

THREE-DIMENSIONAL POLYMERIC CAPILLARY NETWORK:
FABRICATION AND APPLICATIONS

BY

CHUNGUANG XIA

DISSERTATION

Submitted in partial fulfillment of the requirements
for the degree of Doctor of Philosophy in Mechanical Engineering
in the Graduate College of the
University of Illinois at Urbana-Champaign, 2009

Urbana, Illinois

Doctoral Committee:

Assistant Professor Nicholas X. Fang, Chair and Director of Research
Assistant Professor Rohit Bhargava
Associate Professor Gustavo Gioia
Associate Professor Harley T. Johnson

ABSTRACT

Micro capillary networks widely exist in nature in forms of mass transport pathways, such as blood vessels. However their complicated geometry and the extra fine small features bring a great challenge to their potential applications in term of fabrication.

To overcome the fabrication challenge, we presented in this thesis a novel method to fabricate fully three dimensional (3D) microstructures and moving parts using partially crosslinked polymer as sacrificial supports. This was realized on a projection microstereolithography (P μ SL) which produced both the micro structure and the sacrificial part simultaneously using digital grayscale images. To establish the selectivity of the etchant to the partially crosslinked sacrificial parts, we measured the etching rate as a function of photo-crosslinking light intensity and the light exposure time.

As one of the applications of polymeric capillary network, here we showed the implementation of polymeric capillaries coupled with numerical simulation to enhance the mass transport in 3D cell culture. A set of poly (ethylene glycol) micro-fabricated bioreactors were demonstrated with P μ SL technology. We observed both experimentally and numerically the regulation of metabolism in the growth of yeast cells and Chinese hamster ovary cells by controlling the density of micro-capillaries.

In an effort to increase the response speed of a polymeric hydrogel device during solvent actuation, we also reported on the design, analysis, fabrication and testing of several novel polymeric devices. We introduced a capillary network into polymeric devices in such a way as to dramatically increase the rate of long-range solvent transport (compared with diffusion-based mechanisms), while also providing a means to locally

control the swelling of polymeric hydrogel. We realized control of surface-oriented swelling in a curved polymeric beam, which also affected its bending direction.

Compared with traditional silicon MEMS devices, using this method we achieved much higher actuation displacement with respect to the length of the beam without sacrificing the actuation speed. To further increase the transient response speed, we introduced the elastic instability into our beam design. Combined with a design criteria analysis based on beam bending theory, we proved in our experiment the existence of a critical value for a dimensionless parameter that determined the buckle of a curved beam.

ACKNOWLEDGMENTS

My graduate study at the University of Illinois at Urbana-Champaign is one of the most unforgettable experiences in my life. The people I have met and the knowledge and skills I have achieved would undoubtedly benefit my future. It is always my honor to be one of Illinois' alumni.

I would start by thanking my advisor, Dr. Nicholas Fang, for giving me the opportunity to work on exciting and interdisciplinary projects and helping me solve numerous problems throughout my graduate education. I especially feel grateful for his extraordinary patience, kindest support, and continuous encouragement during my exploration of new research fields.

I would also like to thank Dr. Robert Haber for his great generosity, extraordinary patience, and precious financial support in my first few years at the University of Illinois. At the same time, many thanks to all the committee members, Dr. Rohit Bhargava, Dr. Gustavo Gioia, Dr. Harley T. Johnson, and Dr. Jimmy Hsia, for their invaluable suggestions and help.

I gratefully acknowledge Dr. Chen Sun for his pioneer work in projection micro stereolithography which brought me into this field and eventually I built my own system. Special thank to Dr. Leilei Yin for his great discussions on experiment techniques. It is also my pleasure to work with Howon Lee who joined this group later and shared with me his time to develop the second generation of projection micro stereolithography system and to measure the solvent diffusion experiments. To all people in my group, I am truly thankful for their kindest help. Additionally, I would like to thank Dr. Sandra

McMasters and Dr. Zhengyi Shao, for their professional trainings and discussions on cell cultures which enriched the work in Chapter 3.

The unconditional love from my father and sister is always a great source of encouragement. Particularly, I would like to thank my father. His firm support and quiet wisdom are always with me and help me through goods and bads. My mother passed away when I was four, but her smile never fades in my mind, it will lead me towards my dreams forever. Finally and most importantly, I am grateful to my best friend and fiancée, Shu Zhang, for her support, her love, and all the great times she gave to me during all these years.

TABLE OF CONTENTS

CHAPTER 1: INTRODUCTION	1
CHAPTER 2: PROJECTION MICROSTEREOLITHOGRAPHY SYSTEM	4
2.1 INTRODUCTION.....	4
2.2 SYSTEM DESIGN AND CHARACTERIZATION.....	6
2.3 MICROFABRICATED SAMPLES.....	20
2.4 CONCLUSIONS AND OUTLOOK.....	22
REFERENCES.....	23
APPENDIX I.....	25
APPENDIX II.....	26
CHAPTER 3: FULLY THREE-DIMENSIONAL MICRO-FABRICATION WITH GRAYSCALE POLYMERIC SELF-SACRIFICIAL STRUCTURE	29
3.1 INTRODUCTION.....	29
3.2 METHOD AND MATERIALS.....	32
3.3 SELECTIVITY WITH GRAYSCALE EXPOSURE.....	35
3.4 CONCLUSIONS.....	39
REFERENCES.....	40
APPENDIX.....	41
CHAPTER 4: 3D MICROFABRICATED BIOREACTORS WITH CAPILLARIES	43
4.1 INTRODUCTION.....	43
4.2 MICROFABRICATION AND MATERIALS.....	45
4.3 VASCULARIZED MICRO BIOREACTORS.....	46
4.4 METHODS.....	62
4.5 CONCLUSIONS AND OUTLOOK.....	64
REFERENCES.....	68
CHAPTER 5: SOLVENT-DRIVEN POLYMERIC BEAM DEVICES	70
5.1 INTRODUCTION.....	70
5.2 SOLVENT DIFFUSION IN POLYMERS.....	72
5.2 POLYMER ACTUATOR BY SURFACE CAPILLARY.....	82
5.3 BISTABLE POLYMERIC BEAM DEVICE.....	86
5.4 CONCLUSIONS AND OUTLOOK.....	104
REFERENCES.....	106
AUTHOR'S BIOGRAPHY	109

CHAPTER 1

INTRODUCTION

Tubular or capillary networks widely exist in nature and in man-made devices. Naturally, they are common in forms of blood vessels and neural system in animals, veins in plants, and so on. Artificially, they often form micro channels in many medium exchange devices, such as heat exchangers and gas exchangers. Their roles in these forms are basically mass and energy transport and providing a large area for mass and energy exchange between the networks and the space they expand.

The blood capillary is a web of many connected tiny blood vessels, responsible of delivering blood to the tissue under sufficient pressure to exchange materials. This is a two way process, at which nutrients, Oxygen, and other materials, including bacteria, are carried to the tissue and cells during the outflow. On the other hand, blood is returned along with the wastes of cellular metabolism during the return flow. Therefore without blood capillaries, cells or tissues will eventually die of hypoxia and/or the toxicity of their own wastes. Unfortunately, natural blood capillary networks cultured in vitro are rarely observed, forming one of the bottle-necks of constructing thick (>1mm) tissues or organs in vitro, which leads to a long list of patients waiting for organ transplant due to very few organ donors. Although many methods have been proposed to solvent this issue, such as cells on scaffold with growth factors, two dimensional network of micro fabricated micro channels, and molding with polymeric threads, the challenge remains. As a possible alternative, we propose of using artificial three dimensional polymeric capillary network as a bed to create natural capillary system in vitro. This artificial network mechanically

supports the proliferation of the endothelial cells and biologically guides the direction of the growth of the blood capillary.

Capillary networks in plants not only transport water and minerals, but in some motion sensitive plants, such as sensitive mimosa and Venus flytrap, they are in form of ion channels carrying the propagation of so called action potential at a very high speed up to 10 m/s. The action potential triggers the rapid movement of the plants in functions of defense (sensitive mimosa) or nutrition (Venus flytrap). Understanding and mimicking this mechanism will help to design artificial muscles, actuators and explain the nastic motion in plants. However, very few works have been contributed to this field so far. Therefore, we introduce the solvent-swollen polymers as the potential candidate material which analogically substitutes the plant sensitive tissue. To mimic the ion channel, micro capillary networks are imbedded in 3-dimensionally-shaped polymer structures. These capillaries transport the solvent at a high speed driven by the capillary force and trigger the swelling along the pathways which results in a nastic motion as in mimosa. Combined with the elastic instability as shown in Venus flytrap, the engineered polymeric structures are capable of snap motion, providing a much higher transient power output than one without instability mechanism.

However, the polymeric capillary network is one of the most complicated 3 dimensional geometries with multi-scale features. To fabricate ones with high throughput, it requires a micro fabrication technology that has such advantages: 1) capable of rapid fabrication; 2) capable of fully 3 dimensional fabrication; 3) with sub-10 microns resolution, and 4) with potential to scale up. As we thoroughly review all existing micro fabrication approaches, it seems that projection microstereolithography best fits to these

criteria. Nevertheless, projection microstereolithography is still not a fully 3 dimensional micro fabrication technology which limits its application in polymeric capillary networks. To overcome this limit, we for the first time introduce the gray scale self-sacrificial method into projection microstereolithography such that the fully 3 dimensional fabrication is possible.

This dissertation is organized into five chapters. Besides the current chapter which intends to give a brief introduction of the capillary network and the motivations of this dissertation, the other four chapters organized as following:

Chapter 2 describes the realization of a projection microstereolithography system. In this chapter the system configuration, UV optics design, hardware and software integration, and system control will be presented. System characterization will also be described.

Chapter 3 intends to show the implementation and analysis of gray scale self-sacrificial method as an effort to further improve the capability of projection microstereolithography.

Chapter 4 is dedicated to the design and test of a novel micro fabricated bioreactor with capillaries as to improve the mass transport in thick tissue culture.

Chapter 5 will finally show the design and modeling of new polymeric actuators triggered by solvent and powered by polymer swelling. The micro capillary is shaped to transport the solvent and control the swelling of the polymeric devices.

CHAPTER 2

PROJECTION MICROSTEREOLITHOGRAPHY SYSTEM

2.1 INTRODUCTION

Micro capillary system is one of the most complicated geometries in nature. Therefore, to replicate its geometry requires highly sophisticated micro fabrication technology. At the same time, driven by the great economic potential, tremendous efforts have been continuously pouring into the rapid development of micro electro mechanical system (MEMS). Low cost, highly efficient and reliable micro devices enabled by MEMS technologies are remarkably changing the life of the world, such as sensors, actuators, micro display chips, inkjet nozzle arrays and so on. None of these successes could be possible without the strong support from micro fabrication technologies. Most of the micro fabrication technologies are derived from the mainstream IC industry. These silicon-based micro machining technologies contribute significantly to the advancement of MEMS technology. However silicon technologies show limitation in the fabrication of micro devices with three-dimensional (3D) complex geometries. Combining the strong demand and the difficulty to fabricate complex 3D micro devices in the field of silicon based MEMS, scientists and engineers have been developing new approaches to enable the 3D micro fabrication for different materials and applications. For example, the LIGA(German acronym that stands for lithography, electroplating, and molding) process is designed to build high aspect ratio microstructure by incorporating thick resist layers under masked X-ray or laser irradiation [1]. High density plasma etching also creates high aspect ratio micro/nano structures by removing masked material [2]. Both

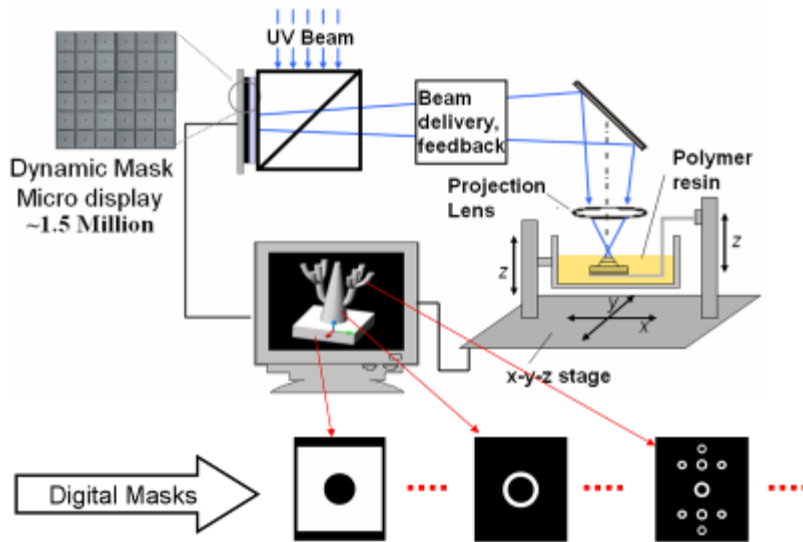
technologies provide limited capability for building micro structure on the vertical direction. However, they are still two and a half dimensional fabrication technologies. The 3D micro fabrication remains a challenge until the introduction of free-forming fabrication technology. Free forming fabrication (FFF) is any fabrication technology that fabricates 3D complex structures by assembling small elements together and it usually starts from and is powered by computer aided design (CAD). FFF includes but not limit to rapid prototyping, 3D printing and direct writing for macro scale ($>1\text{mm}$) fabrication. As for micro scale fabrication, 3D laser chemical vapor deposition (3D-LCVD) technology fabricates the microstructures by laser-induced chemical vapor deposition (LCVD) [3]. Electrochemical fabrication (EFAB) technology has been developed as an extension to the LIGA process in order to fabricate complex 3D metal micro structures [4], in which the electro-chemically deposited metal layers are defined as electrode masks and a planarizing procedure controls the layer thickness. Nevertheless, both 3D-LCVD and EFAB are limited by the specified material selection.

As one of the recent free forming micro fabrication technologies, microstereolithography (μSL) has shined a light on the 3D micro fabrication. Its basic principle is the same as stereolithography, building micro structures in a layer by layer manner by confining the illumination to defined areas in a photo sensitive resin bath. Depending on how each layer is built, microstereolithography can be divided into two types, vector by vector microstereolithography and projection (or integrated) microstereolithography. The vector by vector microstereolithography is first introduced by Takagi and Ikuta [5, 6]. It builds a polymer layer by tracing a focused light beam on a polymer resin surface (with or without constrain). Since then μSL has been greatly

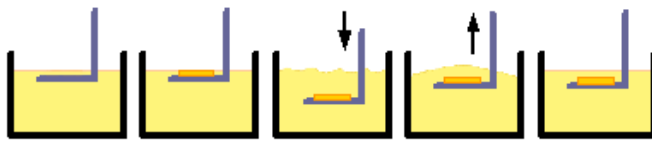
beneficial to a range of fields from micro fluidic systems to tissue engineering. New efforts were also applied to develop a μ SL system which was capable of processing various specifically tailored photopolymers [7]. Furthermore, recent developments in the technology of two photon polymerization (2PP) provide a competing strategy over vector by vector microstereolithography [8-10]. The quadratic dependence of two-photon-absorption assists to confine the solidification in submicron volume. This virtue of the two-photon process allows the fabrication 3D structures by scanning a focus inside the photopolymer which allows the fully 3D micro fabrication. Nevertheless both are slow and expensive serial processes. To overcome the speed limitation and inspired by micro display technologies, scientists incorporated the parallel scheme into μ SL. It is called projection (or integrated) microstereolithography (P μ SL). The core of this technology rests on the use of spatial light modulator (SLM) as a dynamic mask. It can be either a liquid crystal display (LCD, including liquid crystal on silicon (LCOS)) panel or a digital-light-processing (DLP) panel. Both were first introduced by Bertsch [11, 12]. Although, P μ SL can build most of the 3D micro structures, basically bottom to top connected structure, it shows limitation to fabricate some special types of structures, such as overhung and moving parts. We will address this problem in Chapter 2. In this chapter, we will present the details of building and characterizing our P μ SL system.

2.2 SYSTEM DESIGN AND CHARACTERIZATION

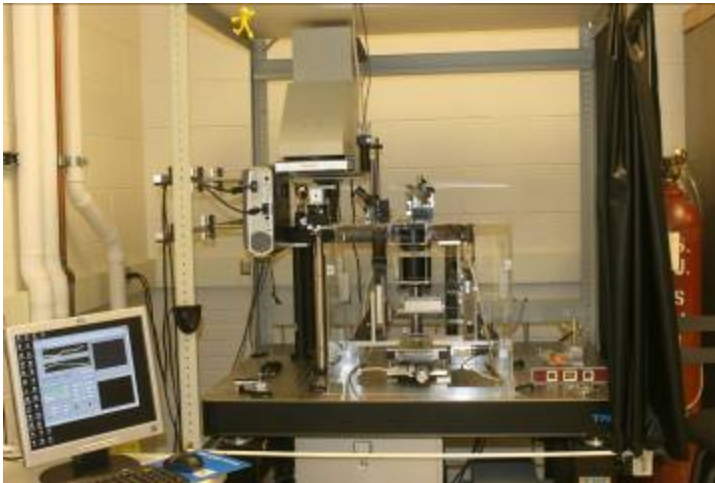
P μ SL inherits the layer-by-layer fashion of microstereolithography, but introduces the dynamic mask for high speed parallel fabrication. The process starts by generating a 3D structure using CAD software and then slices the structure into a sequence of mask images (digital mask). Each image represents a thin layer of the 3D structure. During a



(a)



(b)



(c)

Figure 2.1 (a). Projection microstereolithography system; (b). Sample holder movement during a circle of fabrication; (c). Physical setup of projection microstereolithography system.

fabrication cycle, a single image is displayed on the reflective LCD panel. The image on the LCD is then delivered and projected onto the photo curable liquid surface. The whole

layer (usually 5- 30 microns thick) is polymerized simultaneously. After one layer is solidified, the polymerized component is re-immersed into the resin to allow the formation of a new thin liquid layer on top of it. By repeating the cycle, a 3D microstructure is formed from a stack of layers (Figure 2.1(a), (b)). Our P SL system consists of UV light source, LCD projector, optics, motorized stages, control PC, and control software package. The system sits on a 1000mmX900mm TMC vibration isolated optical table top. To further decrease the vibration effect, most of the vibration components, especially those equipments with cooling fans (PC, UV light intensity controller, UV light power supplier, projector, and stage controller) are placed off the table top. The real configuration of the system is shown in Figure 2.1 (c).

2.2.1 Dynamic mask generator

There are two kinds of dynamic mask generator from the mainstream of micro display technology, LCOS and DLP. LCOS, which is also known as reflective LCD, is considered to be more effective than traditional standard LCD in terms of image brightness and contrast. Each pixel of LCOS can modulate the polarity of reflected incident light beam under application of electro voltage. Thus, with a polarizer in the path of the reflected light beam, the amount of transmitted light is controlled by the voltage of the electros of each LCOS pixel. DLP is a novel display technology first developed by Texas Instruments in 1987. Instead of modulating the polarity of reflected light as in the case of LCOS, each pixel in DLP chip is actually an individual micro mirror which tilting the direction of the reflected light by changing the angle of each micro mirror. The angle can be tilted up to $\pm 10^\circ$. A bright pixel directs the light through the lens; while a dark pixel guides light away from the lens. The gray scale of images is controlled by switching

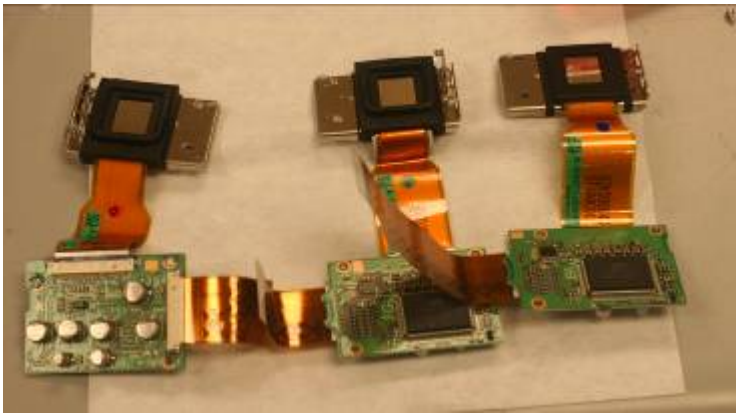


Figure 2.2 Close view of Canon Realis SX50 projector and the three integrated LCOS panels.

the angle of mirror between bright and dark states at different frequencies. Although DLP chip has shaper image and shorter response time compared with LCOS [13], it requires more efforts to integrate the DLP chip into a home-made P μ SL system due the small switching angle range of each pixel mirror. Moreover, the higher response time of the DLP is not very critical due to the fact that the fabrication of each layer in P μ SL takes more than ten seconds. Therefore we choose LCOS chip as our dynamic mask. The LCOS chip is taken from the commercially available high resolution LCOS projector, Canon Realis SX50 with native resolution 1400X1050, contrast ratio 1000:1, and

brightness 2500 ANSI lumens. Each pixel of the LCOS panel is $10\ \mu\text{m} \times 10\ \mu\text{m}$ in size. There are three LCOS panels in the projector. Each panel is optimized to modulate the light of red, green, and blue color (Figure 2.2). Since the wavelength of the light source we use is 436nm, the panel for blue color is the best choice for our system. We removed the light engine in the projector and kept all the electronic components. The LCOS panel for blue light was replaced outside of the projector cover in order to have it aligned with the optics of P μ SL and exposed to external light source (Figure 2.3).

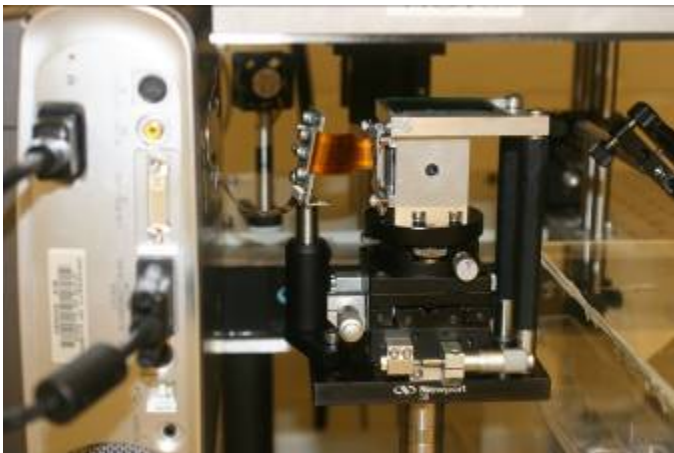
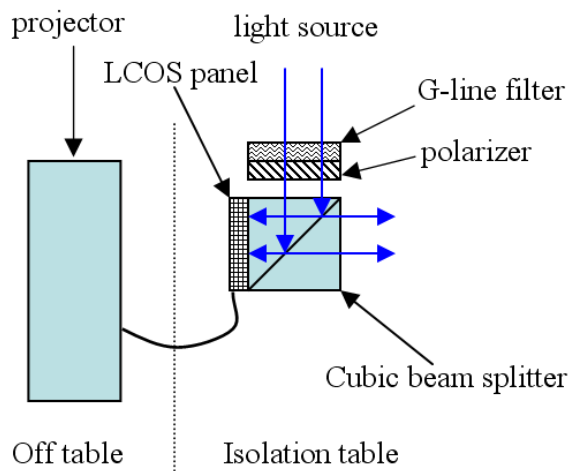


Figure 2.3 Schematic drawing and real assembly of LCOS panel in our P μ SL system.



Figure 2.4 Stage assembly of our P μ SL system

2.2.2 Translation stages

Four Newport motorized translation stages position the substrate holder and the resin container (Figure 2.4). Two stages for X-Y in plane position, the other two, which sit on the X-Y stage assembly, move the resin container and the substrate holder on the Z direction. These stages have a maximum speed of 10mm/s, minimum step size 1 μ m and a range of motion of 10cm and 15cm. They are driven by a Newport MM 3000 motion controller which is in turn operated by the Labview control program. It is important that the X-Y stages move in a plane parallel to the focus plane or the image plane of projection lens. Otherwise, the resin free surface will lose focus during the translation on X-Y stages which results in a poor fabrication resolution. Therefore, the stage assembly is seated on a 3-point adjustable rectangular aluminum plate which is placed directly on the optical table top. By adjusting the screws fixed in the 3 corners of the aluminum plate, the plate can be leveled to be parallel to the focus plane of projection lens. Also the backlash of stages can be a great concern, because it is the primary reason of misalignment in X-Y plane and it also reduces the accuracy on the Z direction. Therefore,

a scheme of backlash compensation or position feedback is critical for the accurate stage control.

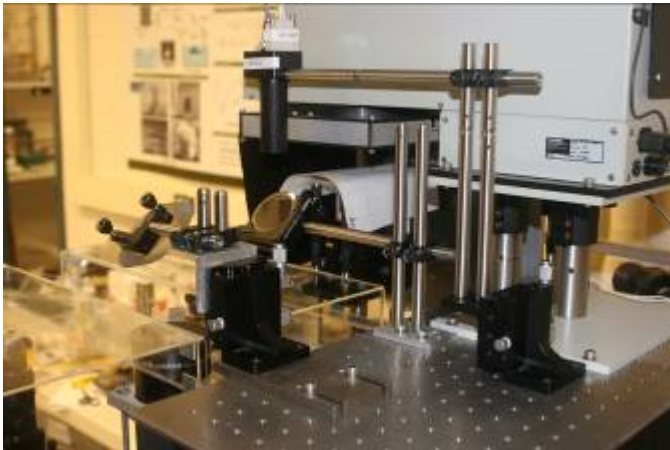
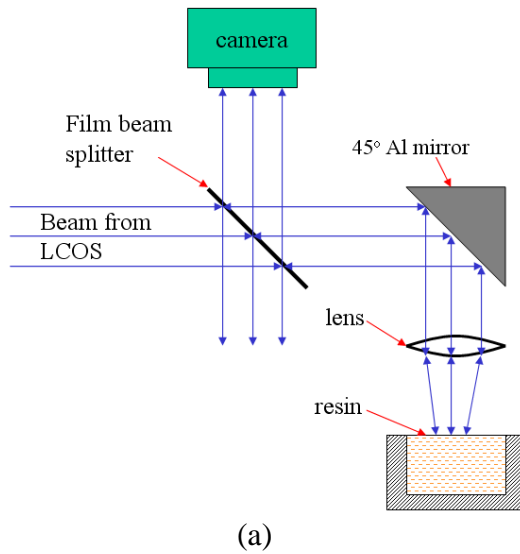


Figure 2.5 (a). The schematic assembly of optics in our P μ SL system. (b). The real assembly of optics.

2.2.3 Optics

The optics in our P μ SL system includes film beam splitter (Pellicle, Thorlabs), 45° Al mirror, CMOS camera, and reduction lens (Figure 2.5). The modulated light beam from LCOS panel is split into 92% transmission and 8% reflectance by the film beam splitter. The 8% reflected light is absorbed by a black fabric sheet below the splitter, while the

92% transmission light is guided through the reduction lens by the 45° Al mirror. The reduction Zeiss lens reduces the size of the incoming image by a factor of ten and projects the image onto the liquid surface. The size of pixel on LCOS panel is 10 μ m, therefore its image after the lens is about 1 μ m which is the highest resolution we can achieve. The lens also allows light reflected from the resin surface to return to the CMOS camera positioned above the beam splitter. The CMOS camera is used to monitor the images on the resin surface, so that it helps to tell whether the resin surface is in the focus plane or not and take corresponding steps to position the resin surface in focus. The position of the sample holder is also corrected based on the vision of the CMOS camera.

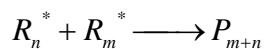
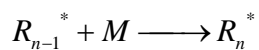
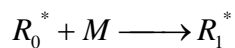
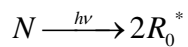
2.2.4 UV light source

The light source of our P μ SL system is an Oriel 87435-1000-1 mercury lamp that projects high-intensity (200-500W) light at a wavelength of 436 nm (with filter). It is powered by an Oriel 68810 arc lamp power supply and tuned by an Oriel 68850 Light Intensity Controller. Study [14, 15] shows that spatially coherent wavefronts scattering at an optical surface, which causes different parts of the wavefronts to interfere at the image plane. This produces a random distribution of fringe patterns called speckles that can greatly degrade the projected image quality like sharpness and contrast. In general, the speckle effect can be eliminated by removing the diffractive source along the light path and protecting the path with a clean environment. However digital micro display chips are composed of millions of single unit, they act as strong diffraction devices under the illumination of coherent light sources. As a result, the light source used in this system is a broad band mercury lamp for lithography in silicon industry. This is a non coherent UV source. A uniform illumination is essential for a good fabrication resolution control.

Therefore a fly-eye device is integrated in the mercury lamp. It is composed of many evenly distributed small convex lenses and each small lens serves as a light source. The lights from all the small lenses overlap and create the uniform light intensity in the working plane. The variation is within 5%. A G-line (436nm) filter is placed between the light source and the LCOS chip for monochromic illumination. The performance of most optical components varies with the wavelength. Therefore monochromic illumination helps to increase the projected image quality. On the other hand, UV can damage the liquid crystal materials in a long term. The filter protects the LCOS panel by blocking out most of the UV.

2.2.5 Photo polymerization

The UV curable resin is a combination of monomer, photo-initiator, and UV absorber. Under UV light illumination, photo-initiators (N) absorb the incident photons (hv) and generate radicals(R^*). The excited radicals react with the monomer molecules (M) and form larger reactive molecules. The reactive molecules continue to react with other monomers to form longer reactive molecules. The reactive molecules keep growing until two of them meet together and form a stable polymer chain. The solidified polymer structure eventually forms by the cross-linking of those polymer chains.



The vertical thickness of the polymerized layer or curing depth is determined by the light energy density (dose) at the exposure area. According to the exponential law of light absorption within the resin, the light intensity $I(z)$ equals:

$$I(z) = I_0 \exp\left(-\frac{z}{D_p}\right) \quad (2.1)$$

where I_0 is the intensity at liquid surface, and D_p is the light penetration depth in the resin. When the light intensity decreases to the value below the critical dose, polymerization stops. The curing depth C_d equals: [13]

$$C_d = D_p \ln\left(\frac{E_0}{E_c}\right) \quad (2.2)$$

$E_0=I_0t$ is the dose at the surface. E_c is the critical dose of polymerization. For different combinations of resin, it is always helpful to measure the curing depth curve versus exposure time. This curve can help to increase the fabrication accuracy on the direction of layer stacking by precisely controlling the exposure time (or dose), especially in the case of overhung structures. Furthermore, this curve can help to optimize the fabrication speed by providing the exact amount of UV doses for corresponding layer thickness. The resin to be measured is poly (ethylene glycol) diacrylate(PEGDA) (MW=575, Sigma-Aldrich) with 2 wt % initiator (Ciba, Irgacure 918) and 0.75 wt % photo absorber (Sudan I, Sigma-Aldrich). The UV light intensity is 4.75 mW/cm². The sample we fabricated to measure the curing depth is shown in Figure 2.6 (a). It is a ladder-shaped structure with each step fabricated under different exposure time. As we can see in Figure 2.6 (b), the curing depth mainly follows equation (2.2). As a rule of thumb, the exposure time for each layer should be the value associated with the curing depth 4-5 μm larger than the

actually layer thickness. In this way, we can reduce the surface roughness and allow a strong bonding between layers.

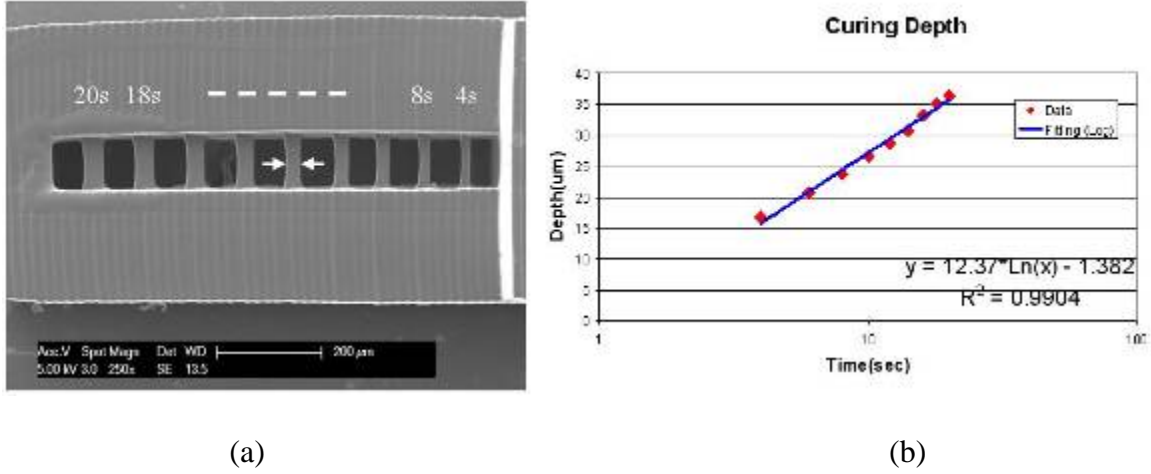


Figure 2.6 (a). Sample for curing depth measurement. (b). Curing depth curve with respect to UV exposure time.

2.2.6 Process control

Before starting fabrication, one should have the bitmap mask images ready. In our system, this is accomplished by slicing the 3D model in AutoCAD model space using user defined Visual Basic function. The source code of this function can be found in Appendix I. This function works for AutoCAD 2002 or older versions only. Current commercial available LCOD panel or DLP panel is of 1~3 centimeters. As a result, the final fabrication area is only couple millimeters in size with a ten-time reduction lens. Therefore it will be difficult to fabricate samples larger than the maximum image of a single exposure. To overcome this problem, there are two ways. One way is to use multiple-chip technology: many panels are assembled into a much larger screen. However this will at the same time require much larger optical components, thus dramatically increasing the cost of fabrication system. To eliminate the gaps between

panels also a big challenge. The other way is to divide a large layer into several sub-regions, the size of each region is equal to or smaller than the size of a single panel image. In this way, each large layer is fabricated by polymerizing all the smaller sub-regions. The adjacent sub-regions are slightly overlapped ($4\mu\text{m}$ - $10\mu\text{m}$) to fuse them together. This method combines the advantages of serial and parallel process. Serial process is for larger scale and parallel process for smaller scale. In our system we use sub-region method. The sub-region mask images are created by running the whole-layer masks through the sub-region creator which is a matlab function (Appendix II).

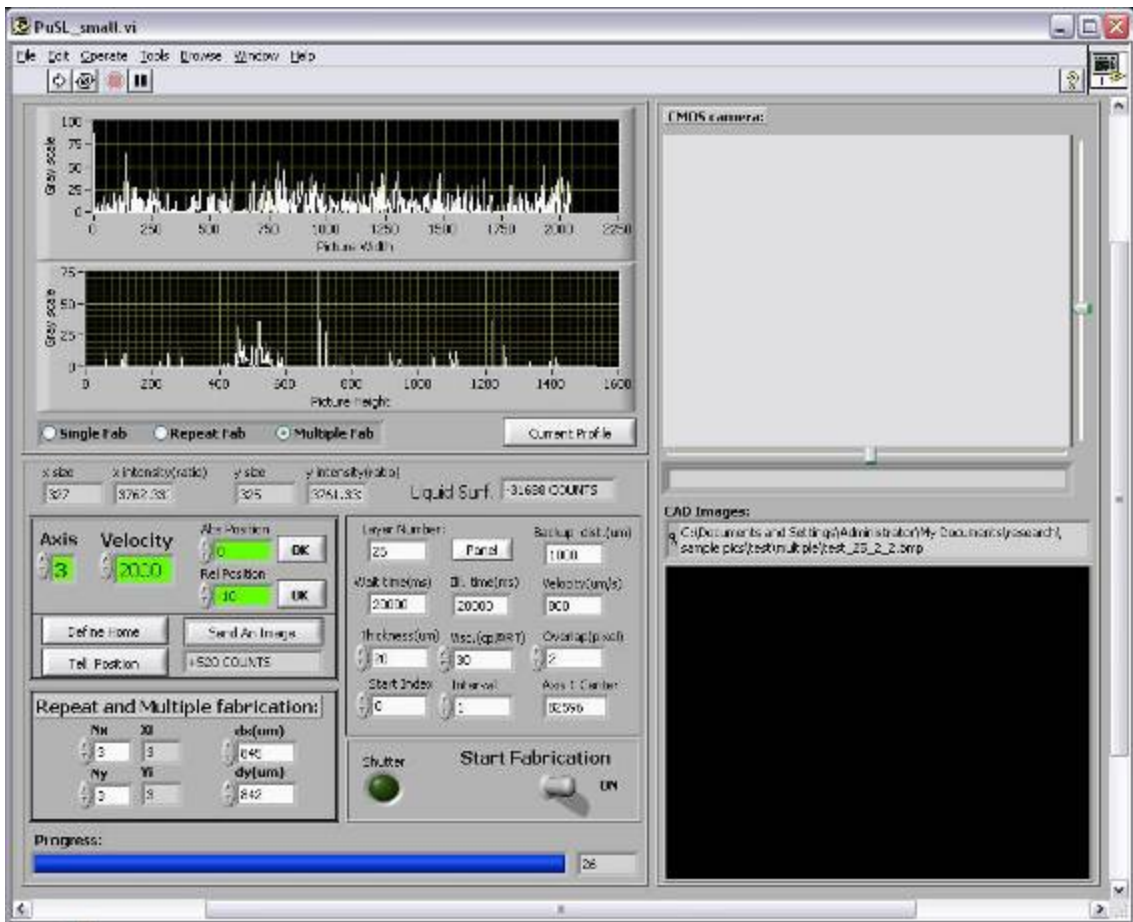


Figure 2.7 Control panel for projection micro stereolithography

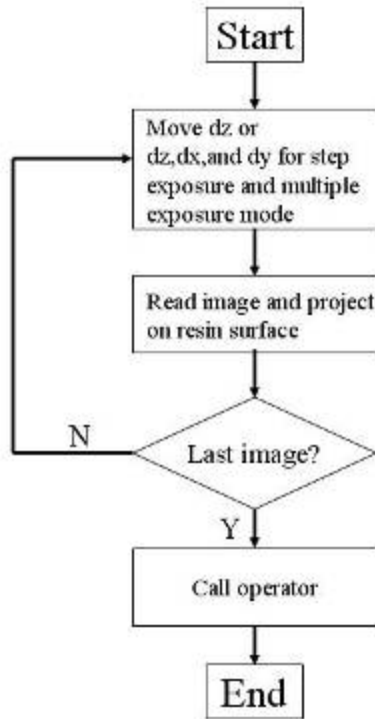


Figure 2.8 Brief process flow chart of projection micro stereolithography process

The process control is integrated in a software package which is developed in Labview language (Figure 2.7). This software communicates with all hardwares through series of interfaces including image grabber for COMS camera, GPIB for stage control, RS232 for shutter control, modem for phone communication, and graphic card for LCOS projector. There are three fabrication modes: single-exposure, step-exposure, and multiple-exposure mode. Single-exposure mode builds small sample with one exposure for each layer, step exposure mode builds an array of small samples, and multiple-exposure mode is designed for large samples which requires multiple exposure for one layer. In order to save fabrication time, in the case of multiple-exposure mode, each sub-region mask is checked to determine whether there is feature in the image. If the image does not contain any feature (or no white pixels) then the exposure procedure will be

cancelled for current sub-region for current layer. This scheme shows time-saving advantage in the fabrication of sparse structures which contain many blank sub-region masks.

The photo-polymerization takes place at the focus plane of reduction lens. Therefore the resin free surface should be placed at the focus plane all the time. Furthermore, the substrate, on which the sample sits, is also positioned relative to the focus plane to define a new layer of thin resin for next exposure. Thus finding the focus plane for both the resin surface and the substrate is critical for the fabrication process. This can be achieved by incorporating an auto-focus mechanism at the beginning of fabrication with the feedback of image information from the CMOS camera. The details of the implementation of auto-focus are present in the following steps:

1. Move stage to one side of focus plane and move towards the other side step by step;
2. A 100X100 pixel calibration image is projected on the surface of resin;
3. CMOS camera takes an image every move step;
4. The image from camera is denoised using median filter ;
5. Calculate the contrast of the image ;
6. If contrast is larger than 1.5 then calculate the feature size, else go back to step 1;
7. move a smaller step, calculate the contrast and feature size;
8. If the contrast increases and the feature size decreases then go to step 7, else change the translation direction of the stage and go to step 7;
9. If the step size is smaller than $3\mu\text{m}$ and the feature size is smaller than 300 pixels then save the feature size and stop.

The position of the resin surface may change during the fabrication due to the ambient temperature change or the evaporation of the polymer solution. It is necessary to check the focus every hour by projecting the same calibration image. If the feature size is appreciably different from the stored feature size, then compensate the error by running the auto-focus scheme again. The brief process flow chart is shown in Figure 2.8.

2.3 MICROFABRICATED SAMPLES

In this section, we will present some of the representative samples that are enabled by our projection micro stereolithography system. The basic capabilities of our system are shown in Table 2.1.

Resolution	Speed	Max. Sample Size
2 μm (in plane)	4mm ³ /hour (viscosity of resin	30mm \times 30mm
1 μm (off plane)	at 10cP)	\times 15mm

Table 2.1 The basic capabilities of our projection micro stereolithography.

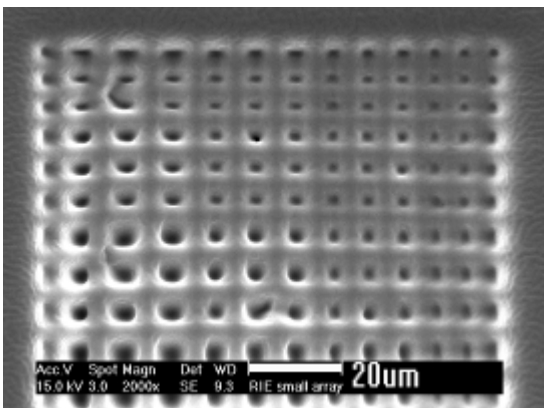


Figure 2.9 Grid pattern for resolution test. The holes at the top-right corner have size of 2 μm .

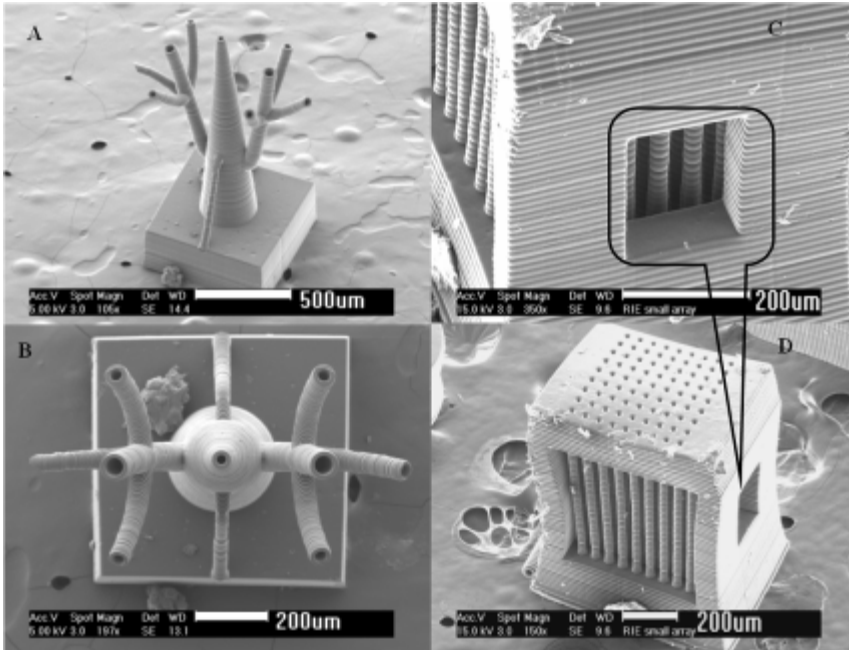


Figure 2.10 A, B: highly branched capillary network structure. The inner radius of capillaries varies from $10\mu\text{m}$ to $30\mu\text{m}$. C, D: a 9 by 9 capillary array with $10\mu\text{m}$ inner radius, $20\mu\text{m}$ outer radius, $80\mu\text{m}$ spacing and $800\mu\text{m}$ in length (aspect ratio >20 , effective channel density $>150/\text{mm}^2$).

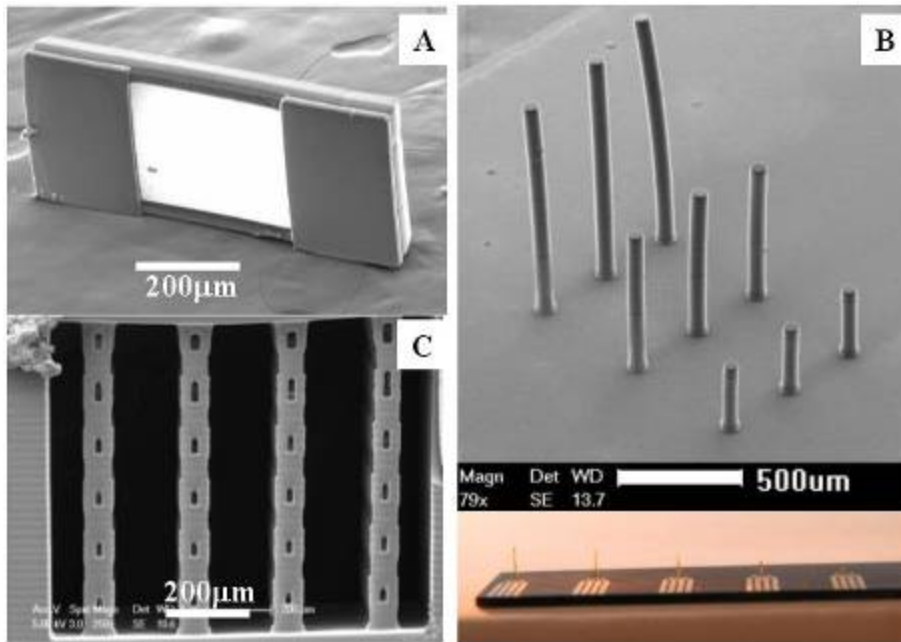


Figure 2.11 A. $2\mu\text{m}$ -thick polymer film for pressure sensor applications, material: 1,6-hexanediol diacrylate(HDDA) (SR238, Sartomer). B. On-chip hair cells for flow detection, material HDDA. Collaborate with Dr. Chang Liu. C. Micro capillaries (material PEGDA) with $10\mu\text{m}\times 20\mu\text{m}$ side windows for mass transport applications.

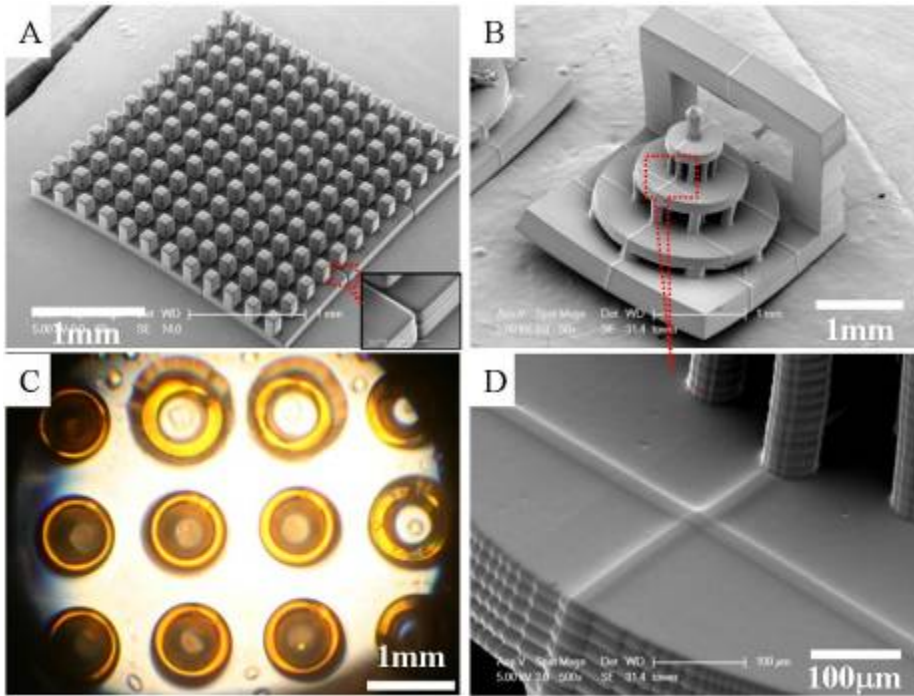


Figure 2.12 A. A large array of blocks fabricated using multiple-exposure mode without edge overlapping. In the zoom-in sub-figure, we can see a notch along the common edge of adjacent exposures. These notches can be mechanically weak points due to the stress concentration. B, D. 3D micro tower fabricated using multiple-exposure mode with 15 μm edge overlapping. The notches are eliminated by overlapping. C. An array of rings fabricated using step-exposure mode. Those rings are with 900- μm outer diameter and 200- μm height, the center-to-center spacing is 1500 μm . All the samples are made of PEGDA.

2.4 CONCLUSIONS AND OUTLOOK

In this chapter, we successfully developed a P μ SL and schematically demonstrated the basic physical and chemical principles of each sub-system. Microfabricated samples for different applications were presented. These samples visually proved the unique capabilities of our projection micro stereolithography system. Although P μ SL shows advantages over many other microfabrication technologies, challenges remain in terms of fabrication speed, sample geometries, and fabrication with heterogeneous materials.

P μ SL system based on free resin surface spends more than half of the fabrication time on waiting free surface to settle. As a solution, a quartz cover coated with non-stick material was introduced to eliminate the free surface. However, on one hand, this cover shows limitation in the selection of non-stick material for various resin solutions; on the other hand, large hydraulic pressure gradient shows up when partially finished sample moved away from the cover. This large pressure gradient may damage samples or even stripe samples off the substrate.

As we mentioned previously, although P μ SL is able to fabricate most of 3D micro structures, it shows limitation in building moving parts and overhung structures. The reason is that part of moving structures or overhung structures is disconnected from remain portion at certain stage during P μ SL fabrication process. Therefore this disconnected part may drift away from correct position during sample transport in the resin. We propose a solution for this problem in the next chapter.

New technologies have been developed to quick fabricate heterogeneous micro particles, such as flow lithography and its derivatives [14-20]. In these technologies, the oxygen inhibition layer close to the PDMS surface provides an isolation of polymerization from the surface, such that finished samples can be flushed away by the resin stream and gives a very high throughput. However sample produce by these methods are mainly 2D ones. This limitation reserves the room for P μ SL to be further improved.

REFERENCES

- [1] E.W. Becker, W. Ehrfeld, P. Hagmann, A. Maner, D. Munchmeyer, *Microelectron. Eng.* 4 (1986) 35.

- [2] S A McAuley, H Ashraf, L Atabo, A Chambers, S Hall, J Hopkins and G Nicholls, Silicon micromachining using a high-density plasma source, *J. Phys. D: Appl. Phys.* 34(2001)2769-2774.
- [3] K. Williams, J. Maxwell, K. Larsson, M. Bioman, Technical digest in: Proceedings of the IEEE International MEMS 99 Conference, 1999, p.232.
- [4] A Cohen, G Zhang, F Tseng, U Frodis, F Mansfeld, P Will, Proceedings of the IEEE international MEMS 99 conference, 1999,p 244
- [5] T. Takagi and N. nakajima, the 4th International Symposium on Micro Machine and Human Science (MHS'93), 1993
- [6] Ikuta and K.Hirowatari, the 6th IEEE Workshop on Micro Electro Mechanical Systems (MESMS'93) 1993.
- [7] J. Stampfl, S. Baudis, C. Heller, R. Liska, A. Neumeister, R. Kling, A. Ostendorf, and M. Spitzbart 2008 Photopolymers with tunable mechanical properties processed by laser-based high-resolution stereolithography *J. Micromech. Microeng.* 18 125014.
- [8] J. Serbin, A. Egbert, A. Ostendorf, B. Chichkov, R. Houbertz, G. Domann, J. Schulz, C. Cronauer, L. Frohlich, and M. Popall 2003 Femtosecond laser-induced two-photon polymerization of inorganic-organic hybrid materials for applications in photonics *Optics Letters* 28 301-3.
- [9] S. Kawata, H. Sun, T. Tanaka, and K. Takada 2001 Finer features for functional microdevices *Nature* **412** 697-698.
- [10] S. Maruo, O. Nakamura, and S. Kawata 1997 Three-dimensional microfabrication with two-photon-absorbed photopolymerization *Optics Letters* **22** 132-4
- [11] A. Bertsch, S. Zissi, J.Y. jezequel, S. Corbel and J. C. Andre, Microstereolithography using a liquid crystal display as dynamic mask-generator, *Microsystem Technologies*, p42-47, 1997
- [12] Beluze, L., Bertsch, A. and Renaud, P., Microstereolithography: a new process to build complex 3D objects , Symposium on Design, Test and microfabrication of MEMs/MOEMs, Proceedings of SPIE, v3680, n2, p808-817,1999
- [13] C. Sun, N. Fang, D.M. Wu, X. Zhang, *Sensors and Actuators A*, 2005, 121,113.
- [14] Neil A. Beaudry, and Tom D. Milster, "Effects of object roughness on partially coherent image formation." *Optics letters*, Vol. 25, No. 7, (2000): 454-6.
- [15] Doany, F. E., Singh, R. N., Rosenbluth, A. E., Chiu, G. L.-T., "Projection display throughput: Efficiency of optical transmission and light source collection." *IBM J. Res. Develop.* Vol. 42, No. 3/4, (1998): 387-398.
- [16] D. Dendukuri, D. C. Pregibon, J. Collins, T. A. Hatton, P. S. Doyle, "Continuous-flow lithography for high-throughput microparticle synthesis", *Nat.Mater.* 2006, 5, 365.
- [17] D. Dendukuri, S. S. Gu, D. C. Pregibon, T. A. Hatton, P. S. Doyle," Lock release lithography for 3D and composite microparticles", *Lab on a Chip*, 2007, 7, 818.
- [18] D. C. Pregibon, M. Toner and P. S. Doyle," Multifunctional Encoded Particles for High-Throughput Biomolecule Analysis",*Science*, 2007, 315, 1393–1396.
- [19] Seung Ah Lee, Su Eun Chung, Wook Park, Sung Hoon Lee and Sunghoon Kwon, "Three-dimensional fabrication of heterogeneous microstructures using soft membrane deformation and optofluidic maskless lithography", *Lab on a chip*, 2009, 9, 1670–1675

[20] Dhananjay Dendukuri, and Patrick S. Doyle, “The Synthesis and Assembly of Polymeric Microparticles Using Microfluidics”, Adv. Mater. 2009, 21, 1–16

APPENDIX I

Sub SectionSolid()

'The CAD model must be drawn from z=0 plane towards z>0 direction.

'setup page for plot

'before run this code make sure the model is Gouraud Shaded, view from the top toward -z direction

'Change the model height and layer thickness as necessary

'Change the file path and file name as nessary

'run the code, pick the solid object in AutoCAD window to start slicing.

'updated by chunguang on 09/12/2007

Dim Layerthickness As Double

Dim Layernumber As Long

Dim SectionI As Long

Dim ModelHeight As Double

Dim Filename As String

Dim Filetype As String

'!!

startindex = 0 'start index for filename

ModelHeight = 300 'The model height

Layerthickness = 30 'the thickness of each layer

Filename = "drive:\folder\filename"

'Change the destination file path as necessary,

'the last word in quotation marks is the file name.

'!!

Layernumber = Fix(ModelHeight / Layerthickness)

Dim modelobj As Acad3DSolid

Dim basepoint As Variant

'user select the 3d entity

ThisDrawing.Utility.GetEntity modelobj, basepoint

' Section 3d model

Dim sectionObj As AcadEntity

Dim sectionPt1(0 To 2) As Double

Dim sectionPt2(0 To 2) As Double

Dim sectionPt3(0 To 2) As Double

Dim sset As AcadSelectionSet

For SectionI = 0 To Layernumber - 1

```

sectionPt1(0) = 1: sectionPt1(1) = 1: sectionPt1(2) = Layerthickness * SectionI
sectionPt2(0) = 1: sectionPt2(1) = -1: sectionPt2(2) = Layerthickness * SectionI
sectionPt3(0) = -1: sectionPt3(1) = 1: sectionPt3(2) = Layerthickness * SectionI
Set sectionObj = modelobj.SectionSolid(sectionPt1, sectionPt2, sectionPt3)
sectionObj.Color = acRed
'hatch the sections
ThisDrawing.SendCommand "hatch" & vbCr
ThisDrawing.SendCommand "s" & vbCr
ThisDrawing.SendCommand "last" & vbCr
ThisDrawing.SendCommand vbCr
'Export the sections as bmp files
Set sset = ThisDrawing.SelectionSets.Add("layer")
sset.Select acSelectionSetLast
sectionObj.Delete 'delete section
modelobj.Visible = False 'hide 3d solid for plotting hatch
ThisDrawing.Plot.PlotToFile Filename & Str(SectionI + startindex) 'plot hatch into file
with current pagesetup
sset.Erase 'delete the layers in ACAD space
sset.Delete
modelobj.Visible = True 'show 3d solid for hatch

Next SectionI
MsgBox "Operation is done! There are " + Str(Layernumber) + " layers!", vbOKOnly +
vbExclamation, "Message"
End Sub

```

APPENDIX II

```

%Image split code; output filename -> name#_#_#.bmp -> number of
%digits may change, # starts from 0, with adjacent images partly overlap,
%updated by Chunguang on 08/29/2007
clear all;
[imagename,pathname,filterindex]=uigetfile('*.*.bmp','Select a first layer image');
prompt={'Number of layers','division in X-dir.','Division in Y-dir','Overlap Pixels'};
dlgtitle='Input filename and Specify matrix size';
answer=inputdlg(prompt,dlgtitle);
[layer nnx nny overlapstring]=deal(answer{:});
k=str2double(layer);
ext='.bmp';
ny=str2double(nny);
nx=str2double(nnx);
overlap=str2double(overlapstring);
ss=size(imagename);
nleng=ss(2)-6;
commonname=sscanf(imagename,'%c',[nleng]);
mkdir(pathname,'multiple');

```

```

spc='_';

for m=1:k
    m          % show m
    seq=num2str(m-1); % from 0
    filename=[commonname,' ',seq,ext];
    I=imread([pathname,filename]);
    imagesize=size(I);
    dy=ceil(imagesize(1)/ny);
    dx=ceil(imagesize(2)/nx);

%top left corner
I2=imcrop(I,[1,1,dx+overlap-1,dy+overlap-1]);
outname=[pathname,'multiple\',commonname,num2str(m-1),spc,'0',spc,'0',ext];
imwrite(I2,outname,'bmp');
%top right corner
I2=imcrop(I,[(nx-1)*dx-overlap+1,1,dx+overlap-1,dy+overlap-1]);
outname=[pathname,'multiple\',commonname,num2str(m-1),spc,num2str(nx-
1),spc,'0',ext];
imwrite(I2,outname,'bmp');
%bottom left corner
I2=imcrop(I,[1,(ny-1)*dy-overlap+1,dx+overlap-1,dy+overlap-1]);
outname=[pathname,'multiple\',commonname,num2str(m-1),spc,'0',spc,num2str(ny-
1),ext];
imwrite(I2,outname,'bmp');
%bottom right corner
I2=imcrop(I,[(nx-1)*dx-overlap+1,(ny-1)*dy-overlap+1,dx+overlap-1,dy+overlap-1]);
outname=[pathname,'multiple\',commonname,num2str(m-1),spc,num2str(nx-
1),spc,num2str(ny-1),ext];
imwrite(I2,outname,'bmp');
%top no corners
for ix=2:nx-1
    I2=imcrop(I,[(ix-1)*dx-overlap+1,1,dx+2*overlap-1,dy+overlap-1]);
    outname=[pathname,'multiple\',commonname,num2str(m-1),spc,num2str(ix-
1),spc,'0',ext];
    imwrite(I2,outname,'bmp');
end
%bottom no corners
for ix=2:nx-1
    I2=imcrop(I,[(ix-1)*dx-overlap+1,(ny-1)*dy-overlap+1,dx+2*overlap-1,dy+overlap-
1]);
    outname=[pathname,'multiple\',commonname,num2str(m-1),spc,num2str(ix-
1),spc,num2str(ny-1),ext];
    imwrite(I2,outname,'bmp');
end
%left no corners

```

```

for iy=2:ny-1
    I2=imcrop(I,[1,(iy-1)*dy-overlap+1,dx+overlap-1,dy+2*overlap-1]);
    outname=[pathname,'multiple\',commonname,num2str(m-1),spc,'0',spc,num2str(iy-
1),ext];
    imwrite(I2,outname,'bmp');
end
%right no corners
for iy=2:ny-1
    I2=imcrop(I,[(nx-1)*dx-overlap+1,(iy-1)*dy-overlap+1,dx+overlap-1,dy+2*overlap-
1]);
    outname=[pathname,'multiple\',commonname,num2str(m-1),spc,num2str(nx-
1),spc,num2str(iy-1),ext];
    imwrite(I2,outname,'bmp');
end
%nonedge blocks
for iy=2:ny-1
    for ix=2:nx-1
        I2=imcrop(I,[(ix-1)*dx-overlap+1,(iy-1)*dy-overlap+1,dx+2*overlap-
1,dy+2*overlap-1]);
        outname=[pathname,'multiple\',commonname,num2str(m-1),spc,num2str(ix-
1),spc,num2str(iy-1),ext];
        imwrite(I2,outname,'bmp');
    end
end
clear I;
end % end of layer loop m
%create a text file with name of overlap pixels
save ([pathname,'multiple\overlap_',overlapstring,'.txt'],'overlap','-ascii');
uiwait(msgbox('Selected set of images have been successfully splitted!','Completed'));
clear all;

```

CHAPTER 3 FULLY THREE-DIMENSIONAL MICRO-FABRICATION WITH GRAYSCALE POLYMERIC SELF-SACRIFICIAL STRUCTURE

3.1 INTRODUCTION

P μ SL is able to build most of the 3D micro structures, basically bottom to top connected structures. However due to the nature of layer by layer fabrication scheme in polymer liquid, the P μ SL method requires that current layer must be precisely laid on the top of last one. When the partially-finished part is transported in the monomer solution, the last layer must stay where it is designed to be. In most of the cases, this condition is

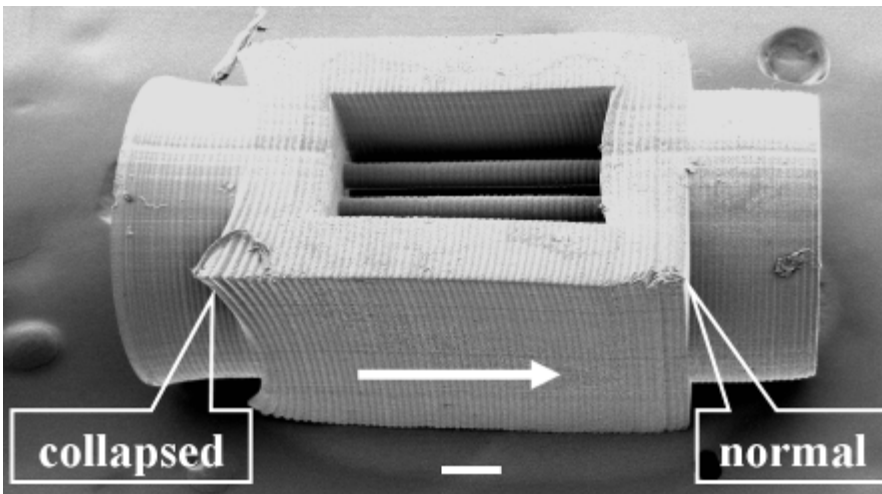


Figure 3.1 Overhung structures collapse without sacrificial structures during P μ SL process. The arrow indicates the fabrication direction and the scale bar is 100 microns.

fulfilled. However for “ceiling lamp” like structures or moving parts, the transport of the partially-built structures in the polymer solution may introduce undesirable drift as the critical parts are not connected to the rest of the solidified components or not well supported. This can cause the structure to collapse as shown in Figure 3.1. In macro scale,

additional supporting structures, usually supporting rods, are introduced to solve this problem. Later in post-processing, those supporting structures are manually removed. It is impractical to replicate the same procedure in micro scale. Furthermore, some supporting structures may be embedded and beyond the reach from outside.

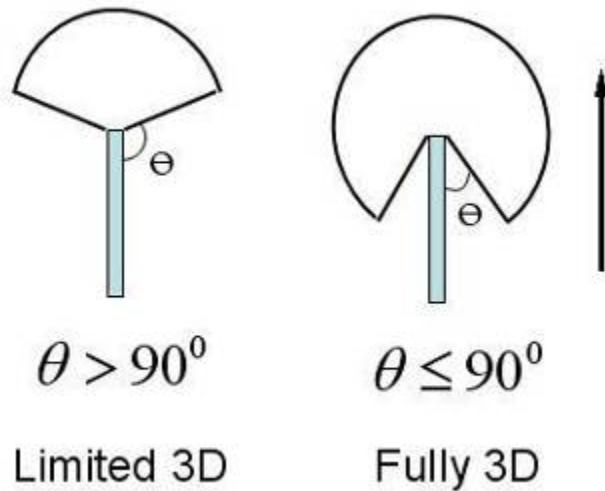


Figure 3.2 Difference between limited 3D and fully 3D micro fabrication, arrow indicates the direction of fabrication.

For the fully 3D micro fabrication in P μ SL, the sacrificial supporting structures become necessary. We define the fully 3D micro fabrication as in Figure 3.2. For a limited 3D micro fabrication technology, micro structures connected to supporting structures can not extend on the opposite direction of fabrication, which is uniquely possible in fully 3D micro fabrication. The sacrificial structures either fix the last layer to the partially finished part or prevent it from undesirable bending. The sacrificial layer has long been adopted by the surface micro machining technologies [1]. There are different sacrificial materials for difference applications. Each material involves a specific release mechanism: HF etching for silica, titanium and aluminum, alkaline solution etching for porous silicon, reactive ion etching for organic polymers and water-soluble sacrificial

layer [1-5]. The sacrificial layer in P μ SL was first introduced by Cabrera [6]. However, in previous works the common approach is to deposit a layer of different material which is dissolved or etched later. The sample has to be switched from one solution to another and go through different coating processes. The cleaning, alignment and focusing process in each switch will dramatically reduce the fabrication speed. This impairs the advantages of P μ SL as a monolithic approach. Therefore we introduce the new self-sacrificial supporting structure which shares the same polymeric material with the micro structure. Poly (methyl methacrylate) (PMMA) is reported to be a self-sacrificial material using deep-UV exposure [7]. In this work PMMA is used as both the structural and sacrificial layers. In order to create the sacrificial layers, deep-UV exposure is applied to change the average molecular weight of PMMA which is dissolved later. However, this method uses different process for structural layers (spin coating) and sacrificial layers (deep-UV exposure). It also relies on gold layer as embed mask for patterning which requires sputter coating process. As mentioned above, the involving of multiple processes dramatically reduces the fabrication speed and increases the cost. Therefore the fully 3D micro fabrication remains a challenge for this method.

As a new approach, our sacrificial structure is fabricated simultaneously with the micro structure under the light exposure of lower intensity which is created by the digital mask of lower grayscale. Thus it has a lower degree of polymerization and a higher etching rate in etchant. For each layer there is a corresponding digital mask. If the layer does not intersect with the sacrificial structure, then the corresponding digital mask remains black and white. Only the areas of white are polymerized. When the layer intersects the sacrificial structure, then the associated digital mask has three grayscale

levels: black, white and gray. Photo-crosslinking will take place simultaneously under the white and gray areas, but with different degree of polymerization. This allows the etching selectivity between white and gray areas. The key principle for this technique is that the etching rate of polymer in etchant varies with the degree of polymerization. In the following we will present the detailed fabrication and etching process with characterization of the etching selectivity based on the theory of photo-polymerization and experiments.

3.2 METHOD AND MATERIALS

One of the advantages of digital masks over physical masks is that the former can create grayscale exposure light field. However, the physical masks can only create black and white, binary exposure light intensity field. The dynamic mask used in our system is a reflective LCD panel since reflective LCD panels are cheaper and easier to be integrated with optics than DLP panels. Although LCD panels usually show a higher dark field light intensity than DLP panels, we control our incident light source such that the dark field intensity ($<0.2 \text{ mW/cm}^2$) is lower than the threshold ($\sim 0.3 \text{ mW/cm}^2$) of photo-polymerization during an exposure time of 20 seconds. The light intensity distribution of the reflected beam from the LCD panel is closely proportional to the grayscale distribution of the digital mask. It is well known that the degree of irradiation polymerization is related to the incident light intensity. The grayscale of digital mask provides the opportunity to control the degree of polymerization locally, therefore control the etching rate of polymer in the etchant. The etching rate will decrease as the degree of polymerization increases. The quantitative study on the etching selectivity will be presented in next section.

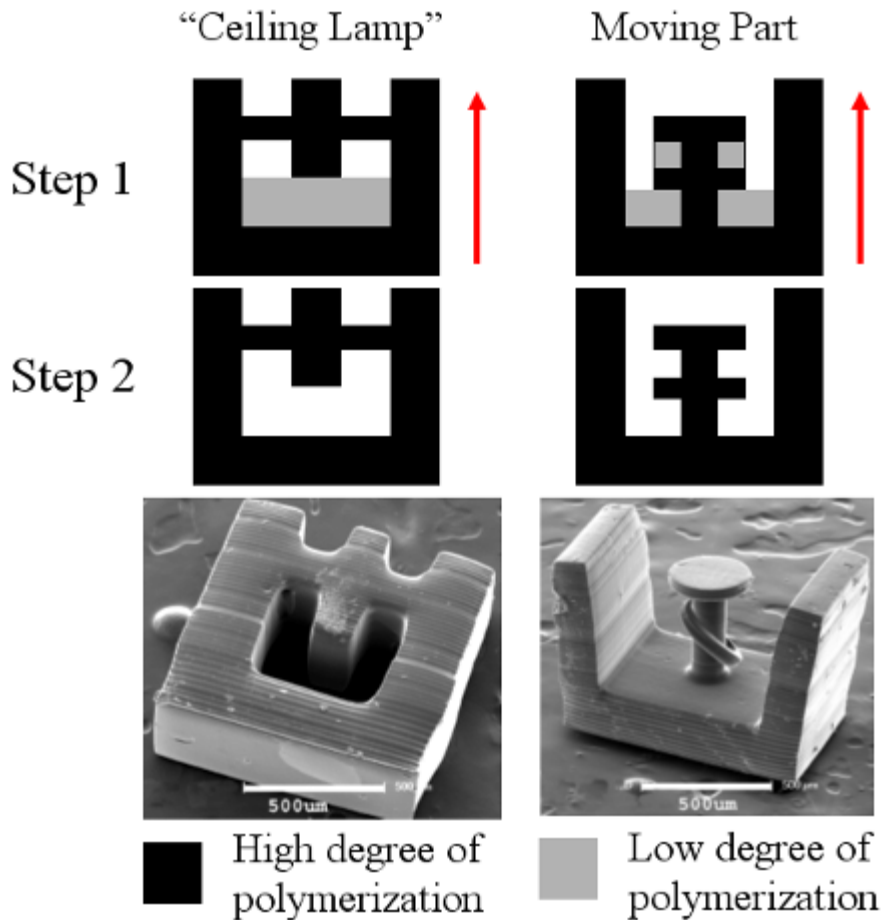


Figure 3.3 Schematic drawing of fabricating “ceiling lamp” and moving part with sacrificial structures in P μ SL. In step 1, the designed micro structures are fabricated using P μ SL. The sacrificial structures are polymerized using lower grayscale which will result in lower degree of polymerization. In step 2, the sacrificial structures are etched away and release the free standing structures and the moving part. The red arrow indicates the fabrication direction. Scale bar are 500 microns.

In this work, we use 1, 6-hexanediol diacrylate (HDDA) (SR238, Sartomer) and Ciba Irgacure819 as initiator. The wave length is 436 nm and the light intensity for a white digital mask is 3.32 mW/cm². The etchant is piranha solution composed of one volume of 96% sulfuric acid and one volume of 30% hydrogen peroxide. It is commonly used to clean the residual polymer on silicon wafers. Figure 3.3 schematically shows the process of fabricating the overhung micro structure and the micro moving part with sacrificial

structure. The actual finished samples are also shown. After the whole 3D structure is finished by P μ SL process, it is placed in acetone covered from light for 24 hours at room temperature to remove the residue monomer in the structure. We find that a portion of the sacrificial structure is dissolved during this step. The dissolved part usually is close to the edges of the sacrificial structure, where the degree of polymerization is even lower than the center area. After removing the residue monomer, the sample is placed in the etchant for a few hours, depending on the size of the sacrificial structure. The temperature of the etchant is set to 70 °C, while it is stirred on a magnetic hot plate.

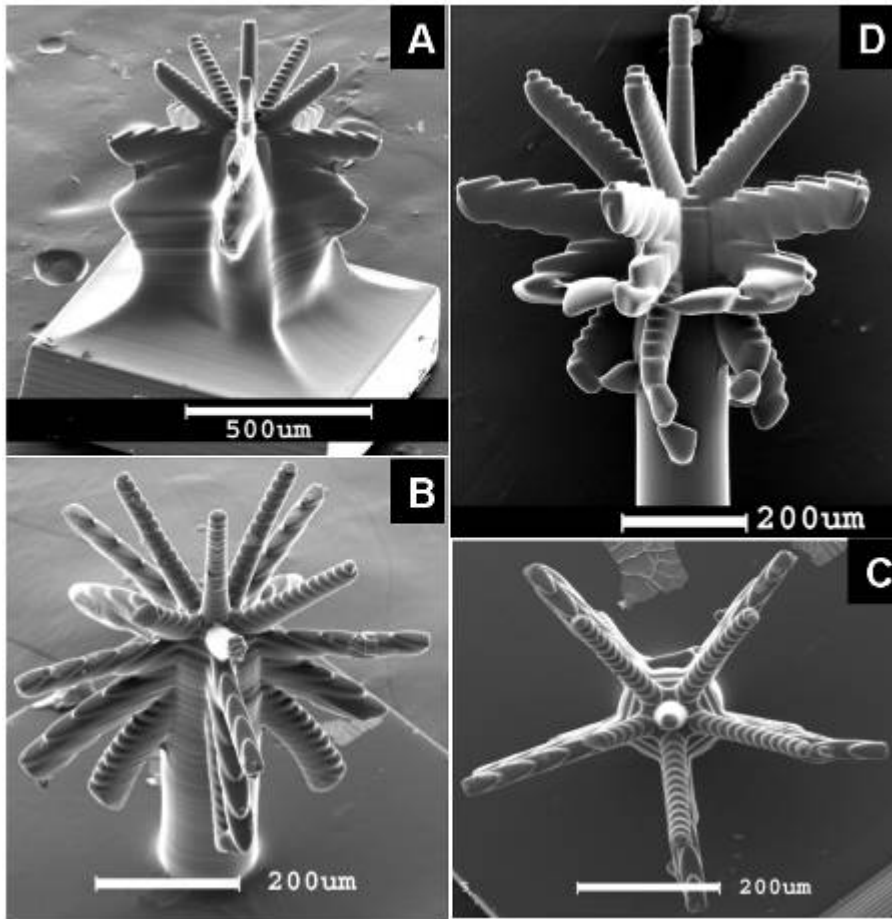


Figure 3.4 A. Micro-fabricated hair tree after acetone treatment but before acid etching, part of the sacrificial structure has been removed by acetone. B. Side-view of hair tree after acid etching. C. Top-view of hair tree after acid etching. D. Side-view of hair tree after acetone treatment without using sacrificial structure.

Figure 3.4 shows the micro fabricated fully 3D micro structure. This is a hair tree with hairs pointing to all directions. The diameter of the hairs varies from 60 μm to 100 μm and the layer thickness is 20 μm . It can be clearly seen (Figure 3.4D) that without sacrificial structure the disconnected elements float away randomly and collapse. But we can still find a portion of the hairs pointing to downward direction close to the center. This is because the region close to the center has higher light intensity and the sacrificial structure forms and later is removed by acetone. In contrast, the hair tree with grayscale sacrificial structures is built faithfully (Figure 3.4A, B, and C), demonstrating the effectiveness of this method. The dimension of the hairs varies less than 10% before and after etching.

3.3 SELECTIVITY WITH GRAYSCALE EXPOSURE

To design the grayscale level for the sacrificial structure, we study the relationship between the etching rate and the grayscale exposure created by the digital mask. Polymer etching is a process of breaking down the chemical bonds of the polymer chain. So the linear etching rate is a function of the density of the chemical bonds, especially in the case of surface etching. A surface etching mechanism is required for our fully 3D micro fabrication technology. Surface etching etches the surfaces but maintains the geometry of the micro structure, however bulk etching will break larger pieces into smaller pieces and destroy the integrity of the micro structure. In our preliminary studies, the specimen of photocrosslinked 1, 6-hexanediol diacrylate submersed in the etchant only appears smaller in dimensions over extended time rather than disintegrates. This implies surface etching is dominant in this process. The density of the chemical bonds is proportional to the amount of polymerized monomer in one unit volume of starting monomer which is

the degree of polymerization. Two parameters are controllable in our method, light intensity and exposure time for each layer. The light intensity is controlled by the grayscale of the digital mask and the exposure time is controlled by the time that digital mask is displayed on the LCD panel. In the rest of this section, we develop a semi-empirical theory to describe the selectivity of the etching.

The chemical reaction in PμSL is a radical chain polymerization. Because the volume of the resin is much larger than the volume of micro structure, to a very close approximation, the starting monomer and initiator concentration are assumed to be same for each layer. The whole fabrication process is done at a constant room temperature. So we also assume the reaction temperature does not change for each layer. And those temperature dependent parameters will be treated as constants in this analysis. With the assumption of steady state, the rate of photo-polymerization for unsaturated monomers has form [8]:

$$R_p = k_p[M]\left(\frac{\phi I_0(1 - e^{-\varepsilon[A]b})}{k_t}\right)^{1/2} \quad (3.1)$$

where k_p and k_t is the rate constant for polymer chain propagation and termination, respectively, $[M]$ is the monomer concentration, ϕ is the quantum yield for initiation, I_0 is the incident light intensity, $[A]$ is the concentration of species which undergoes photo-excitation, ε is the molar absorptivity (extinction coefficient) of A at the particular frequency of radiation absorbed and b is the thickness of reaction system being irradiated. The rate of polymerization is also call the rate of monomer disappearance, and it is given with very good approximation by [9]

$$-\frac{d[M]}{dt} = R_p \quad (3.2)$$

Combining Equations (3.1) and (3.2), the integration gives [Appendix]

$$[M] = [M]_0 \exp\left(-k_p \left(\frac{\varphi(1 - e^{-\varepsilon[A]b})}{k_t}\right)^{1/2} I_0^{1/2} t\right) \quad (3.3)$$

where $[M]_0$ is the initial monomer concentration. The difference of monomer concentration between the current solution and the initial one, $([M]_0 - [M])$, tells the amount of monomer polymerized. We further assume the etching rate of the photo-cured polymer varies linearly with the density of chemical bond (or polymerized monomer), then the etching rate can be expressed as [Appendix]

$$R_{etching} = C_1 \exp\left(-k_p \left(\frac{\varphi(1 - e^{-\varepsilon[A]b})}{k_t}\right)^{1/2} I_0^{1/2} t\right) + C_2 \quad (3.4)$$

where C_1 and C_2 are constants. C_2 is the etching rate at maximum degree of polymerization. Using fully polymerized disk with diameter of 5 mm and thickness of 1.76 mm, we measured $C_2 = 16 \pm 0.7 \mu\text{m/hr}$ when the sample was etched in the same etchant at the same conditions mentioned in last section for 5 hours. From Equation (3.4), we can see the controllable parameters in our method are the light intensity I_0 and the exposure time t . The etching rate changes exponentially with the product of square root of I_0 and t . To control the light intensity I_0 , we only need to display the digital mask of different grayscale levels. We have experimentally verified the power law dependence of the etching rate with I_0 and t in the following.

By rewriting Equation (3.4) and taking the natural logarithm on both sides, we can see:

$$\ln(R_{etching} - C_2) \propto I_0^{1/2} t \quad (3.5)$$

To study the exposure time dependency, we fabricate the sample as shown in Figure 3.5A with three identical arms for the statistical analysis purpose. The radiation time decreases

every ten layers by five seconds for each arm. The layer thickness is 20 μ m. The sample is etched for 30 minutes and dried in air for 12 hours. The width of each arm is measured before and after etching and the differences are taken for the analysis of the etching rate under different exposure time. The sample in Figure 3.5B has blocks fabricated using digital mask of different grayscale levels. Each layer is 20 μ m thick and is exposed for 30 seconds. Again, the sample is etched for 30 minutes and dried in air for 12 hours. The difference in the width of those blocks tells the etching rate under different grayscale exposure. From Figure 3.5, we can see the linear relationship in Equation (5). It means that the etching rate exponentially changes with the product of t and $I_0^{1/2}$ as theoretically expected. Based on this study of the etching selectivity, we use grayscale of 40 out of full scale of 255 (white) and the exposure time 10s for the sacrificial layer fabrication to ensure the success of the above samples fabrications. The light intensity of grayscale 40 corresponds to 0.37mW/cm². The ratio of the etching rate between sacrificial structures and micro structures is 10.

This technology is not limited to the same polymer and etchant mentioned above. Any photo-curable polymer undergoing surface etching in etchant is a valid candidate. However, like any micro fabrication technology, there are certain drawbacks with this technology. The surface roughness will increase to couple microns for 20-micron thick layers after etching. The reason is that for each layer there is also a gradient of degree of polymerization along the thickness direction. This will cause uneven etching on surfaces. Furthermore, the etchant for removal of crosslinked polymer usually is very corrosive. It will be a problem when the sample has to stay on some metallic substrates that are

subject to erosion. These are among the future efforts to be addressed in advancing this technology.

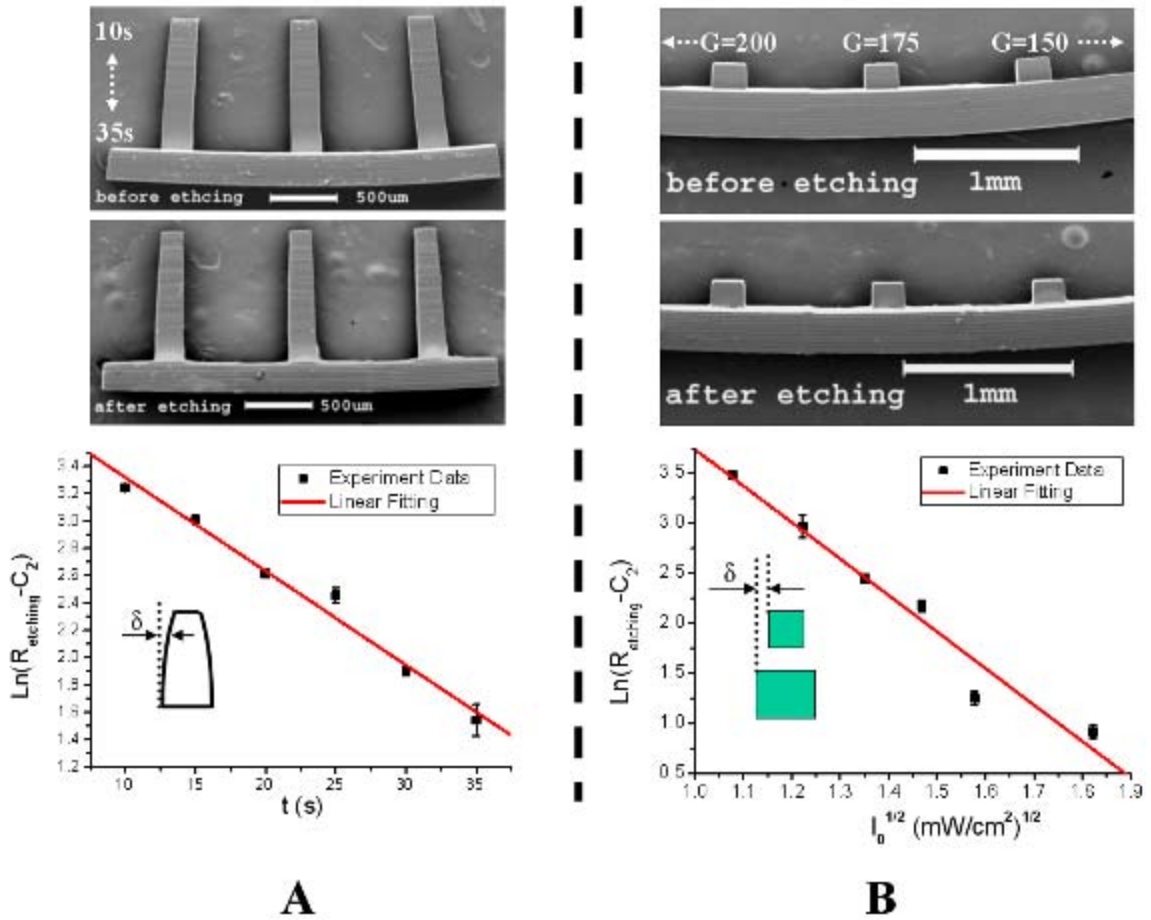


Figure 3.5 A. the experiment sample and the data of etching rate under different exposure time. B. the experiment sample and the data of etching rate under different exposure light intensity. The error bar is the standard deviation of multiple measurements. The unit for etching rate is $\mu\text{m}/\text{hr}$.

3.4 CONCLUSIONS

By taking the advantages of the digital mask, which not only allow one to quickly generate masks for the micro structure fabrication but also to control the gray scale of the mask where supporting structures are needed, gray scale sacrificial structure is introduced to fabricate fully 3D micro structures and micro moving parts in P μ SL. This novel

method not only inherits the parallel, high-resolution, broad-material-compatible characteristics of P μ SL, but further brings new capabilities to this technology. The sacrificial structure and the micro structure are fabricated simultaneously using the same material without reducing the high speed of P μ SL fabrication which is not possible for other micro fabrication methods. The theoretical predicted selectivity of the etchant to the partially crosslinked sacrificial parts were verified by measuring the etching rate as a function of photo-crosslinking light intensity and the light exposure time. Furthermore, the selectivity analysis is expected to explain a broader range of acrylated monomers. Finally, this technology will enable the fabrication of more complex scaffolds in tissue engineering and more sophisticated micro fluidic devices, such as the artificial 3D capillary network.

REFERENCES

- [1] Madou, M. J. 1997 Fundamentals of Microfabrication, *CRC Press*.
- [2] D. Westberg, O. Paul, G. I. Andersson, H. Baltes 1996 Surface micromachining by sacrificial aluminium etching *J. Micromech. Microeng.* **6** 376-84. [3] T.E. Bell, P.T.J. Gennissen, D. DeMunter and M. Kuhl 1996 *J. Micromech. Microeng.*, 6, 361.
- [4] A. Bagolini, L. Pakula, T. L. M. Scholtes, H. T. M. Pham, P. J. French, P. M. Sarro 2002 Polyimide sacrificial layer and novel materials for post-processing surface micromachining *J. Micromech. Microeng.* **12** 385-9.
- [5] G. M. Linder, V., Gates, B. D., Ryan, D., Parviz, B. A. and Whitesides 2005 Water-Soluble Sacrificial Layers for Surface Micromachining *SMALL* **1** 730-736. [6] Cabrera M, Bertsch A, Chassaing J, von Jezequel J y and Andre J C 1998 *Mol. Cryst. Liq. Cryst.*, 315, 223.
- [7] R W Johnstone, I G Foulds and M Parameswaran 2008 Self-sacrificial surface micromachining using poly(methyl methacrylate) *J. Micromech. Microeng.* **18** 115012
- [8] George G. Odian, principles of polymerization, 2nd edition, John Wiley & Sons, Inc.1981, p209-210
- [9] George G. Odian, principles of polymerization, 2nd edition, John Wiley & Sons, Inc.1981, p189

APPENDIX

In this appendix we will derive Equations (3.3) and (3.4) in the main text.

In a radical chain polymerization, monomer disappears by the initiation reaction as well as by the propagation reactions. The rate of monomer disappearance, which is synonymous with the rate of polymerization, is given by

$$-\frac{d[M]}{dt} = R_i + R_p \quad (3.6)$$

where R_i and R_p are the rates of initiation and propagation, respectively. However, the number of monomer molecules reacting in the initiation step is far less than the number in the propagation step for process producing high polymer. To a very close approximation the former can be neglected and the polymerization rate is given simply by the rate of propagation, which is Equation (3.2). By substituting the rate of propagation given by Equation (3.1) into Equation (3.2), we have

$$-\frac{d[M]}{dt} = k_p[M] \left(\frac{\varphi(1 - e^{-\varepsilon[A]^b})}{k_t} I_0 \right)^{1/2} \quad (3.7)$$

Integration of Equation (3.7) by separating variables yields

$$[M] = C_0 \exp\left(-k_p \left(\frac{\varphi(1 - e^{-\varepsilon[A]^b})}{k_t} \right)^{1/2} I_0^{1/2} t\right) \quad (3.8)$$

where C_0 is a undetermined constant. The initial condition

$$[M]_{t=0} = [M]_0 \quad (3.9)$$

gives

$$C_0 = [M]_0 \quad (3.10)$$

therefore we have monomer concentration in current solution

$$[M] = [M]_0 \exp\left(-k_p \left(\frac{\varphi(1 - e^{-\varepsilon[A]^b})}{k_t}\right)^{1/2} I_0^{1/2} t\right) \quad (3.3)$$

Assuming the etching rate of the polymer varies linearly with the density of chemical bond (or polymerized monomer), namely $[M]_0 - [M]$, then we have the etching rate

$$R_{etching} = \alpha([M]_0 - [M]) + \beta \quad (3.11)$$

where α and β are constants. By substituting Equation (3.3) into Equation (3.11), $R_{etching}$ becomes

$$R_{etching} = \alpha([M]_0 - [M]_0 \exp\left(-k_p \left(\frac{\varphi(1 - e^{-\varepsilon[A]^b})}{k_t}\right)^{1/2} I_0^{1/2} t\right)) + \beta \quad (3.12)$$

after rearrangement

$$R_{etching} = C_1 \exp\left(-k_p \left(\frac{\varphi(1 - e^{-\varepsilon[A]^b})}{k_t}\right)^{1/2} I_0^{1/2} t\right) + C_2 \quad (3.4)$$

where $C_1 = -\alpha[M]_0$ and $C_2 = \alpha[M]_0 + \beta$.

CHAPTER 4

3D MICROFABRICATED BIOREACTORS WITH CAPILLARIES

4.1 INTRODUCTION

Reconstructive surgeries are performed to recover the function and appearance of damaged tissues, especially following major cancer resections and traumas. It is estimated that more than one million reconstructive surgery procedures are performed by plastic surgeons every year. The development of reconstructive surgery [1] has proved the success of free flaps as reconstructive tissues for recipients. A free flap is a block of tissue with inherent microcirculatory network, usually is transferred from a patient's own body close to the defective site [2]. However, the nature of sacrificing one part of a body for another limits the application of free flaps in practice. Therefore alternative tissue sources for reconstructive surgery are desired. The field of tissue engineering [3] introduces the exciting possibility of replacing damaged body parts with new ones customized to the specific needs of the recipient, independent of the availability of donor sources. A number of tissue-engineered products are currently used clinically, such as IntegraTM, CarticeTM, and ApligrafTM. Further development of cell biology, micro-technology, and biomaterial science will provide new opportunities to create larger and more complex artificial tissues.

One of the major obstacles towards the creation of large complex 3D artificial tissues is the lack of microcirculatory system at the early stage of tissue culture [4]. The time scale for neo-vascularization is in the order of days (even with growth factors) and the time scale for cell death from hypoxia is in the order of hours. Therefore without

capillary perfusion, the metabolism during cell growth cycles will eventually exhaust the supply of nutrient and oxygen from the external environment and the embedded cells suffer from the lack of nourishment, creating a bottleneck for the growth of thick (>1 mm scale) 3D tissues. Studies [5, 6] confirm that cells in a tissue are poorly cultured when they are further than ~ 400 μm away from external nutrient sources. As a matter of fact, in real tissues, most of cells stay within a distance of about 100 μm from nearby capillaries [3]. Several research groups have developed methods to enhance the mass transport in tissue culture by taking advantage of current microfabrication technologies. For example, by inserting and extracting nylon strands and tubing, straight artificial blood vessels were created to allow the continuous perfusion of culture medium [7]. However, the assembly of many discrete micro blood vessels into an inner-connected 3D network for nutrient perfusion will not be practical. Griffith, et al [8] created 3D channels by 3D printing technology. Unfortunately, the resolution of this technology was only 200 μm , which is much larger than a capillary dimension (<20 μm). Silicon microfabrication technologies and molding were also able to create two dimensional micro channels for enhanced mass transport [9]. A recent study [10] shown a multi-culture system consisting of myoblasts, embryonic fibroblasts and endothelial cells co-seeded on highly porous, biodegradable polymer scaffolds could induce the endothelial vessel networks. However the scaffolds used in this work were less than 1 mm thick, which was still within the diffusion distance of external nutrients. Nevertheless, the three dimensional nutrient transport in thick ($>1\text{mm}$) tissue culture still remains a hurdle in tissue engineering.

To enhance the transport and exchange of nutrients and wastes for constructing thick artificial tissues, a novel three dimensional microfabrication technology, projection micro

stereolithography (P μ SL) [11], is introduced for the design and the fabrication of vascularized micro bioreactors. We show in this chapter such micro fabricated bioreactors, coupled with mass transport simulation, can dramatically enhance the nutrition and growth of cultured cells through capillary networks. This microfabrication method brings several unique advantages to the field of tissue engineering: first, the capability of P μ SL to build truly 3D sophisticated microstructures with very fine spatial resolution at micron scale; second, a significantly shortened design cycle enabled by high fabrication speed (200 layers in a couple of hours); finally, the choice of biocompatible and biodegradable polymers offers flexibility on fabricating implantable pre-vascularized scaffolds for different tissue cultures[12,13].

4.2 MICROFABRICATION AND MATERIALS

Not only is P μ SL capable of constructing 3D complex polymer capillaries with high resolution, it also offers potential of locally controlling the Young's modulus [14] and the permeability of polymer structures. The cross-linking ratio of photo-curable polymer increases as the exposure dose increases and finally reaches a plateau [15]. Meanwhile, the permeability of the photo-cured polymer is a function of cross-linking ratio, the permeability decreases as the cross-linking ratio increases (Figure 4.1). Therefore, by simply controlling the exposure dose for each layer and within each layer in the fabrication process, the permeability of 3D structures can be precisely, locally tuned in a 3D space. This technology has a great potential application of local delivery in tissue engineering devices.

P μ SL is compatible with various biomaterials of different functions, for example biocompatible and biodegradable polymers including Poly (ethylene glycol) (PEG), poly

lactic acid (PLA), poly caprolactone (PCL), and their copolymers. In this work, the monomer is a water-soluble PEG diacrylate (molecular weight 575, from Sigma-Aldrich, with viscosity 57cP at 25°C). Bis(2,4,6-trimethylbenzoyl)-phenylphosphineoxide (Irgacure 819, from Ciba) is used as the photo initiator. A small amount of UV absorber (0.5-0.8 wt %) is mixed with the PEG monomer to control the UV penetration depth in the solution.

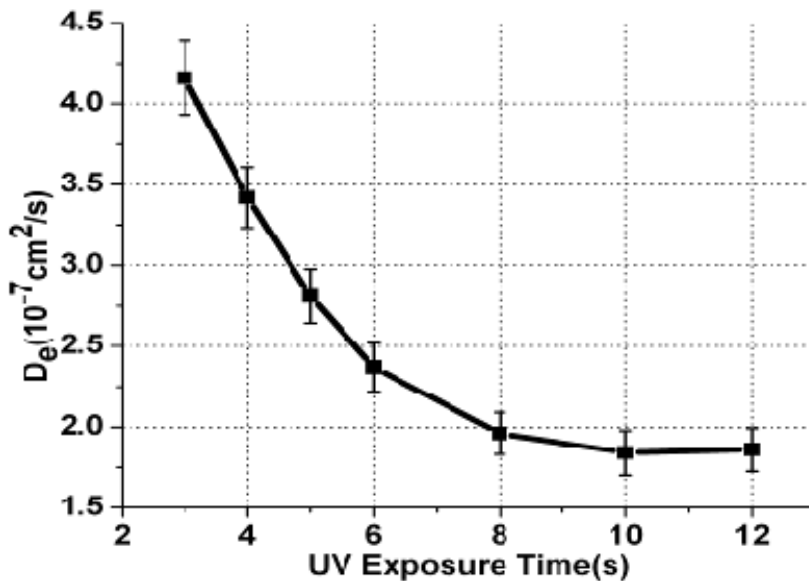


Figure 4.1 Experimental data of effective diffusion coefficient of ethanol in 200-µm thick PEG (MW575) films cured using different UV exposure time, temperature=20 °C. UV source for film fabrication: wave length=390 nm, intensity =1.1 mW/cm².

4.3 VASCULARIZED MICRO BIOREACTORS

During a tissue culture, it is very important that all the cells in the tissue are well fostered to reach high cell density. In normal tissue, most cells stay within around 100 µm to blood vessels, because the nutrients are depleted at this distance. This means for active tissues, the capillary network has to be dense enough to balance the consumption during cell metabolism. Similarly, in our micro-bioreactor design, we try to mimic the

real nutrient delivery using a dense capillary network. However, due to the theoretical complexity of branching capillary structure, parallel straight capillary system is preferred in this work. Approximately, a real capillary can be regarded as an assembly of many segments of straight capillaries. Therefore we designed and fabricated the micro bioreactor using P μ SL as shown in Figure 4.2. The capillaries are 800 μ m long with 20- μ m inner radius and 40- μ m outer radius, the distance between the nearest points of two adjacent parallel tubes is 40 μ m. Two ring structures as “artery” and “vein” are connected to the bioreactor chamber which is filled with parallel capillaries. The external nutrient supply will be connected to these two rings which have 400- μ m inner diameter. Figure 4D shows the cross-section view of a micro-bioreactor. Since the volume of the reactor is only 0.13 μ L, it allows culturing about 1,300 cells at the level of 10^7 cells/mL.

Instead of trial and error in culture experiments, we apply numerical method to study the mass transport by a PEG micro-tube which will eventually guide our bioreactor design and cell culture experiment. Without studying the kinetics of tissue growth or cell proliferation, the purpose of this numerical method is to design the right dimensions and density of artificial capillaries, such that all cells in the bioreactor are well nourished even at maximum cell density. Therefore, as a “worst case scenario”, we assume the cell density is at the maximum value which is derived from the average cell size in the case of yeast culture. The capillaries are arranged in a hexagonal array as shown in Figure 4.3A. The simulation is based on one single capillary supported by thick polymer structures. Figures 4.3B and 4.3C show the geometries of the model and the reduced simulation domain according to the symmetry of the model. In the numerical study we further take the following assumptions:

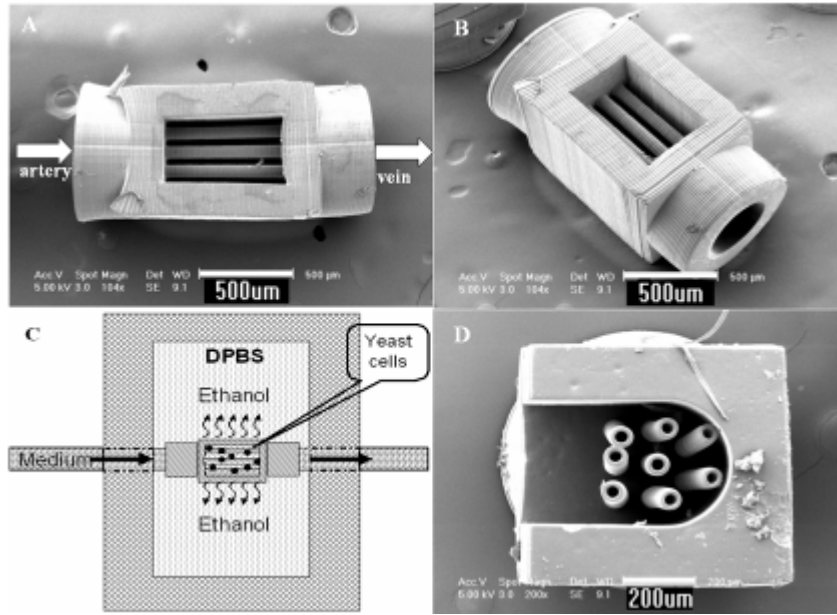


Figure 4.2 A, B, D. different views of a micro-bioreactor; C. yeast cell culture device, the culture medium is pumped from external pipe through the polymer capillaries in the micro-bioreactor. The bioreactor is submerged in DPBS (Dulbecco's Phosphate Buffered Saline) solution. When the culture medium flows through the capillaries, it will diffuse out through the wall of capillaries. The glucose metabolism of yeast cells will produce ethanol which will diffuse into the DPBS solution.

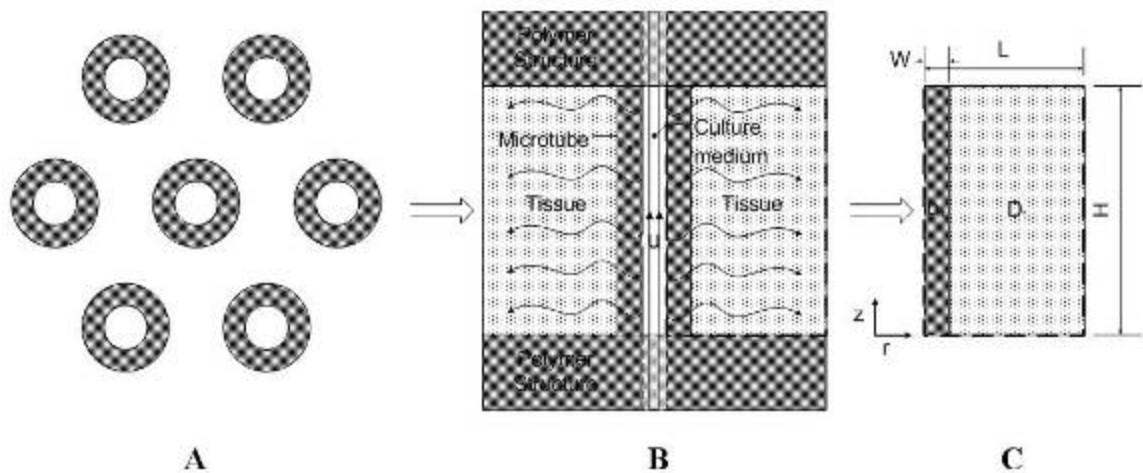


Figure 4.3 Simulation model for hexagonally arranged capillaries.

- Polymer structures are thick compared with the thickness of capillary wall. The rate of nutrient species diffusion in polymer is much slower than that in tissue by nearly one order. Therefore we neglect the diffusion through the polymer structure.

- The nutrient concentration in capillaries only changes along the axial direction. Advection transport dominates in capillaries.

- Diffusion transport dominates within the wall of capillaries and tissue, no advection in these regions. This can be regarded as “worst-case scenario” design. The actual advection effect will only increase the mass transport, so it will not fail the design.

- The final mass transport distance is determined at the steady state when the number and density of cells reach the maximums. So in the simulation we assumed that the mass transport is steady.

4.3.1 Governing equations

Adopting a nutrient consumption model of cells, the simulation tells the distribution of nutrients in the micro-bioreactor which is full of cells. Basically, it is a diffusion limited problem with static governing equations:

$$D_{pi} \nabla^2 c_i = 0 \quad \text{In capillary wall} \quad (4.1)$$

$$D_{ii} \nabla^2 c_i - R_i = 0 \quad \text{In cell suspension} \quad (4.2)$$

Here D_{pi} , D_{ii} are the diffusion coefficients for metabolite species i in polymer and in tissue respectively, they are assumed to be constant. c_i and R_i are the concentration and consumption rate of species i . In the case of steady state, the process of cells consuming metabolites is often described by Michaelis-Menten kinetics [17, 18]:

$$R_i = \frac{V_{\max} c_i}{K_M + c_i} \quad (4.3)$$

Where V_{\max} is the maximal uptake rate and K_M is the metabolite concentration when the uptake rate is half of the maximum. In Michaelis-Menten kinetics, the consumption behavior follows first order kinetics at low concentration. That means the consumption rate is proportional to the concentration. But there is a threshold at which cells start to starve. As a rule of thumb, condition $c_i = K_M$ is often used. We adopt this condition to determine the boundary of mass transport distance. As the concentration of metabolites increases, the consumption behavior will become zero order kinetics gradually. At a certain point, the cell is saturated and the intake of metabolites reaches a plateau.

Finally the 2D governing equations in cylindrical coordinates are as followings:

$$D_{pi} \left(\frac{\partial^2}{\partial r^2} + \frac{1}{r} \frac{\partial}{\partial r} + \frac{\partial^2}{\partial z^2} \right) c_i = 0 \quad r_0 \leq r \leq r_0 + W \quad (4.4)$$

$$D_{ii} \left(\frac{\partial^2}{\partial r^2} + \frac{1}{r} \frac{\partial}{\partial r} + \frac{\partial^2}{\partial z^2} \right) c_i - \frac{V_{MAX} c_i}{K_M + c_i} = 0 \quad r_0 + W \leq r \leq L \quad (4.5)$$

4.3.2 Boundary conditions

We have assumed that no mass transports through the polymer structures. Therefore no mass flux is perpendicular to the polymer structure surfaces. This will introduce two boundary conditions:

$$\frac{\partial c_i}{\partial z} = 0, \quad z = 0, H \quad (4.6)$$

At $r = L$, we imposed condition $\frac{\partial c_i}{\partial r} = 0$. This can be explained that $r = L$ is a surface of

polymer structures or the simulation domain is large enough that the concentration

around here is constant zero or this is a symmetric point. But to find the mass transport distance, the simulation domain should be large enough to reach constant zero concentration regions.

According to the assumption that the concentration of metabolites in the tube only changes along the axial direction, also the concentration is very low (100nmol/mL), the consumption of metabolite will not change the volume of the culture medium appreciably.

Then we have the boundary condition based on mass conservation:

$$\frac{\partial c_i}{\partial z} - \frac{2D_{pi}}{ur_0} \frac{\partial c_i}{\partial r} = 0, \quad r = r_0 \quad (4.7)$$

Here u is the velocity of culture medium flow in the tube.

Finally, at the interface of wall of capillary and tissue, two different materials are next to each other with distinct permeability. In order to fulfill the mass conservation law, we introduced the jump condition:

$$D_{pi} \left(\frac{\partial c_i}{\partial r} \right)^- - D_{ti} \left(\frac{\partial c_i}{\partial r} \right)^+ = 0, \quad r = r_0 + W \quad (4.8)$$

The “-” and “+” stand for the values on different sides of the interface. The physical interpretation of this condition is that the mass flux at the two sides of the interface should be equal.

4.3.3 Results based on oxygen transport

Equation (4. 4) combined with (4. 5) is a nonlinear system. We used 3-point central difference scheme in the simulation domains (wall of capillary and tissue) and 5-point bias difference on boundaries. Newton iteration was implemented. We simulated the oxygen transport which was almost always the main factor limiting the size of engineered

tissue structure [3]. The typical diffusion coefficient of oxygen in a tissue at 37°C was from [3], the inlet oxygen level was set to be the arterial oxygen level. Assuming the cells were hepatocytes and the density level was 10^7 cells/mL. The diffusion coefficient of oxygen in polymerized PEG was conservatively estimated from [19] considering the oxygen molecule is much smaller than bio molecules. The parameters used in the simulation are listed in Figure 4.4. Due to the oxygen consumption outside the tube, the oxygen concentration in the tube gradually decreases from inlet to outlet. As a result, the oxygen diffusion distance decreases along the same direction. The diffusion distance at the outlet is used to design the spacing between capillaries in the bioreactor.

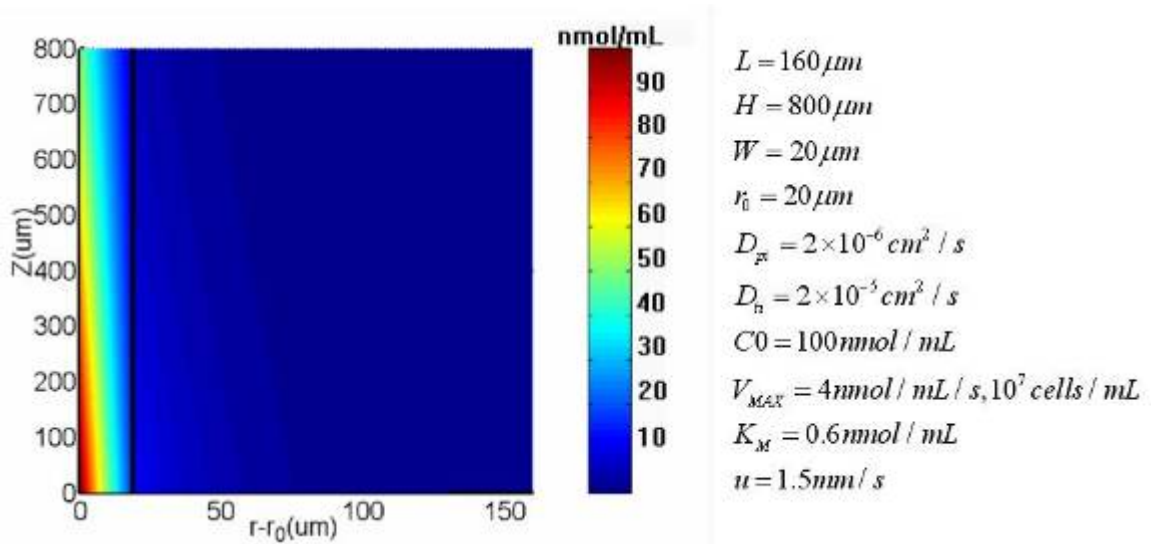


Figure 4.4 The distribution of oxygen concentration in the wall of a capillary and in the tissue. The black line indicates the interface of the wall and tissue. The simulation parameters are also listed.

With the listed simulation parameters, the diffusion distances truncated according to the hypoxic condition $c_i = K_M$ at the inlet is 74 microns, and 48 microns at the outlet. It is clearly shown in Figure 4.5A that the concentration of oxygen decreases dramatically (~90%) through the wall of capillaries. This is due to the much smaller diffusion

coefficient of oxygen in PEG. To increase the oxygen concentration reaching the tissue under certain perfusion concentration, there are two ways: one is to reduce the thickness of the wall, but this will also reduce the mechanical capability of capillaries. The capillaries need to be strong enough to sustain the pressure during culture medium perfusion. The other way is to increase the diffusivity of polymers by selecting potential

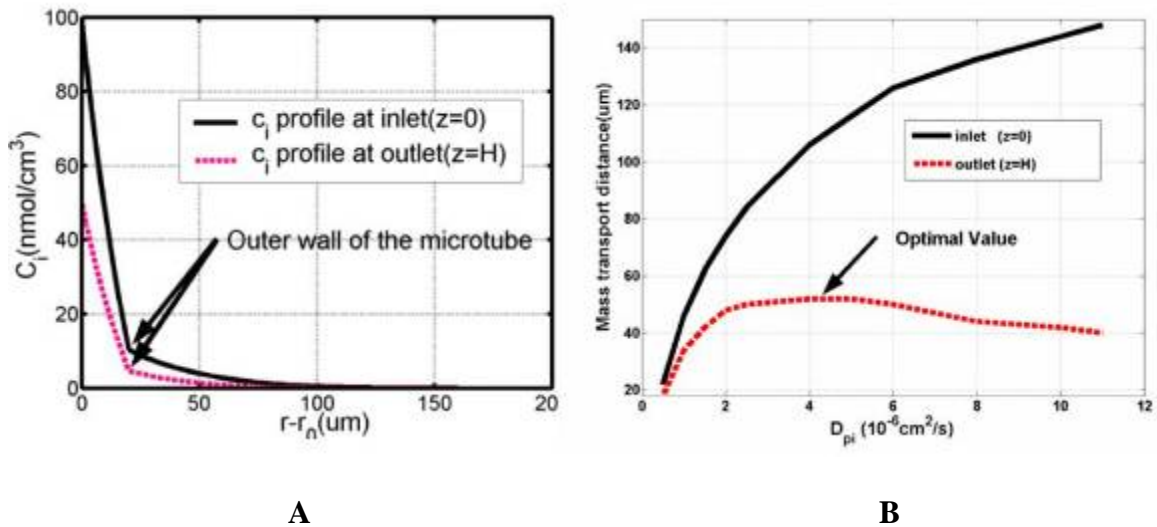


Figure 4.5 A. The profiles of oxygen concentration at the inlet and outlet of a capillary. B. The diffusion distance of oxygen at the inlet and outlet of a capillary as the diffusion coefficient changes.

polymers with higher permeability or increasing the porosity of selected polymer.

However, a higher permeability of polymer is not always better. The reason is that for capillaries of certain length H , a too high permeability will cause too much “upstream” consumption and the oxygen concentration in capillaries will decrease quickly. This will eventually decrease the mass transport distance at “downstream”. However the distance between parallel capillaries in a micro bioreactor is determined by the mass transport distance at the downstream outlet. So there is an optimal diffusion coefficient for the polymer selection. Figure 4.5B shows the phenomenon, the blue line is the mass transport

distance at the inlet and red line for outlet. As the diffusivity of the capillary material increases, the mass transport distance increases monotonously at the inlet, however the transport distance at the outlet increases first, then at a certain point ($\sim 4 \times 10^{-6} \text{ cm}^2 / \text{s}$) it starts to decrease, this is the optimal diffusion coefficient for this specific tube geometry.

4.3.4 Chinese hamster ovary (CHO) cell culture

Based on the oxygen simulation, we conservatively designed two kinds of bioreactors by arranging capillaries closer than simulated: one is with capillaries of 120- μm center-to-center distance, 40- μm ID and 50- μm OD, called type I from now on; the other one is with capillaries of 120- μm center-to-center distance, 60- μm ID and 80- μm OD, called type II from now on. We will use these two kinds of bioreactors for the first mammalian cell culture.

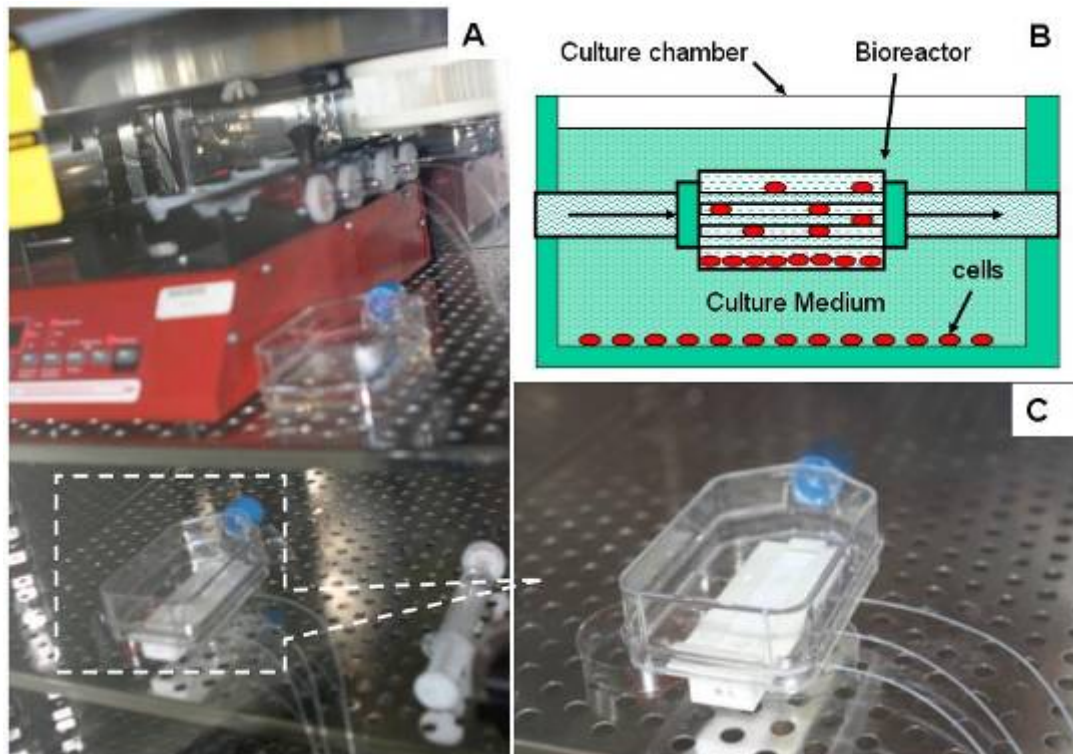


Figure 4.6 CHO cell culture system

Most of mammalian cells, such as endothelial cells, are anchorage dependent. They need to attach to proper extra cellular matrix (ECM) for normal growth. Therefore the bioreactor not only transports nutrients but also serves as an ECM or a scaffold. Since Chinese hamster ovary (CHO) cells are the most widely used mammalian cells for transfection, expression, and large-scale recombinant protein production. As a start, we choose CHO-K1 (from ATCC) cell whose growth is anchorage dependent to study the functionality of our vascularized micro bioreactors. The culture system is shown in Figure 4.6A. The whole system sited in a humidified CO₂ incubator. A multi-syringe pump was connected with a multi-chamber culture device using polyethylene tubing. The culture device was made of Teflon and it was covered by a conventional culture flask for gas exchange during the cell culture (Figure 4.6C). The micro bioreactor was fixed in the culture device by connecting to the metal tubes extruding from the walls of the culture device as shown in Figure 4.6B. The culture medium covered the top of the bioreactor after the cell seeding. The medium was standard F12 culture medium plus 10% bovine serum and antibiotic. The material of the bioreactor was PEG which was not self cell adhesive. Therefore to change the surface property of PEG for cell anchorage, the bioreactor was soaked in Poly-L-lysine (0.5M from Sigma-Aldrich) solution for 12 hours and rinsed using culture medium for 20 seconds before use. After the bioreactor was connected to the device, the cell-free culture medium in the bioreactor was removed using an absorbing paper before 1 μ L CHO cell suspension (2×10^6 cell/mL) was seeded. There were about 100 cells trapped in the bioreactor. Fresh culture medium was topped to cover the cell-seeded bioreactor, after which the medium started to be pumped through the capillaries. As a comparison, control experiments were also conducted at the same

time with all conditions identical except without medium perfusion. The humidified incubator was set to 37°C and 5% CO₂. The medium flow rate was 5 μL/min. On the fourth day, the perfusion was stopped and the cells were stained using Cell Tracker Blue CMAC from Invitrogen and following the staining manual. The images were taken on Zeiss Axiovert 200M fluorescent microscope. The results using type II bioreactor are shown in Figure 4.7. The bright blue areas are CHO cells. The two images on the left (Figure 4.7 A and C) are taken at different height of the bioreactor. The other two on the right (Figure 4.7 B and D) are control experiments taken at the same height.

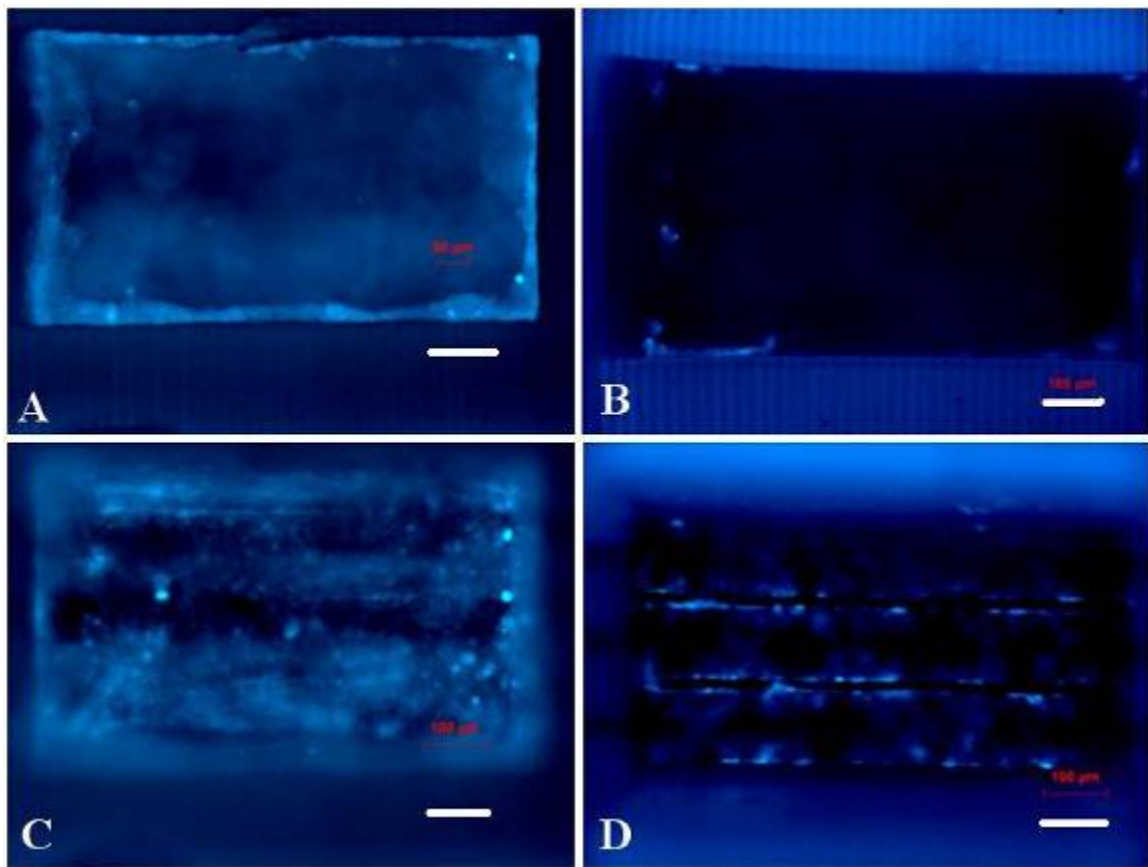


Figure 4.7 CHO cell culture in type II bioreactor. A,C. Results of perfusion culture; B,D. Results of control experiment without perfusion. The scale bars are 100 μm.

Figure 4.7A was focused at the entrance of the opening and we can see layers of CHO cells attaching to the walls. Figure 4.7C was focused right on top of the first layer of capillaries. It showed the live CHO cells covering the capillaries. However in the control experiment (Figure 4.7 B and D), there was only very weak florescent signal and we could barely see any cell. Therefore, the medium perfusion in capillaries played a very important role in the survival of cells in the bioreactor by providing them nutrients through the diffusion of capillaries. In perfusion culture, the seeded CHO anchored and proliferated on the inner surfaces of the bioreactor. A lot more CHO cells clustered together, which created a cell density close to 10^8 cells/cm³. This high density has rarely been seen in conventional 2D cultures. Although we were not able to count the number of cells in the bioreactor from the florescent images, we could still tell that it was much more than 100 cells which were originally seeded. CHO cell culture was also carried out in type I bioreactor which had smaller capillaries. The medium perfusion was stop at the 6th day. The results are shown in Figure 4.8. Looking from the top of the bioreactor, Figure 4.8A was focused right at the top of the first layer of capillaries and Figure 4.8B was at the same height taken in the control experiment which was without medium perfusion. PEG is transparent to visible light. This provided the opportunity of observing the distribution of CHO cells through the sidewall of the bioreactor (Figure 4.8C). Again we hardly saw cells in the control experiment. Comparing with type II bioreactor, there were less cells in the type I bioreactor even the culture in the latter one took longer time. This could be contributed to the smaller size of capillaries which provided less culture medium to the cells in the bioreactor.

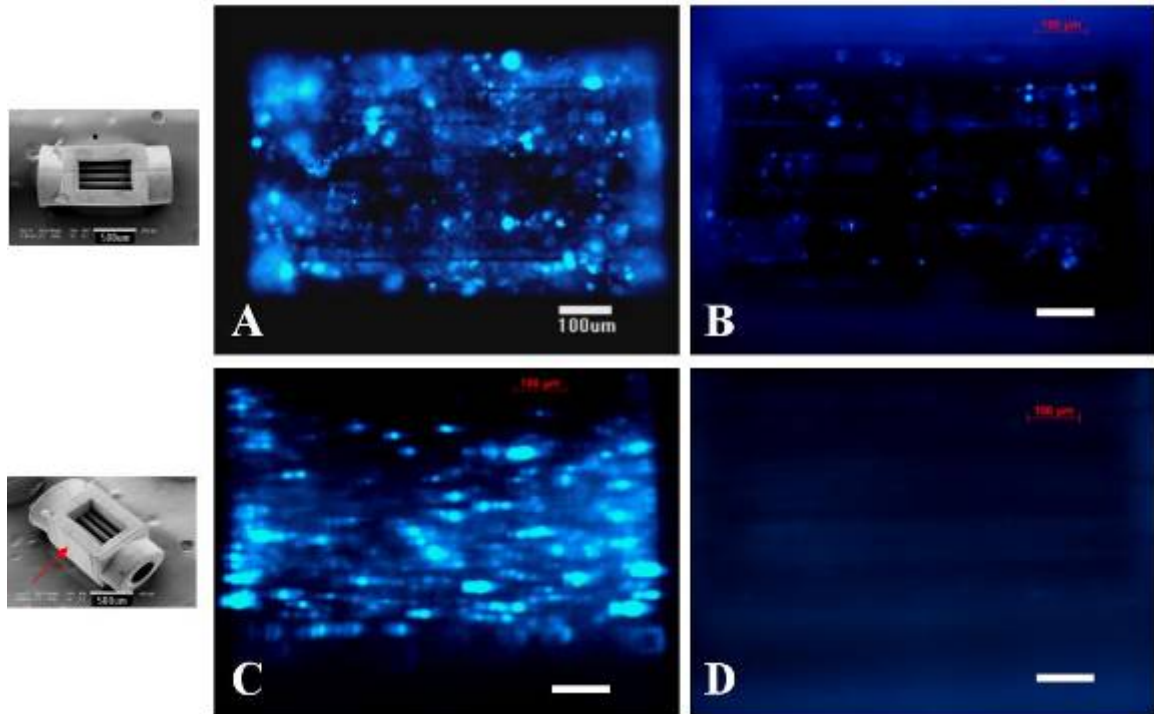


Figure 4.8 CHO cell culture in type I bioreactor. A, C. Results of perfusion culture; B, D. Results of control experiment without perfusion. The scale bars are 100 μm .

4.3.5 Results based on the glucose consumption of yeast cell

Yeast cell *Saccharomyces cerevisiae* is well studied of their growth cycles, so we used it as another model to testify the function of our micro-bioreactors. *S. cerevisiae* cell growth has two phases: Glucose is first catabolized fermentatively into carbon dioxide and ethanol (Phase I), and then when the glucose is limited ($<830 \text{ nmol/mL}$), ethanol is respired to carbon dioxide and water with the presence of oxygen (Phase II). The biomass production rate in Phase II is much slower than that in Phase I [20]. Therefore, we can neglect the biomass produced in Phase II. Furthermore, in our experiment we will try to inhibit Phase II metabolism by removing the ethanol. The effective diffusion coefficient of glucose in crosslinked PEG (MW575) is measured using the method mentioned in [21]. The flow rate in the channels is set at 0.5 mm/s. The Michaelis kinetic constants

V_{MAX} and K_M are from [20]. The average protein and biomass weight of single *Saccharomyces cerevisiae* yeast are 6×10^{-12} g and 15×10^{-12} g [22], respectively. From our scanning electronic microscopy measurement, the diameter of our cultured *S. cerevisiae* yeast cells (strain INVSc1) is $3.14 \pm 0.61 \mu\text{m}$ (Figure 4.9). When the cells are packed together in a most insufficient way which is cells occupy the eight vertices of a cube, then the cell density is $3.2 \times 10^{10}/\text{mL}$. The other simulation parameters are set as follows: $D_{pi}=1.1 \times 10^{-9} \text{ cm}^2/\text{s}$, $D_u=1.1 \times 10^{-6} \text{ cm}^2/\text{s}$ [23], $C_0=110 \mu\text{mol}/\text{mL}$ (concentration of glucose in polymer capillaries), $V_{MAX}=663 \text{ nmol}/\text{mg protein}/\text{min}$, $K_M=76 \mu\text{mol}/\text{mL}$.

Our simulation indicates that the bottleneck of effective glucose transport is the permeability of polymer capillaries. The glucose concentration drops off more than 90% after diffusing through the capillary wall. The simulation shows that if the center to center distance of the capillaries is set to $120 \mu\text{m}$ and the wall of the capillary is $10 \mu\text{m}$, then the inner radius of the capillary has to be larger than $20 \mu\text{m}$ to ensure that all the yeast cells in the bioreactor has a high enough ($>830 \text{ nmol}/\text{mL}$) glucose concentration to stay in the mixed respiro-fermentative metabolism and produce ethanol (Figure 4.9). This configuration corresponds to $80.2 \text{ capillaries}/\text{mm}^2$ if capillaries are in hexagonal arrangement. By increasing the inner radius of the capillary, not only the perfusion of the culture medium is increased, but also the gap between capillaries is decreased. It is equivalent to increase the density of the capillary. When the inner radius is $20 \mu\text{m}$, the lowest glucose concentration in the bioreactor is $880 \text{ nmol}/\text{mL}$. Further decreasing the inner radius of capillaries will decrease the glucose concentration in the bioreactor and force some yeast cells start to consume ethanol [20, 24]. The biomass growth becomes much slower than at a higher glucose concentration. Two experiments at different points

of the simulation curve are also shown in Figure 4.9. Experiment A is in the Phase I region that the glucose concentration in the bioreactor is much higher than 830 nmol/mL. Experiment B is at the cutoff region between Phase I and Phase II. We observed dramatic difference of the biomass production (Figure 4.9B and 5C). Actually in experiment A (Figure 4.9B), the yeast cells filled the whole bioreactor and even pushed the cells on top out of the bioreactor during culture. When the bioreactor was removed from the culture chamber, the top layers of yeasts were washed away. However, experiment B (Figure 4.9C) shows the exact amount of yeast that we achieved. According to the simulation, in experiment B, the yeast cells should also have fully filled the bioreactor as shown in experiment A. We contribute this error to a low glucose concentration in the bioreactor right after the cell seeding. In experiment B, the capillaries were sparser than that in experiment A. Without cells blocking the way, the glucose diffusing from the capillary quickly escaped from the bioreactor, causing a too low glucose concentration to keep the proliferation of yeast cells. A more detailed model to better capture the real time growth of yeast cells in bioreactors will be our future efforts.

During the growth of yeast number in the bioreactor, the yeast cells did not consume all the glucose diffusing from the capillaries. Therefore, some glucose leaked from the bioreactor and dissolved in the DPBS solution. As a result, the glucose concentration in the DPBS solution increased. The amount of glucose leaking from the bioreactor depended on how many cells were in the bioreactor. The more cells the less leaking, thus the glucose concentration in the DPBS solution increased slower. Figure 4.10 shows the average rate of glucose concentration in the DPBS solution in experiment A (Figure

4.9B). The average rate of glucose concentration is calculated by dividing the difference of glucose concentration by the time between current and last measurements. From

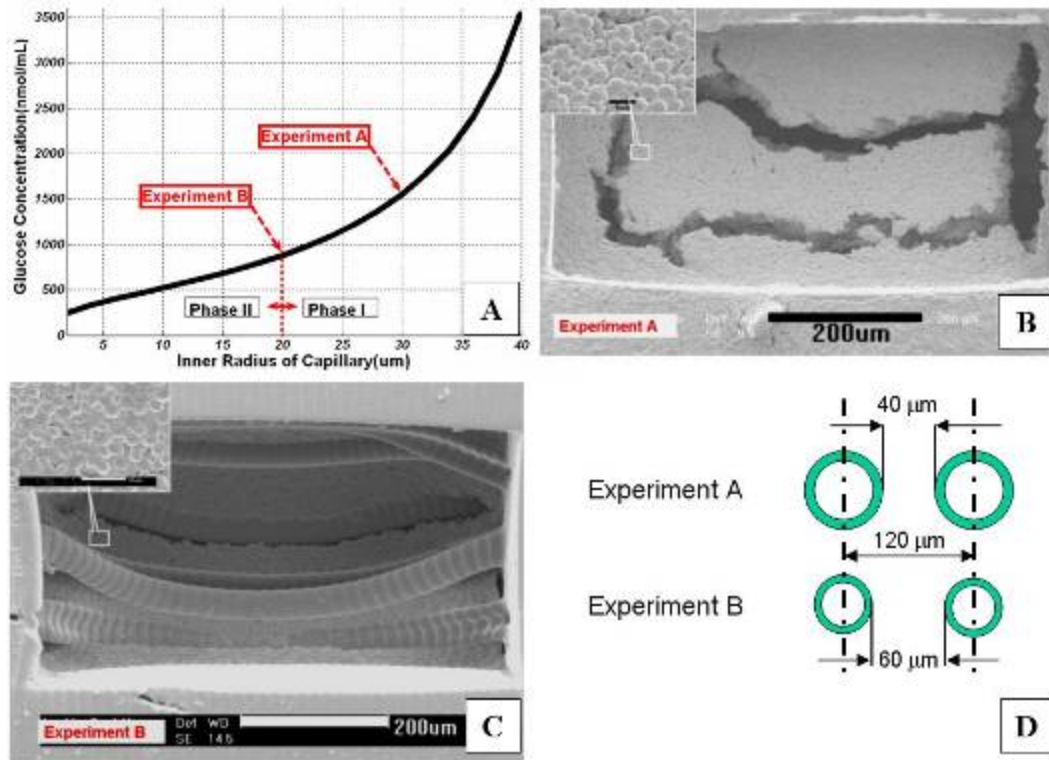


Figure 4.9 A. Simulation results indicating the minimum glucose concentration in a bioreactor increases as the inner radius of capillaries increases. B, C and D. Two experiments based on yeast model were conducted to verify the simulation. In experiment A, the inner radius of capillaries was 30 μm , the glucose concentration in a bioreactor was within Phase I metabolism of yeast such that the number of yeast cells grew fast and filled the whole bioreactor. The cracks were due to the collapse of capillaries when the sample was dried in air. In experiment B, the inner radius of the capillary was 20 μm . The glucose concentration in the bioreactor decreased and we saw much less yeast cells in the bioreactor. The center-to-center spacing of capillaries was 120 μm ; the thickness of capillary wall was 10 μm .

Figure 4.10, in experiment A, the yeast population in the bioreactor kept increasing during the culture. The glucose rate decreased almost 10 times, but the actual number of yeast increased more than 10000 times. We attribute this discrepancy to two possible reasons: First, in Michaelis-Menten kinetics, the glucose consumption rate of yeast varies with the local glucose concentration. The increase of yeast population in the bioreactor

changed the glucose distribution and thus changed the overall relationship of yeast number and glucose consumption which was not linear. The other reason is that not all the yeast cells were consuming glucose at the end of experiment. The yeasts on top were too far away from the capillary, such that the local glucose concentration was too low for the yeast to do glucose metabolism [20].

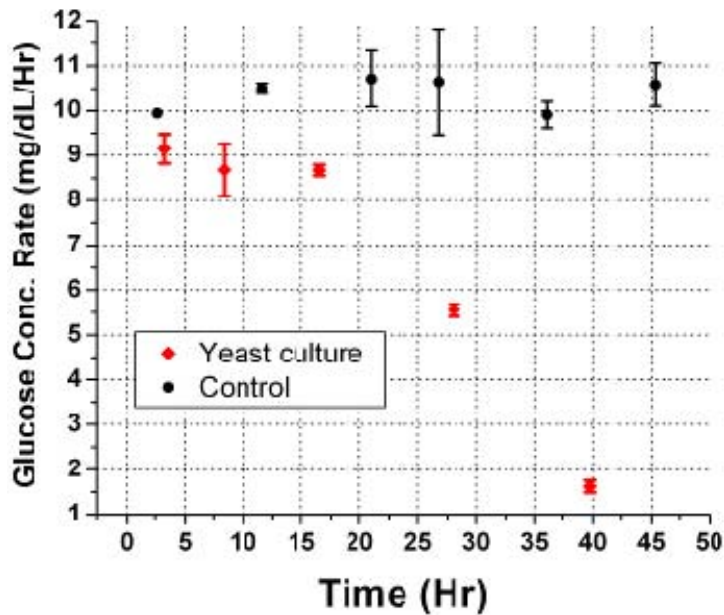


Figure 4.10 The average increasing rate of glucose concentration in the DPBS solution.

4.4 METHODS

4.4.1 Measurement of effective diffusion coefficient of ethanol in PEG membranes

We measured the effective diffusion coefficient of ethanol in PEG membranes using the Kaufmann-Leonard method [21]. Two identical stirred compartments were filled with deionized water and 50 w% ethanol water solution. These two compartments were separated by a 200- μ m PEG membrane which was fabricated by UV-polymerizing a

layer of PEG diacrylate solution between two glass slices. The motor stirred at a rate of 1Hz. After 10 minutes, the concentration of ethanol in deionized water was measured using QED alcohol test kit (OraSure Technologies, Inc.). Since the change of ethanol concentration in both compartments was very small compared to 50 w% ethanol solution, we assumed the diffusion mass flux $= -D_e \times C_0 / d$ was constant during the measurement. Here D_e is the effective diffusion coefficient; C_0 is the concentration of ethanol in 50 w% ethanol solution and d is the thickness of PEG membranes. Therefore D_e can be calculated from equation $\delta m = D_e \times C_0 \times \delta t / d$. Here δm is the amount of ethanol in deionized water during a time period of δt .

4.4.2 Yeast cell culture

The yeast we used was diploid strain INVSc1 (Invitrogen). Before yeast culture, the bioreactors were fabricated using P μ SL and kept in 100% ethanol for 24 hours and biology grade water for 24 hours to remove the residue monomer and initiator, also to increase the permeability of the capillaries. The yeast suspension in 1.5 mL microcentrifuge tube was moved from -70 °C freezer and left in 20 °C room temperature for 20 minutes before they were seeded in the micro bioreactor using 0.1-10 μ L micro pipette. The number of seeded yeast was around 80. The micro bioreactor was placed in the reaction chamber (1inch \times 0.5inch \times 0.5inch) filled with DPBS. Two steel micro tubes with OD 400 μ m penetrated the chamber side walls and were connected to the micro bioreactor inside as shown in Figure 4.2C. The chamber was covered with quarter inch thick transparent PLEX sheet to prevent possible contamination. The yeast culture medium YPD (1 g yeast extract (Difco), 2 g Peptone (Difco), 2 g D-glucose, 100 mL distilled water) was delivered at a flow rate of 0.5 mm/s through the capillaries in the

micro bioreactor. The culture chamber is kept in a humidified incubator at 30 °C for 45 hours. The DPBS solution in the chamber was replaced with fresh one every 6~10 hours to remove the ethanol in the chamber. The glucose concentration in the replaced DPBS was measured using GlucCell™ glucose monitoring system. Finally, the incubated micro bioreactor was removed from the chamber and dried in air at room temperature for one hour before sputtering coating and SEM observation.

4.5 CONCLUSIONS AND OUTLOOK

Projection micro-stereolithography promises rapid design and manufacturing of advanced micro bioreactors by offering a unique opportunity to culture tissues in vitro. By integrating high density micro capillary channels within the micro bioreactors, the mass transport can be enhanced by advection to withstand the increasing demand of oxygen and nutrients during cell growth. Simulation based on glucose diffusion model shown that the bottleneck of effective transport was the diffusivity of the polymer material of capillaries. The glucose concentration dramatically decreased after diffusing through the wall of the capillary. The *S. cerevisiae* yeast cell and the CHO cell cultures well verified the simulation prediction. Our simulation modeling can predict how far the nutrients transport into cell layers. With the predicted transport distance, we can precisely control the density of the polymer capillary to ensure that all the cells in the micro bioreactor are in healthy nutrient state.

Our future efforts to improve the application of our vascularized bioreactors include multi-layered cell co-culture, controlling the porosity of capillaries, and more complicated configuration of capillaries.

Research [10] has shown that a multi-culture system can promote the formation of endothelial blood vessel network in vitro and in vivo, and formed a thin tissue. Therefore, we hypothesize that a bio-degradable artificial capillary network, combined with a multi-culture system (Figure 4.11), can induce the vascularization in a thick artificial tissue.

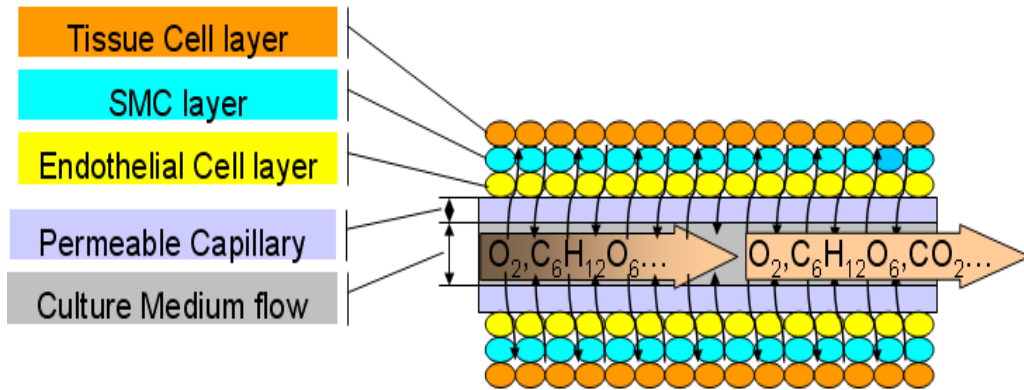


Figure 4.11. Schematics of constructing artificial tissue. SMC (smooth muscle cell).

We expect the polymeric walls of capillaries will eventually be dissolved by the flowing culture medium, resulting in a thick artificial tissue with natural endothelial vessels stabilized by smooth muscle cells. However, the road to success is full of challenges which include uniform cell seeding on the surfaces of capillaries and the secondary cell seeding on capillaries covered with endothelial cells and so on. These challenges lead to the need of a new technology capable of fixing cells to the desired locations on 3D scaffolds, during or after the fabrication of scaffolds. This kind of technology will contribute greatly to the field of 3D cell patterning which helps to understand cell-cell interactions, increase protein production and further boost the development of tissue engineering.

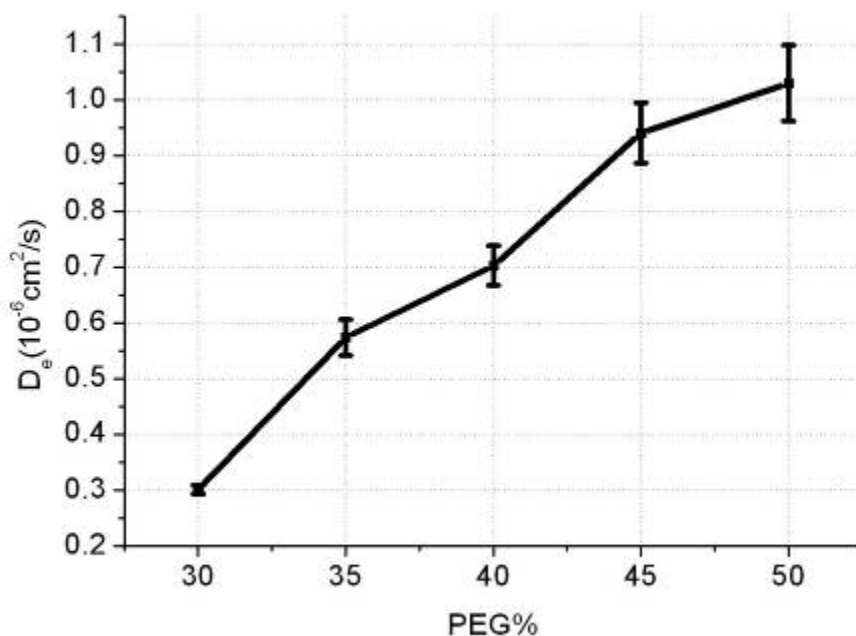


Figure 4.12 Effective diffusion coefficient of glucose in HDDA membranes fabricated using a mixture of HDDA and PEG at different ratios (weight percent).

In Figure 4.1 we have shown that the permeability of polymeric structures is a function of curing photon dose during the photo-polymerization process. However, the advantage of this method is shadowed by the tunability of this method. To extend the range of controllable permeability of polymeric structures, we introduced a method of photo-polymerizing a mixture of photo-curable monomer and photo-inert monomer, which are mixable but non-reactive with each other. For instance, we have achieved a wide range of effective diffusion coefficient of glucose in 200- μm thick membranes fabricated using a mixture of HDDA (SR238, Sartomer) and PEG (MW 250, Sigma-Aldrich) at different ratios (Figure 4.12). The change of permeability was due to the phase separation of HDDA and PEG during the photo-polymerization, which induced nano-pores in the structure after the non-reactive PEG was washed out (Figure 4.13). In a

range of 30wt % to 50 wt% of PEG, the pores size varies from 100 nm to 900 nm. This leads to an opportunity of filtering the size of molecules passing through the material. As an ongoing collaboration with Prof. Rohit Bhargava in the effort to construct an *in vitro* 3-dimensional prostate cancer model with controlled micro-structures, this method is currently under investigation.

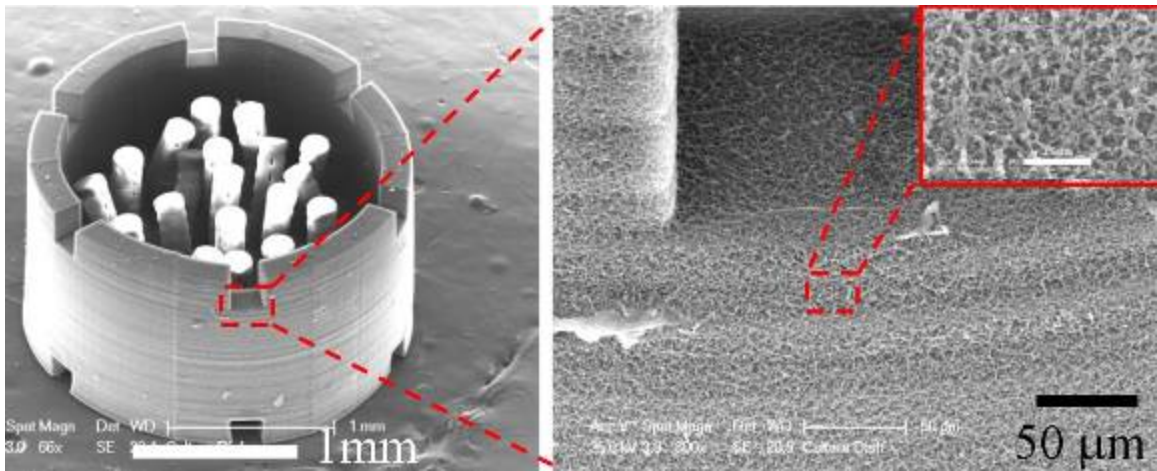


Figure 4.13 A micro structure fabricated in P μ SL using a mixture of 50 wt% of HDDA and 50 wt% of PEG (MW250).

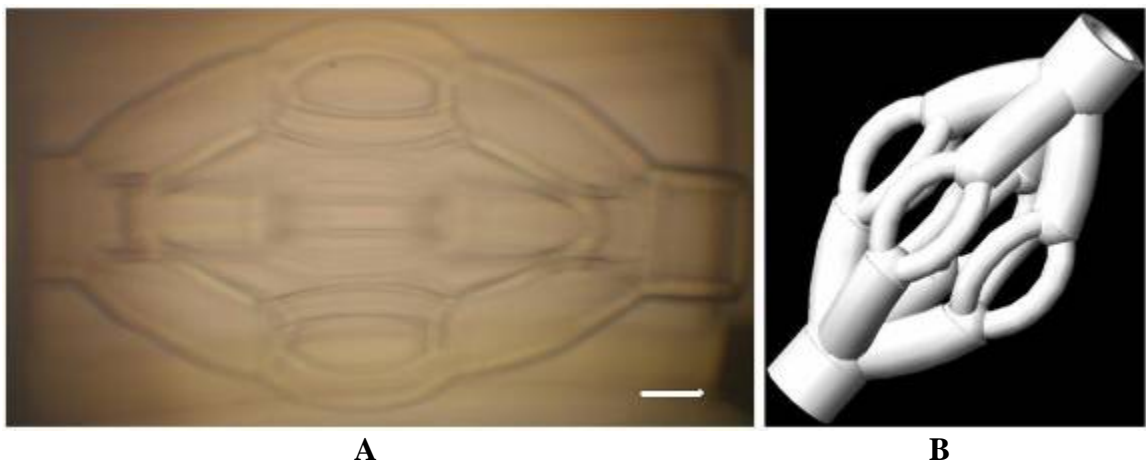


Figure 4.14 A. Optical image of a branching capillary system. B. CAD design of capillary system. Scale bar = 100 μ m.

Nature creates the blood capillary system with numerous bifurcating structures. This is the most effective structure to deliver nutrients to every single cell all over a human body. In order to take the advantage of this natural creation, it is essential to be able to mimic this structure in P μ SL for the bioreactor design. As one of our future efforts, we designed and fabricated a bioreactor with branching capillaries (Figure 4.14). Figure 4.14A was taken with the sample in ethanol and it clearly showed the inner connectivity of branching capillaries.

REFERENCES

- [1] Dunn R, Watson S. Why climb a ladder when you can take the elevator? *Plast Reconstr Surg*, 107, 283(2001)
- [2] Taylor GI, Palmer JH. The vascular territories (angiosomes) of the body: experimental study and clinical applications. *Br J Plast Surg*, 40,113-141 (1987)
- [3] Francois Berthiaume and Martin L. Yarmush, *Tissue Engineering, Encyclopedia of Physical Science and Technology*, 3rd edition, (Academic Press, 2002), 16, p817
- [4] Ruben Y. K, Henryk J. S, Kevin Sales, Peter Butler, Alexander M.S, The roles of tissue engineering and vascularisation in the development of micro-vascular networks: a review, *Biomaterials*, 26, 1857-1875(2005)
- [5] Sutherland, R.M. et al, Oxygenation and differentiation in multicellular spheroids of human colon carcinoma. *Cancer Res*. 46, 5320-5329 (1986).
- [6] Martin, I. et al, Method for quantitative analysis of glycosaminoglycan distribution in cultured natural and engineered cartilage. *Ann. Biomed. Eng.* 27, 656-662(1999).
- [7] Neumann T, Nicholson BS, Sanders JE., Tissue engineering of perfused microvessels. *Microvasc Res*, 66:59-67(2003)
- [8] Griffith LG, Wu B, Cima MJ, Powers MJ, Chaignaud B, Vacanti JP. In vitro organogenesis of liver tissue. *Ann NY Acad Sci*, 831:382-97(1997)
- [9] Jeffrey T. Borenstein, et al, Microfabrication Technology for Vascularized Tissue Engineering, *Biomedical Microdevices*, 4:3, 167-175(2002)
- [10] Shulamit Levenberg, Jeroen Rouwkema, Mara Macdonald, Evan S Garfein, Daniel S Kohane, Diane C Darland, Robert Marini, Clemens A Van Blitterswijk, Richard C Mulligan, Patricia A D Amore, and Robert Langer, Engineering vascularized skeletal muscle tissue, *Nature biotechnology*, 23, 879 - 884 (2005)
- [11] C. Sun, N. Fang, D.M. Wu, X. Zhang, Projection micro-stereolithography using digital micro-mirror dynamic mask, *Sensors and Actuators A*, 121,113-120(2005)
- [12] Buddy D. Ratner, Stephanie J. Bryant, *Biomaterials: Where We Have Been and Where We Are Going*, *Annu. Rev. Biomed. Eng.* 6:41-75(2004)
- [13] Qingpu Hou, Paul A. De Bank, Kevin M. Shakesheff, Injectable scaffolds for tissue regeneration, *J. Mater. Chem.*, 14: 1915-1923(2004)

- [14] E. Manias, J. Chen, N. Fang, X. Zhang, Polymeric Micromechanical Components with tunable Stiffness, *Appl Phys Lett*, 79, No 11, 1700-1702(2001)
- [15] N. Fang, C. Sun, X. Zhang, Diffusion-limited photopolymerization in scanning micro-stereolithography, *Appl. Phys. A*, 79:1839-1842(2004)
- [16] C.G. Xia, C. Sun, D.M. Wu, X. Zhang and Nicholas Fang, 3D Microfabricated Bioreactors, *NSTI-Nanotech*, 2, 140-143 (2006)
- [17] Leonor Michaelis, Maud Menten. Die Kinetik der Invertinwirkung, *Biochem. Z.*, 49:333-369(1913)
- [18] G. E. Briggs, J. B. S. Haldane, A note on the kinetics of enzyme action, *Biochem. J.*, 19:339(1925)
- [19] Fotios M. Andreopoulos, Eric J. Beckman, Alan J. Russell, Light-induced tailoring of PEG-hydrogel properties, *Biomaterials*. 19(1998) 1343-1352.
- [20] Karin Otterstedt et al, Switching the mode of metabolism in the yeast *Saccharomyces cerevisiae*, *EMBO reports*, 5, No. 5:532-537(2004)
- [21] T.G. Kaufmann and E.F. Leonard, Mechanism of interfacial mass transfer in membrane transport. *AIChE J.* 14, 421(1968)
- [22] Fred Sherman and James Hicks, Getting started with yeast, *Methods in Enzymology* 194:3-21,(1991)
- [23] Antonio A. Vicente, Marian Dluhy, Eugenio C. Ferreira, Manuel Mota, Jose A. Teixeira, Mass transfer properties of glucose and O₂ in *Saccharomyces cerevisiae* flocs, *Biochemical Engineering Journal*, 2:35-43(1998)
- [24] Verduyn C, Zomerdijk TPL, Van Dijken JP, Scheffers WA, Continuous measurement of ethanol production by aerobic yeast suspension with and enzyme electrode, *Appl Microbiol Biotechnol* 19:181-185(1984)

CHAPTER 5

SOLVENT-DRIVEN POLYMERIC BEAM DEVICES

5.1 INTRODUCTION

Many applications of hydrogels depend on their unique solvent-swollen properties. Their swelling and shrinking behaviors can be triggered by different stimuli, such as by solvents with different ion concentrations[1], temperature[2], and radiation[3]. The solvent-stimulated swelling phenomenon in hydrogels has long been recognized and investigated theoretically and experimentally [4~6]. The unique characteristics of these polymers have led to some interesting micro devices and applications [7~13]. However, due to fabrication challenges, these gel devices are often formed into simple geometries such as spheres and strips. Moreover, they can only operate in solvents. The response speed is also a great concern for hydrogel devices. It is well known that solvent transport in gels is diffusion dominated. As a general estimation, the diffusion time scale is L^2/D ; here, L is the characteristic length and D is the diffusion coefficient of the solvent. The diffusion coefficient of a solvent in polymer gel is usually in the range of $10^{-6} \sim 10^{-10}$ cm^2/s . Therefore, for length scales on the order of $100\mu\text{m}$, the diffusion time is larger than 100 s or 1.7 minutes. The slow pace of the diffusion process is responsible for the slow responses of hydrogels and further limits the application of polymer swelling in microfluidic devices and other applications, like artificial muscles.

To overcome the diffusion speed limit, we for the first time introduced a micro capillary network into a hydrogel device [14]. The capillaries serve as “highways” for long-range solvent transport by capillary force. In this case, diffusion transport only

happens locally (short range) across the capillary walls. Compared to diffusion, capillary flow is much faster. The velocity of the solvent front in a capillary can be estimated by $T_s \cos(\theta) R / (4\eta L)$ [15], where T_s and η are the surface tension and the viscosity of the solvent, respectively, θ is the contact angle, R is the radius of the capillary, and L is the length of the solvent in the capillary. For water, $T_s=72$ mN/m, $\eta=8e-4$ Pa·s, a typical contact angle is $\theta=30^\circ$, and the water front velocity can reach 2 m/s for a 1-mm long water column in a 200- μ m micro channel. Although the solvent front velocity may differ from solvent to solvent, it is clear that, generally, capillary flow is much faster than the diffusion process by several orders of magnitude. Therefore, capillary networks dramatically increase the speed of long-range solvent transport and of the gel response. Nevertheless, the gel response is still dominated by local diffusion. The speed of local solvent transport cannot be increased without applying external driving forces, such as pressure, which increase the operation cost of the gel devices.

As a cheap and effective means to overcome these limitations, we introduce an elastic instability mechanism into polymer gel devices. In this way, the elastic energy during the slow gel swelling or shrinking process is stored in the device and afterwards is quickly released by taking advantage of the elastic instability. As a demonstration, in this chapter we focus on micro gel beam structures. Incorporation of bistability in silicon micro-electro-mechanical systems (MEMSs) is not a new idea. The simplest mechanical bistable system can be developed by applying an axial compressive force at both ends of a slim beam. If the force exceeds a certain value, the beam buckles into one of two possible stable states [16]. A more general bistable system may incorporate additional transverse forces with different configurations [17-19], thermally-introduced compressive

force [20] or use the electro-thermal bimorph effect [21]. However, little attention has been given to polymer gel devices, to the best of our knowledge. Polymeric devices have great potential in the development of artificial muscles and as transducers for micro-fluidic circuits. In such applications, the available trigger signals are usually solvents or the desired ion concentration; therefore, external transverse force, as often used in silicon based beams, is not preferred for triggering the instability mechanism, nor is the thermal expansion effect. As a solution, we propose the use of locally-controlled gel swelling and shrinking to trigger instability. In this case, the only input is the solvent from micro-fluidic circuits and the device can be actuated off-plane. In the following sections, a brief introduction on solvent diffusion in polymers and on elastic beam instability will be given before the details of the fabrication, design criteria and performance of a polymeric bistable device.

5.2 SOLVENT DIFFUSION IN POLYMERS

5.2.1 Literature review

Our design here heavily involves the phenomenon of solvent diffusion in polymers, understanding which will provide the insight criteria for the design of our polymer micro devices. However solvent diffusion in polymers is very complex and often shows different kinetics [22]. So far there is no single theoretical framework or mathematical model has been able to provide a complete explanation of this phenomenon [23-25]. The challenges come from the dramatic variety of the physical and chemical properties of the polymeric materials and the nature of solvents. The solvent diffusion in polymers can be separated into three steps. Small solvent molecules are first absorbed on the surfaces of the polymeric material. Then the molecules diffuse through the polymer and finally

desorb on the surfaces of the polymer. The duration and intensity of these steps is influenced by several factors such as the polymer and solvent molecular structures, temperature, mechanical deformation, solvent-polymer interaction, etc. [23, 26]. Many of these factors affect the mass transport process through a substantial time scale associated with structural changes of the polymer, for example, during plasticization the polymer changes from a glassy to a rubbery state when the local solvent volume fraction exceeds some threshold values. If the time scale of the swelling experiment is much longer or shorter than the time scale for molecular rearrangement of the polymer network, then the evolution of the system can be modeled as a Fickian diffusion process. On the other hand, if swelling is measured on a time scale that is of the same order as that for molecular rearrangements, diffusion will often be non-Fickian [27]. Furthermore, when diffusion occurs in the rubbery state, large segments of the polymer participate due to chain rotations, translations as well as vibrations such that a larger internal void space is more readily accessible. However, in the glassy state, chain motion is limited in hard or brittle polymers. There is less free volume than in the case of rubbery polymers. It has also been shown that polymeric materials at a temperature below the glass transition temperature may be in a state of non-equilibrium, with properties generally characterized as being time dependent. As a result, the diffusion of small molecules through glassy polymers becomes rather complex.

Several models have been proposed to explain the phenomenon of solvent diffusion in polymers. Models based on Fick's laws are often adopted due to its simplicity and mathematical tractability. Fick's first law (Equation (5.1)) says that the mass flux (J) through an area is proportional to the concentration (c) gradient normal to the area and

the linear coefficient is given the name of diffusion coefficient (D) which can be concentration dependent. The commonly adopted concentration dependency of D is derived from free volume theory which suggests that the D is exponentially related to the local concentration. Fick's second law (Equation (5.2)) truly is a law of mass

$$J = -D\nabla c \quad (5.1)$$

$$\frac{dc}{dt} = -\nabla \cdot J \quad (5.2)$$

conservation which mathematically tells that the concentration rate at a space point is equal to the divergence of the local mass flux. Despite the thorough development of Fickian diffusion theories [28-33], most of the solvent-polymer systems do not obey this simplified explanation, especially in the case of glassy polymers in which often a clear sharp diffusion front is observed. The sharp front separates the dry polymer from the swollen polymer, usually associating with a phase change from glassy state to rubbery state. The movement of the sharp front is associated with the nature of a solvent-polymer system and it can be mathematically categorized in term of the mass uptake M.

$$M = kt^n \quad (5.3)$$

here t is the time and k and n are constants. Then Fickian diffusion (Case I diffusion) follows $n=1/2$, Case II diffusion corresponds to $n=1$ [34], and anomalous diffusion is characterized by: $1/2 < n < 1$. The Case II diffusion has attracted a lot of attention due to its unique characteristics: (1) a sharp diffusion front separates the wet and swollen region from a dry and usually glassy region; (2) the solvent volume fraction is almost uniform behind this front; (3) the front moves at a constant speed; (4) usually a Fickian precursor appears in the dry region right ahead of the front. To understand the non-Fickian diffusion, Thomas and Windle suggested that the diffusion process was strong coupled

with the mechanical response (viscoelastic response) of the polymer [35-37]. The sorption of solvent creates the osmotic pressure which induces the swelling. The osmotic pressure and the viscoelastic response together affect the deformation of the polymer such that mechanical response and Fickian diffusion are coupled. Unfortunately, this model did not take external loads into account which led to the consideration that the transport of the penetrants to be driven by both molecular diffusion and by a stress associated with swelling [38, 39]. This idea was implemented by introducing extra mass flux associated with the stress gradient. Different kinds of viscoelastic models were also adopted to derive the stresses. However these models leave out the interactions between the solvent and polymer, causing the need to fit models to different solvent and polymer systems and these theories fail to predict the coupled large deformation of polymer which obviously happens in our work.

Apart from the theories dedicated to the transport of small molecules in dry polymers, field theories have been formulated to unfold the transport of liquid in hydrogels and porous materials. Especially, porous elastic models have been successfully introduced to explain the liquid transport in porous elastic solids [40, 41]. Many more theories based on different concepts also contributed to the understanding of the swelling and shrinking of polymeric gels [42-46]. All these field theories well explain the liquid transport in wet gels to certain extend, however, the fully explanation of liquid transport in dry polymers coupled with large deformation remains a challenge.

Substantial progress in both experiment and theory has been achieved to better under the transport of small molecules through polymers. However, more delicate field model is desired to fully understand this phenomenon. Therefore, in this work, we will present the

data of diffusion experiments to get a qualitative image of solvents diffusion in the polymer we used, leaving the modeling as one of the future efforts.

5.2.2 Solvent diffusion in photo cross-linked poly ethylene glycol (PEG)

The polymer we used in the work was PEG diacrylate (MW575, Sigma-Aldrich), Bis(2,4,6-trimethylbenzoyl)-phenylphosphineoxide (Irgacure 819, from Ciba) was used as the photo initiator. We mixed 0.75 wt% of UV absorber with the PEG monomer to control the UV penetration depth in the solution. The wave length for the light source was 436 nm and the light intensity was 3.32 mW/cm². The solvent-polymer systems we studied were acetone-PEG, ethanol-PEG, and water-PEG. It is worth to mention that the method we propose here is not limit to PEG only. The two basic criteria for the material selection are: (1) the material must be able to swell or shrink as it contacts with or separates from solvents; (2) the material must be compatible with P μ SL.

It has been known that the propagation of solvent diffusion front in polymers is associated with the intrinsic nature of the diffusion [47], for example, if t is the time, then the diffusion front position in the Fickian diffusion (Case I diffusion) is proportional to $t^{1/2}$ instead of t which is unique for Case II diffusion. Therefore by tracking the diffusion front, one can tell the category of the observed diffusion. Fortunately, the photo cross-linked PEG is transparent for visible light. Therefore the diffusion front propagation can be tracked by monitoring the light reflection from the front. The detectable reflection change at the diffusion front is the result from the shift of the optical properties of the polymer while soaked with solvents.

Two kinds of sample were prepared for the diffusion study. One was fabricated from 100% PEG diacrylate solution. We designed the sample as shown in Figure 5.1. This

sample has a $200\ \mu\text{m} \times 200\ \mu\text{m}$ channel parallelly next to an $800\ \mu\text{m} \times 800\ \mu\text{m} \times 500\ \mu\text{m}$ diffusion block of PEG. A micro tube with inner diameter of $200\ \mu\text{m}$ is inner-connected with the channel as the inlet. Solvents will be continuously delivered through the micro

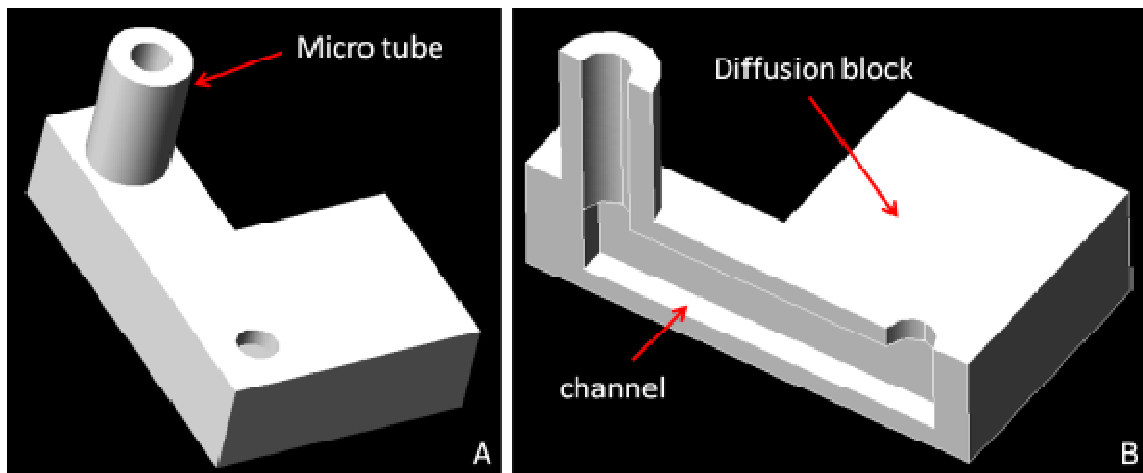


Figure 5.1 A. The CAD model of the device for diffusion study; B. The section view of the device in A.

tube while the capillary force drags the solvents into and fills the channel. The sample was fabricated using P μ SL and then soaked in acetone for 3 hours before it was dried in air at room temperature for 1 hour. The diffusion started to happen at the moment the channel was filled which happens so fast ($<0.1\ \text{s}$) that we could assume that the edge of the polymer block contacts with the solvent at the same time. A video was recorded from the top of the diffusion block as the front propagated into the polymer block (Figure 5.2). It can be seen that a sharp front blurs as it penetrates into the polymer. The penetration depth was calculated by measuring the distance between the front and a fixed point ahead of the front. Three solvents were studied, acetone, ethanol, and water (Figure 5.3). From

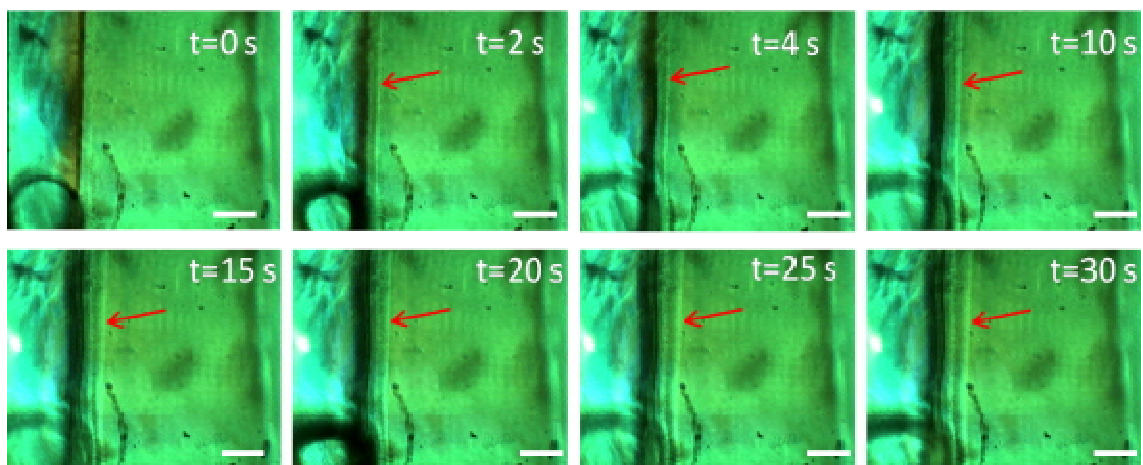


Figure 5.2 Video frames of acetone diffusion in a PEG block. Scale bars are 100 μm and the arrows indicate the front position.

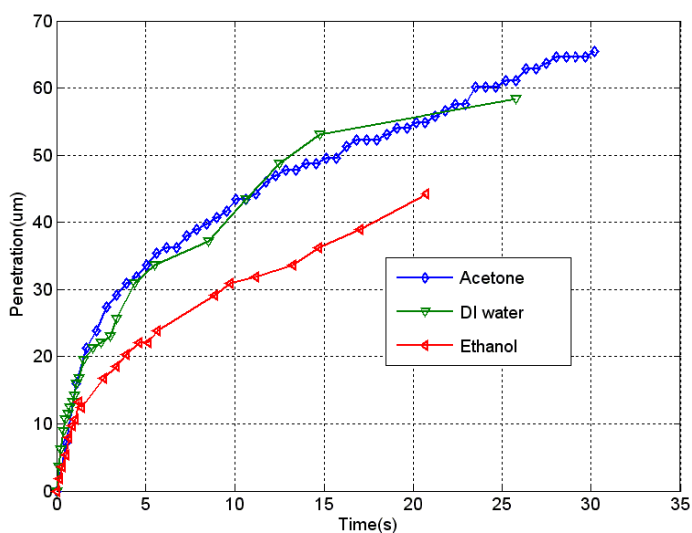


Figure 5.3 The propagation of solvent diffusion front in PEG

these curves, it seems that none of it follows the Case II diffusion which is characterized by a sharp and linear front propagation. Neither are they Fickian diffusions, because the front position does not follow the $t^{1/2}$ relationship. Acetone and water have a similar behavior, with ethanol showing slower diffusion. Close study of the experiment data appears to tell that this anomalous diffusion has a linear front propagation at the first 20

μm follow which is a Fickian diffusion. This phenomenon is consistent with the observation that the front was sharp at the beginning and then turned into a blurry one. One possible explanation is that when the diffusion front is close to the surface, the pressure at the front takes less effort to move solvent from the surface to the sharp front, but as the front moves further into the polymer, the resistant (depend on path length) to move the solvent to the front also increases while the driven pressure does not increase, as a result the sharp front blurs.

The mechanical deformation of the polymer during the solvent transport can affect the diffusion behavior. Therefore, as one effort of the fundamental study on solvent transport in polymers, we try to reduce the effect of the deformation and at the same time enhance the diffusion front visibility by designing the second sample to be a polymer rod with 600- μm diameter fabricated using a mixture of PEG diacrylate and PEG (MW=200, Sigma-Aldrich) at a weight ratio of 1:3, respectively. One end of the slim rod will contact with the solvent which starts to transport along the rod towards the other end. To make the polymer rod, a glass tube with 1-mm inner diameter was filled with the PEG mixture and then was exposed to a UV flux at wave length=390 nm, intensity =1.1 mW/cm² for 30 seconds. The solidified rod with diameter of 1 mm then was separated from the glass tube and left in acetone. Only the PEG diacrylate monomers were photo-crosslinked while the PEG in the solution led to the phase separation in the crosslinked polymer and dramatically increased its porosity after the PEG was removed by soaking the sample with acetone overnight. Finally the sample was dry in air for one hour before diffusion experiments at which moment the diameter of the rod had reduced to 600 μm . The dry sample was transparent and the swollen sample showed in white color, which made it

easier to track the diffusion front comparing to samples of PEG diacrylate only. The experiment was carried out at a room temperature of 20 °C in a sealed glass tube with half inch inner diameter (Figure 5.4). The solvent used in this experiment was deionized water. Therefore, to reduce the effect of the evaporation at the surface of the rod, the glass tube was partially filled with deionized water to saturate the water vapor in the glass tube. The polymer rod was hanged from the tope and a metal tube extruded form the bottom to deliver the water to the lower end of the rod. The diffusion progress was recorded (Figure 5.5) and the data is shown in Figure 5.6. It can be clearly seen that there is a sharp front separating the dry (glassy) region and the wet (rubbery) region. The transport followed Fickian diffusion at the beginning and then developed into a Case II diffusion with constant swelling ratio.

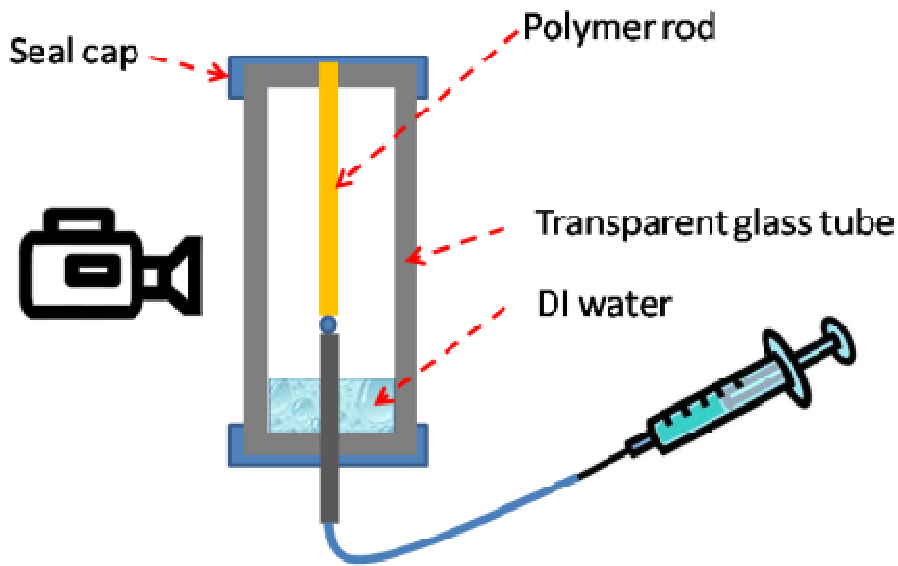


Figure 5.4 Schematic drawing of the setup for measuring water diffusion in a polymer rod.

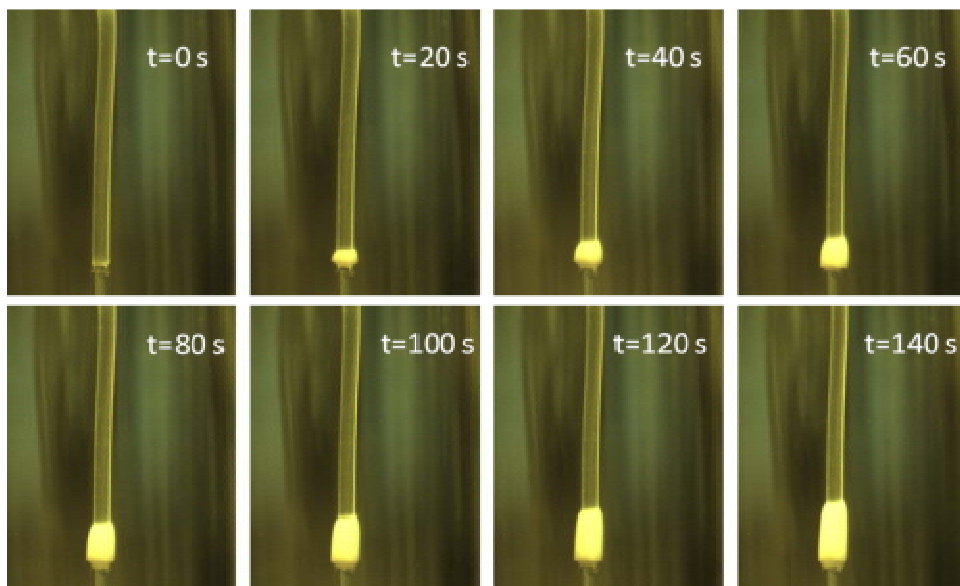


Figure 5.5 The time frames of water diffusion in a PEG rod. The diameter of the dry rod is $600\ \mu\text{m}$.

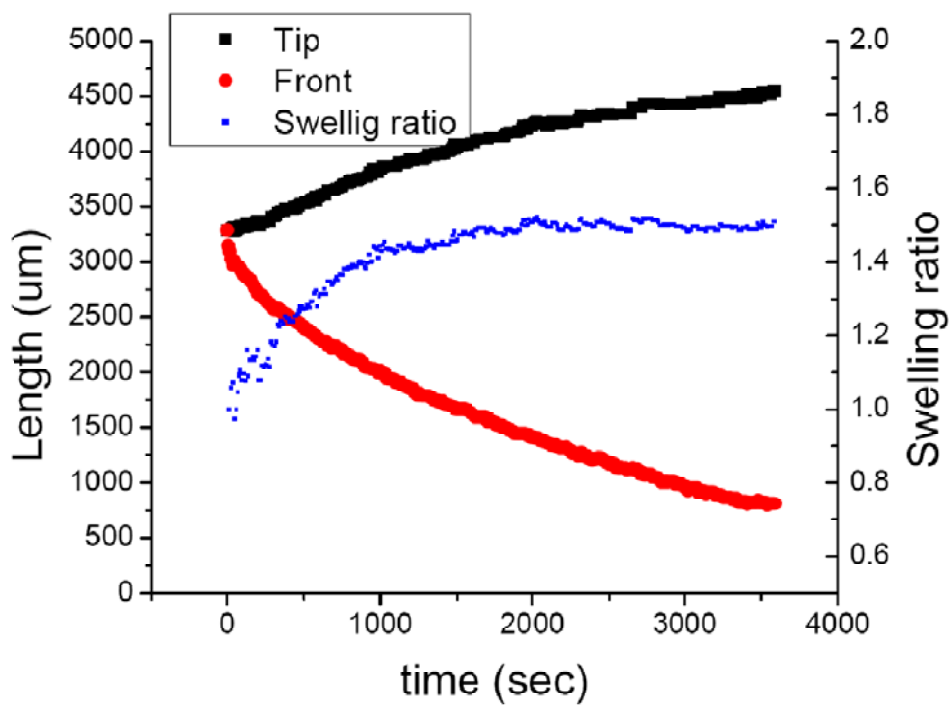


Figure 5.6 Front and tip position in PEG rod diffusion with the calculated swelling ratio. The swelling ratio is defined as the length of wet region divided by the length of original dry region corresponding to the wet region.

5.2 POLYMER ACTUATOR BY SURFACE CAPILLARY

Cantilever is one of the most important actuation structures. Therefore we introduce cantilever as an example for the application of capillary network in polymer swelling control. Though Guan [48] has designed a 2D bi-layered polymer cantilever structures using different polymers for each layer and the structures can fold up in solvents, our 3D cantilever device not only can be actuated in air but also the whole cantilever beam is made of a single polymer. When one surface of a PEG cantilever contacts the solvent, the polymer starts to swell. However, wetting of the whole curved beam takes longer time than the time scale of desired experiments, thus the solvent only wets a portion of the curved beam (Figure 5.7). As a result, for a relatively long time, the beam is roughly divided into two layers: a wet layer and a dry layer. The wet layer swells and expands, while the dry layer is stretched. This is similar to the thermal bimorph effect, which also has two layers but with distinct materials for each layer. The strong shear stress causes a change of the beam curvature. Conversely, when the solvent evaporates, the wet part will begin to shrink and reverse the curvature towards its initial shape. In order to distribute the solvent to one surface of the cantilever for actuation and deplete the solvent for de-actuation, we propose to introduce the capillary into the cantilever which requires a sophisticated micro fabrication technology. There are several micro fabrication techniques for soft materials [49]. As a cheap and fast method for polymer gel fabrication, photo-polymerization is the most attractive. However, in order to construct a complicated 3D micro structure, advanced technologies and methodologies need to be incorporated to

guide photo-polymerization in 3D space. Therefore we adopt projection micro-stereolithography (PμSL) as our design tool.

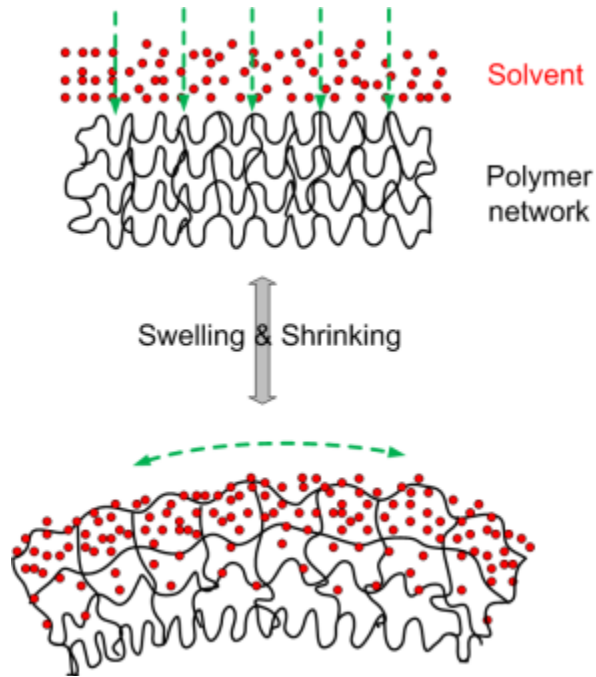


Figure 5.7 Schematic illustration of solvent diffusion introducing the curvature change of a polymer cantilever.

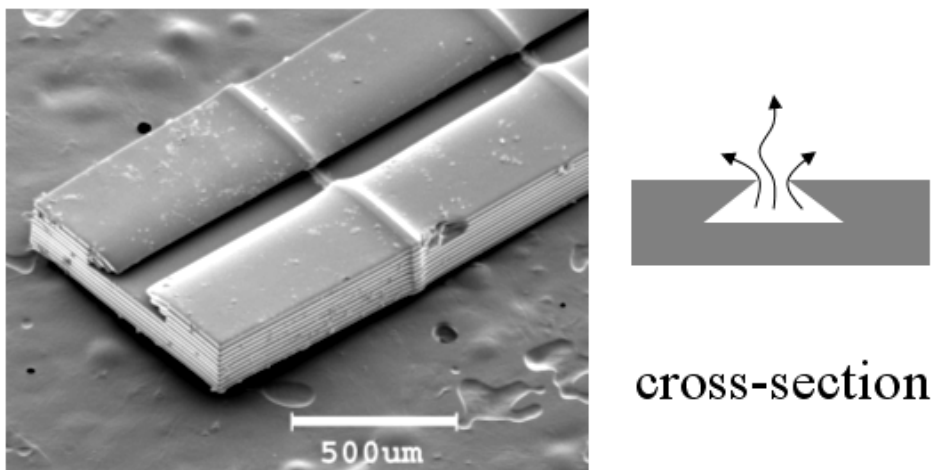


Figure 5.8 PEG cantilever with surface capillary

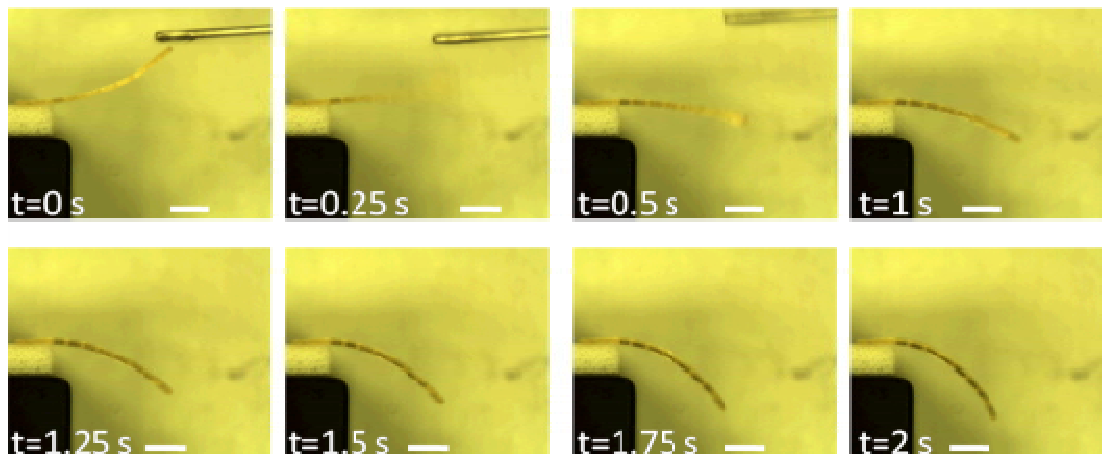


Figure 5.9 Time frames of a PEG capillary actuated by a drop of acetone. Scale bars are 2 mm.

We designed a cantilever beam with embedded open surface capillary as shown in Figure 5.8. The wedge-shaped cross-section of the cantilever not only helps to increase the capillary force by changing the contact angle but also keeps the solvent from drying out before reaching the destination thus reduce the amount of solvent for actuation. A 1-cm long, 1-mm wide, and 400- μm thick cantilever was fabricated and tested (Figure 5.9). In the test, one end of the cantilever was glued to a fixed support and a droplet of acetone was delivered to the other end using a needle. The test was conducted at a room temperature of 20 °C. Since the solvent was almost uniformly distributed along the cantilever, the cantilever bended into an arc. The curvature changed faster first then slowed down. This was due to the higher acetone transport speed at the beginning and the depletion of the acetone in the capillary later. As one of the advantages of polymeric beam actuators over conventional silicon-based beam actuators, the polymeric ones are capable of providing much larger actuation displacement with respect to the dimension of

the beam. For example, the displacement of the tip of the cantilever in Figure 5.9 can be larger than the length of the cantilever.

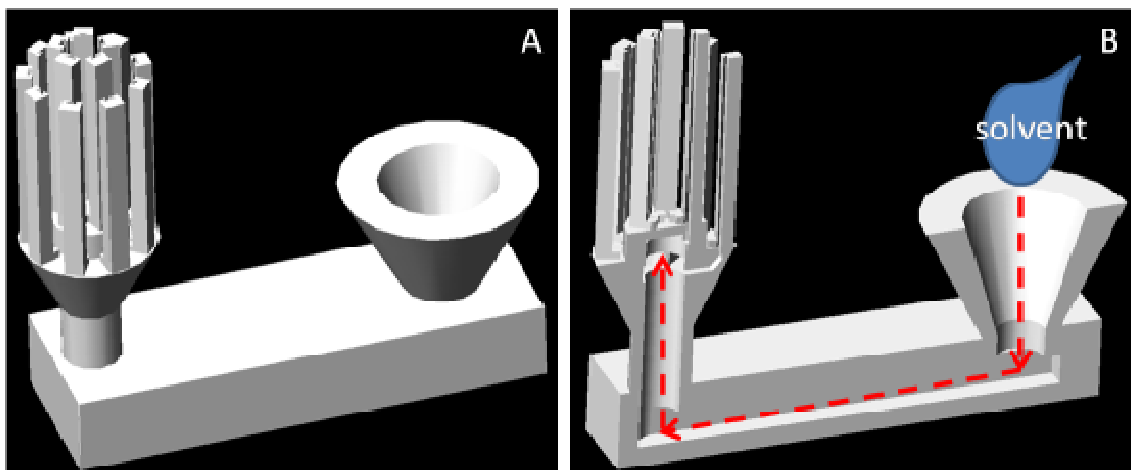


Figure 5.10 A. CAD model of a polymeric micro flower with 14 leaves. B. Section view of the micro flower in A, the red arrows indicate the direction of the solvent flow. The length of the cuboid base is 2-mm long.

As a demonstration of polymer actuation in a complex micro fluidic system, we also designed a polymeric micro flower with 14 leaves (Figure 5.10). These leaves have the same shape as shown in Figure 5.8 and with dimensions $1000\ \mu\text{m} \times 100\ \mu\text{m} \times 80\ \mu\text{m}$. The surface capillaries associated with these leaves are about $40\text{-}\mu\text{m}$ deep and $60\text{-}\mu\text{m}$ wide. All leaves are connected to a funnel through internal capillary network (Figure 5.10 B). When a drop of acetone is placed in the funnel, the capillary force will drive them to all the cantilevers and they will bend simultaneously. Conversely, as the acetone evaporates, all cantilevers will recover to original shape simultaneously (Figure 5.11). This device also shows the possibility of synchronized control of multiple micro fluidic actuators by the design of 3D micro fluidic channel network in P μ SL.

From the time scale of the above two devices, it shows that the actuation mostly happens in the first one second. On one hand, this actuation speed is much faster that

most of the existing hydrogel actuators which often take tens of seconds or even longer to response. On the other hand, it suggests that Fickian diffusion may be valid to model this phenomenon since Fickian diffusion is the dominant mechanism at the beginning of most of the solvent-polymer diffusions. Further study is needed to validate this argument.

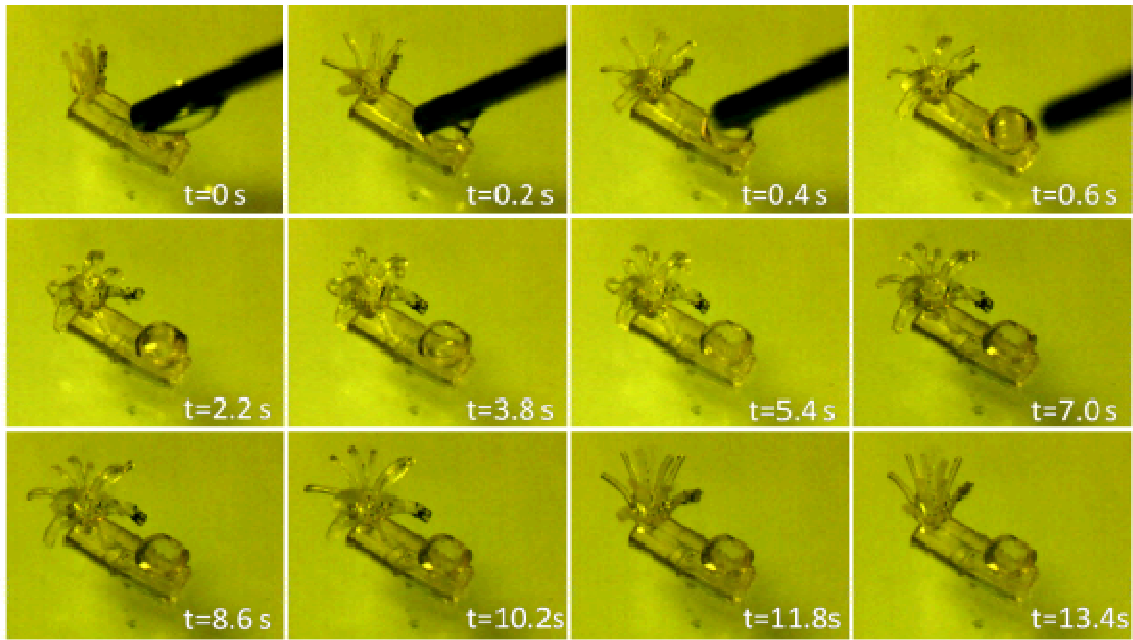


Figure 5.11 Time frames of a micro flower actuated by a drop of acetone.

5.3 BISTABLE POLYMERIC BEAM DEVICE

To further increase the response speed of the polymeric actuator, we introduce the elastic instability into a polymeric beam device. In this section, we will first briefly introduce the linear elastic theory of bending and derive the equations to describe the instability of a curved beam, then we will implement this analysis to a bistable beam device, and finally we will show the performance of this device.

5.3.1 Introduction to linear elastic theory of bending

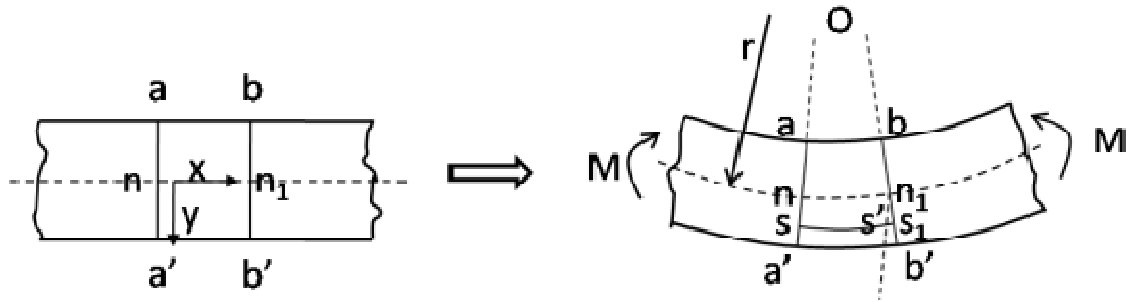


Figure 5.12 A prismatical bar undergoes pure bending

We start from a pure bending case: A prismatical bar under the action of equal and opposite couples at its ends is said to undergo pure bending. The magnitude of the couple is M which is called the bending moment (Figure 5.12). It has been experimentally proved that we can assume the entire transverse section, such as $a-a'$ and $b-b'$ which are originally plane, remains plane and normal to the longitudinal axis ($n-n_1$) of the bar after bending. The axis of the bar refers to the line through the centroids of its cross sections. Based on this assumption, during bending the cross sections $a-a'$ and $b-b'$ rotate with respect to each other about axes perpendicular to the plane of bending, so that the material on the concave side surface compression and that on the convex side extension. The surface through $n-n_1$ and perpendicular to the plane of bending does not experience any strain, which is called the neutral surface and its intersection with any cross section is called the neutral axis. The distribution of the strain on any cross section can be derive by considering a plane ($s-s'$) which is at distance of y from the neutral surface. The elongation of $s-s'$ can be obtained by drawing a line n_1-s' parallel to $a-a'$. Denoting by r the radius of curvature of the deflected axis of the bar and using the similarity of the triangles $s's_1n_1$ and nn_1O , the strain associated with surface ss' is

$$e_x = \frac{s's_1}{ss'} = \frac{s's_1}{nn_1} = \frac{y}{r} \quad (5.4)$$

This equation also applies to the concave area with $y < 0$ thus $e_x < 0$ which means material is under compression. From equation (5.4) it tells that the strains in the cross sections are proportional to the distance y from the neutral surface and inversely proportional to the radius of the curvature. The maximum strain appears at the surface of the bar which is farthest from the neutral surface. Now the equilibrium condition requires the strain (or stress) distribution must give rise to a resisting couple which balances the external couple M . Let dA be the elementary area of a cross section, according to Hooke's law, the moment of the force on this element with respect to the neutral axis is $(Ey/r) \cdot dA \cdot y$. $= (Ey^2/r) \cdot dA$, here E is the Young's module. Summarizing such moments over the entire cross section and putting the resultant equal to the external moment M , the following equation is obtained:

$$\int \frac{E}{r} y^2 dA = \frac{EI_z}{r} = M \quad \text{or} \quad \frac{1}{r} = \frac{M}{EI_z} \quad (5.5)$$

in which

$$I_z = \int y^2 dA \quad (5.6)$$

is the moment of inertia of the cross section with respect to the neutral axis z which is perpendicular the plane of bending. Equation (5.5) indicates the curvature varies directly with the bending moment and inversely with the flexural rigidity of the bar, EI_z .

For consistency, from now on let us use y to denote the deflection of the axis of the bar, then the well-known exact formula for the curvature is:

$$\frac{1}{r} = \frac{d^2y}{dx^2} / \left[1 + \left(\frac{dy}{dx} \right)^2 \right]^{3/2} \quad (5.7)$$

For small deflected bar, $(dy/dx)^2$ is small comparing with 1, therefore we can simplified Equation (5.7) by dropping term $(dy/dx)^2$ in the dominator as:

$$\frac{1}{r} = \frac{d^2y}{d^2x} \quad (5.8)$$

Combining Equations (5.5) and (5.8), we have:

$$\frac{d^2y}{d^2x} = -\frac{M}{EI_z} \quad (5.9)$$

The minus sign appears because the bending moment is taken positive when it produces upward concavity and the second derivative $(dy/dx)^2$ is negative for such bending if the coordinate axes are directed as in Figure 5.12. Equation (5.9) has general application in bending problems.

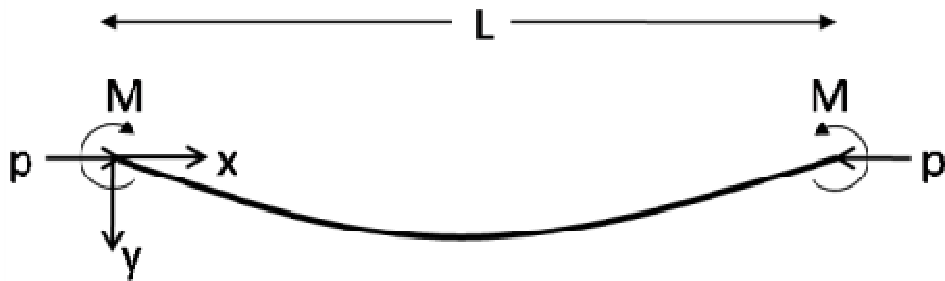


Figure 5.13. An initially curved bar under external bending moment and axial compressive loads.

The polymeric beams we design in this chapter are initially curved, and their curvatures change as the solvent transports into the polymer. Therefore one of the interesting problems for us is shown in Figure 5.13, an initially curved bar is under both the external bending moment and compressive loads at its ends. Let us consider, as an example, the case in which the initial shape of the axis of the bar is given by the equation

$$y_0 = a_n \sin\left(\frac{\pi x}{L}\right) \quad (5.10)$$

If this initially curved bar is submitted a longitudinal compressive force p and the bending moment M , additional deflections y_1 will be produced so that the final ordinates of the deflected curve are

$$y = y_0 + y_1 \quad (5.11)$$

and the bending moment at any cross section is

$$M' = M + p(y_0 + y_1) \quad (5.12)$$

Then the deflections y_1 due to the deformation are determined from Equation (5.9)

$$\frac{d^2 y_1}{d^2 x} = -\frac{M}{EI} - k^2(y_0 + y_1) \quad (5.13)$$

here $k^2 = p/(EI)$, and from now on we use I represent I_z . by substituting y_0 and rearrangement, we obtain

$$\frac{d^2 y_1}{d^2 x} + k^2 y_1 = -\frac{M}{EI} - k^2 a_n \sin\left(\frac{\pi x}{L}\right) \quad (5.14)$$

A guessed special solution for Equation (5.14), with A and B to be determined, may have form

$$y_s = AM + B \sin\left(\frac{\pi x}{L}\right) \quad (5.15)$$

which is substituted into Equation (5.14) and we have

$$\begin{aligned} & -B \frac{\pi^2}{L^2} \sin\left(\frac{\pi x}{L}\right) + Ak^2 M + Bk^2 \sin\left(\frac{\pi x}{L}\right) \\ & = -\frac{M}{EI} - k^2 a_n \sin\left(\frac{\pi x}{L}\right) \end{aligned} \quad (5.16)$$

By comparing the coefficients of M and \sin function, it gives

$$A = -\frac{1}{p}, \text{ and } B = \frac{\alpha a_n}{1-\alpha} \text{ with } \alpha = k^2 L^2 / \pi^2$$

Therefore the general solution for Equation (5.14) will be in form

$$y_1 = C \sin(kx) + D \cos(kx) + y_s$$

$$= C\sin(kx) + D\cos(kx) - \frac{M}{p} + \frac{\alpha a_n}{1-\alpha} \sin\left(\frac{\pi x}{L}\right) \quad (5.17)$$

and thus from Equation (5.11), we have

$$\begin{aligned} y &= a_n \sin\left(\frac{\pi x}{L}\right) + C\sin(kx) + D\cos(kx) - \frac{M}{p} + \frac{\alpha a_n}{1-\alpha} \sin\left(\frac{\pi x}{L}\right) \\ &= C\sin(kx) + D\cos(kx) - \frac{M}{p} + \frac{a_n}{1-\alpha} \sin\left(\frac{\pi x}{L}\right) \end{aligned} \quad (5.18)$$

here C, and D are coefficients are determined by applying the boundary conditions

$y=0$ at $x=0$ and $y=0$ at $x=L$ which tell $C = \frac{M}{P} \frac{1-\cos(kL)}{\sin(kL)}$, and $D = \frac{M}{P}$. Finally the solution

for Equation (5.14) is given by

$$\begin{aligned} y &= \frac{M}{P} \frac{1-\cos(kL)}{\sin(kL)} \sin(kx) + \frac{M}{P} \cos(kx) - \frac{M}{p} + \frac{a_n}{1-\alpha} \sin\left(\frac{\pi x}{L}\right) \\ &= \frac{M}{p \cos\left(\frac{kL}{2}\right)} \left[\cos\left(\frac{kL}{2} - kx\right) - \cos\left(\frac{kL}{2}\right) \right] + \frac{a_n}{1-\alpha} \sin\left(\frac{\pi x}{L}\right) \end{aligned} \quad (5.19)$$

Then the mid-point deflection can be obtained by setting $x=L/2$

$$y_{x=L/2} = \frac{M}{p \cos\left(\frac{kL}{2}\right)} \left[1 - \cos\left(\frac{kL}{2}\right) \right] + \frac{a_n}{1-\alpha} \quad (5.20)$$

When $M=0$ then Equation (5.19) reduces to a much simpler form

$$a_a = \frac{a_n}{1-\alpha} \quad (5.21)$$

This equation shows that the initial deflection a_n at the middle of the bar is magnified in the ratio $1/(1-\alpha)$ by the action of the longitudinal compressive force.

5.3.2 Bistable polymeric beam with elastic support

Euler's column theory tells that as a compressive force acting at the ends of a straight bar exceeds a critical value it will become unstable and buckle. Therefore when a curved beam is subjected to an elastic support and at the same changes its curvature, the force resulting from the elastic response of the support may exceed this critical value and cause

the beam to change curvature abruptly. This mechanism can be integrated into our solvent actuated polymeric beams to dramatically improve the response speed thus increase the transient mechanical power output. In this section we will show how to design the polymeric beam system with elastic instability response.

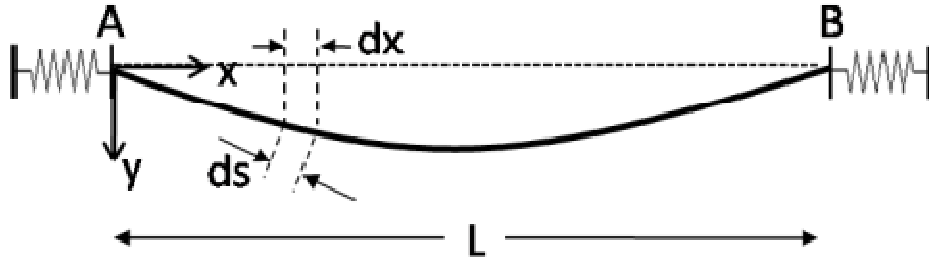


Figure 5.14 An initially curved beam with elastic supports.

Let us, for example, consider a simple case in which the interaction between the beam and the support is only a longitudinal force p , no bending moment M exists (Figure 5.14). Again the beam has initial sinusoidal shape as shown in Equation (5.10). This initial shape changes as the solvent starts to diffuse into the wall of the capillary which is embedded in the beam and we further assume that the beam keeps the sinusoidal shape (dominant shape, only the magnitude a_n changes) during this process. The initial shape is the shape without any external load and it changes during experiment. To be more precise, from now on we will denote the initial shape as natural shape and the associated deflection as natural deflection. Similarly, the shape under external forces will be denoted as actual shape and the associated deflection as actual deflection. Therefore the actual shape of the beam under force p is obtained from Equation (5.19) by taking $M=0$ as

$$y = \frac{a_n}{1-\alpha} \sin\left(\frac{\pi x}{L}\right) \quad (5.22)$$

and the actual mid-point deflection is shown in Equation (5.21). The linear response of the support is taken to be $p=k_s\Delta x$, here Δx is the displacement and k_s is the rigidity of the support. In order to focus on the essential mechanisms involved, we postpone the consideration of developing a full theory for this system; instead, we try to use a simple, linear bending theory that does not take into account the compression and extension of the beam (it can be shown that the effects of compression and extension are small [50]). The scenario of the system performance is that as the curvature of the beam changes, the end-to-end span also changes, which is coupled with the elastic response from the support. The change of the end-to-end span of the beam can be calculated by comparing the length difference between the curved beam and the projection of the beam on the x axis. The difference of each pair of corresponding elements is (Figure 5.14)

$$ds - dx = dx\sqrt{1 + \left(\frac{dy}{dx}\right)^2} - dx \quad (5.23)$$

when dy/dx is small, the Taylor expansion on the right hand side with respect to dy/dx around 0, dropping higher order terms, gives,

$$\begin{aligned} ds - dx &= dx\left[0 + 0 \cdot \left(\frac{dy}{dx}\right) + \frac{1}{2}\left(\frac{dy}{dx}\right)^2 + \dots\right] \\ &\approx \frac{1}{2}\left(\frac{dy}{dx}\right)^2 dx \end{aligned} \quad (5.33)$$

Therefore the displacement of the end of the beam is given by

$$\Delta x = \frac{1}{2} \int_0^{l/2} \left(\frac{dy}{dx}\right)^2 dx \quad (5.34)$$

However the original (fully dry sample) shape of the beam is not a straight one, instead it is sinusoidal shape given by $y_0=a_0\sin(kx/L)$. Taking this into account, the displacement of the end during curvature change of the beam is

$$\Delta x = \frac{1}{2} \int_0^{l/2} \left(\frac{dy_0}{dx} \right)^2 dx - \frac{1}{2} \int_0^{l/2} \left(\frac{dy}{dx} \right)^2 dx \quad (5.35)$$

Substituting y_0 and Equation (5.22) into this equation gives

$$\Delta x = \frac{\pi^2}{8L} \left(a_0^2 - \frac{a_n^2}{(1-\alpha)^2} \right) \quad (5.36)$$

The linear support also provides

$$\Delta x = \frac{p}{k_s} \quad (5.37)$$

From Equations (5.36) and (5.37) we have

$$\tilde{a}_n^2 = (1 - \beta\alpha)(1 - \alpha)^2 \quad (5.38)$$

where $\tilde{a}_n = a_n/a_0$ is the dimensionless natural midpoint deflection, and

$$\beta = 8EI / k_s L a_0^2 \quad (5.39)$$

is also a dimensionless parameter which is proportional to the ratio of the flexural rigidity of the beam and the rigidity of the support. We can also define the dimensionless actual mid-point deflection from Equation (5.21) by dividing both sides with a_0 , then

$$\tilde{a}_a = \frac{a_a}{a_0} = \frac{\tilde{a}_n}{1-\alpha} \quad (5.40)$$

Equations (5.38) and (5.40) give the parametric relations between the dimensionless natural midpoint deflection and the dimensionless actual midpoint deflection. In Equation (5.38), the left hand side (\tilde{a}_n^2) is non-negative, and $(1 - \alpha)^2$ on the right hand side is also non-negative; therefore, the following inequality must be satisfied:

$$1 - \beta\alpha \geq 0 \quad (5.41)$$

However, Euler's column theory [51] tells us that the minimum axial force required to cause the buckling of beams with hinged ends is $p_{er} = \pi^2 EI / L^2$. We notice that $\alpha = p/p_{er}$.

Therefore, for the beam to buckle, then must $\alpha \geq 1$. From Equation (5.41), we obtain

$$\beta \leq 1 \quad (5.42)$$

This means the rigidity of the support should be higher comparing with the flexural rigidity in order to have the buckling take place and Equation (5.42) give the threshold of the ratio between these two rigidities.

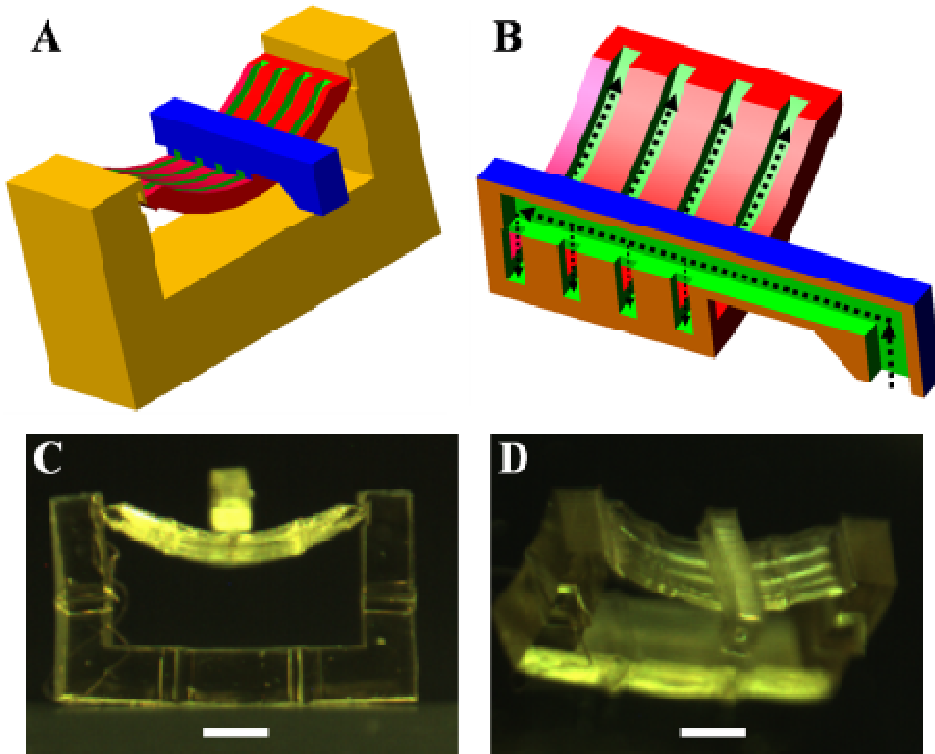


Figure 5.15 A. The CAD design of the polymer gel bistable device. B. A half section view of the curved beam. The arrows indicate the direction of solvent flow. C, D. Optical images of the microfabricated sample. Scale bars are 500 microns.

Now let us apply this analysis to a real device as shown in Figure 5.15. It consists of three parts: a curved, flat beam (red) with open channels (green) on one of the surfaces; a hollow faucet (blue), which delivers the solvent to the channels; and a U-shaped elastic frame (orange), all made of the same PEG material. The overall dimensions of the frame are 3.5 mm×2 mm×1 mm, and the beam is 175- μ m thick with channels that are 90- μ m wide and 75- μ m deep. One way in which our beam differs from silicon MEMS curved

beams, whose curvature is formed from the introduction of an initial residue stress, is that our designed beam is initially curved without appreciable residue stress. Initial residue stress is a costly and hard-to-control process; therefore, our design represents a cheaper and easier alternative for achieving curved beams. Upon solvent delivery to the inlet of the faucet, a strong capillary force drives the solvent through the inner channel of the faucet and dispenses it to the four connected open channels. As observed in the experiment, this happens in a period of less than 20 ms. Compared to the diffusion speed, we can assume that all the channels are filled with solvent at the same time. This assumption is essential for the model analysis. In our design, the beam curvature decreases and the end-to-end span of the beam increases as the solvent further diffuses into the polymer. However, the dry elastic frame resists the increase of the elongation of the beam by applying a pair of compressive forces at both ends of the curved beam. This causes an increase in the internal elastic energy in the device. As the curvature reaches a critical value, the compressive force generated by the frame may be not sufficient to constrain the beam, causing the beam to buckle. It can be shown in our analysis and experiment that if the buckling occurs in the swelling process, then the device will experience buckling in the shrinking process as well.

We model the complex geometry of our gel device as four simple beams with the lengths and moments of inertia shown in Figure 5.16. From our experiments, the solvent volume ratio of solvent is less than 5% during most of the time in the actuation. Therefore all beams are assumed to have the same Young's modulus E , and it remains the same during swelling. Beams 2 and 4 are identical, and both are fixed with Beam 3. Beam 1 is connected to Beams 2 and 4 only by a thin film 20 μm in thickness. Therefore,

we model Beam 1 as hinged to Beams 2 and 4, as the rotation resistance is small. As a result, the interaction between Beam 1 and Beams 2 and 4 is only a pair of longitudinal p.

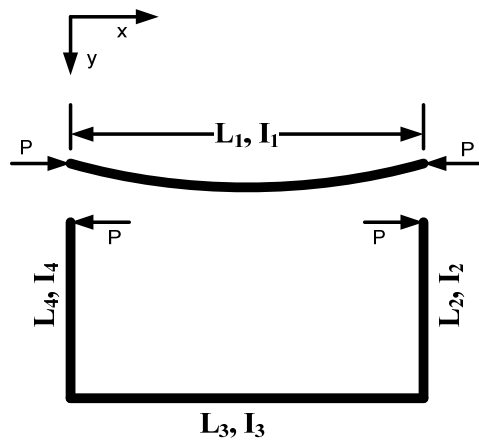


Figure 5.16. Model for a microgel bistable beam device.

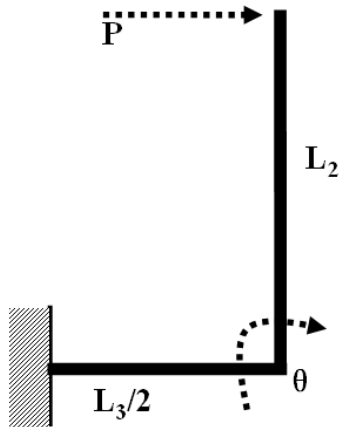


Figure 5.17. Simplified model for Beams 2 and 3.

Due to the symmetry of the structure, the deflection of Beam 2 at the joint with Beam 1 can be achieved in the simplified model (Figure 5.17). The deflection is composed of two parts: one due to the rigid rotation of Beam 2, θL_2 and the other from the deflection of

Beam 2 under transverse load p , w_2 . The expressions for θ and w_2 can be found in [52].

Thus,

$$\Delta x_2 = \theta L_2 + w_2 = p \left(\frac{L_2^2 L_3}{2EI_3} + \frac{L_2^3}{3EI_2} \right) \quad (5.43)$$

Therefore in this case, the rigidity of the elastic support is

$$k_S = \frac{6EI_2 I_3}{3L_2^2 L_3 I_2 + 2L_2^3 I_3} \quad (5.44)$$

Substituting this expression into Equation (5.39) then we have

$$\beta = \frac{8L_2^2 I_1}{a_0^2 L_1} \left(\frac{L_3}{2I_3} + \frac{L_2}{3I_2} \right) \quad (5.45)$$

It can be rewritten as

$$\beta = \frac{p_{er} \left(\frac{L_2^2 L_3}{2EI_3} + \frac{L_2^3}{3EI_2} \right)}{\frac{\pi^2 a_0^2}{8L_1}} \quad (5.46)$$

Therefore, β is also the ratio of the end deflection of Beam 2 when $p=p_{er}$ to the extension of Beam 1 due to the original deflection y_0 which is the maximum extension. This means that in order for buckling to take place, the resistant force from the support as the beam reaches the maximum extension should be larger than p_{er} . From Equation (5.46), to achieve that, the initial deflection of Beam 1 should be large, and the flexural rigidity of Beams 2, 3, and 4 needs to be large compared to beam 1 as well. In this way, the U-shaped frame can provide enough axial force to trigger the buckling of curved beams. As can be seen in Figure 5.18, the critical value of β that separates the buckling region ($\beta < 1$) and smooth deformation region ($\beta > 1$) is unity. Polymer swelling or shrinking causes the natural deflection to monotonically decrease or increase, respectively. In the buckling

region, during the change in natural deflection, the actual deflection jumps from one side to another at certain points. These points are the unstable configurations in which the buckling happens. However, when $\beta > 1$, the actual deflection changes continuously with the natural deflection, and no buckling occurs.

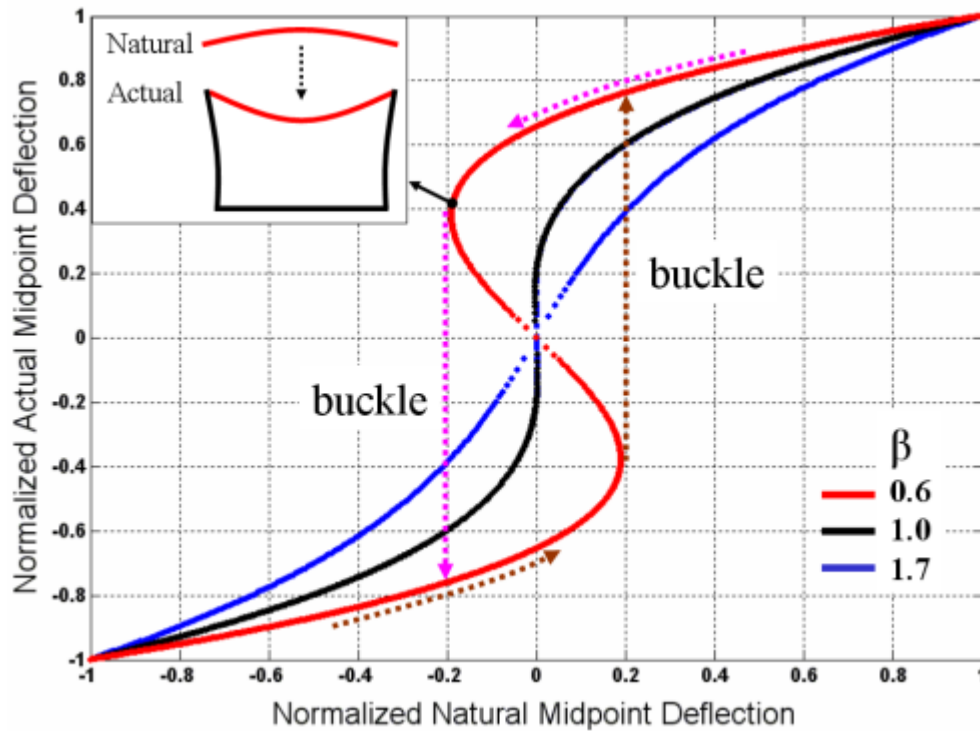


Figure 5.18 The dependence of the relationship between the actual and the natural midpoint deflection on the geometric parameter β .

It can also be shown that buckling is an energy-favorable phenomenon. Since the compression and extension energies are small [50], the elastic energy is considered to be bending energy. The bending energy is expressed in the form of [53]:

$$U = \frac{1}{2EI} \int_0^L M^2 dx \quad (5.47)$$

here M is the bending moment. The total elastic energy consists of four portions: the elastic energies stored in Beams 1, 2, 3, and 4, with those of Beams 2 and 4 being identical. That is,

$$U_{total} = U_1 + U_2 + U_3 + U_4 = U_1 + 2U_2 + U_3 \quad (5.48)$$

The bending moment for Beam 1, 2, and 4 are:

$$\begin{cases} M_1 = p \times y = \frac{pa_n}{1-\alpha} \sin\left(\frac{\pi}{L_1} x\right) \\ M_2 = p \times x \\ M_3 = p \times L_2 \end{cases} \quad (5.49)$$

Combining Equations (5.47), (5.48), and (5.49), we have:

$$U_{total} = \frac{p^2 a_n^2 L_1}{4EI_1(1-\alpha)^2} + \frac{p^2 L_2^3}{3EI_2} + \frac{p^2 L_2^2 L_3}{2EI_3} \quad (5.50)$$

Dividing both sides of Equation (5.50) by $U_0 = \frac{p_{er} \pi^2 a_0^2}{8L_1}$ gives the dimensionless total elastic energy:

$$\tilde{U}_{total} = (2 + \beta - 2\beta\alpha)\alpha^2 \quad (5.51)$$

Here $\tilde{U}_{total} = \frac{U_{total}}{U_0}$. From the expression of U_0 , it can be seen that U_0 is the work done by

the critical load p_{er} over the distance equivalent to the extension of Beam 1 due to the initial deflection y_0 . Equations (5.38) and (5.51) reveal the relationship between the elastic energy \tilde{U}_{total} and the natural midpoint deflection \tilde{a}_n of Beam 1. As shown in Figure 5.19, in the buckling region ($\beta < 1$), the elastic energy keeps accumulating until snapping takes place. The accumulated elastic energy suddenly drops and mostly transfers into kinetic energy. When $\beta > 1$, the elastic energy changes smoothly with the

natural deflection. No sudden drop of energy is observed. The drop in energy increases as β decreases. This can be achieved by increasing the initial deflection of Beam 1 or making the flexural rigidities of Beams 2, 3, and 4 higher. From (5.51), when $\beta=1$, the maximum of \tilde{U}_{total} is 1, or $U_{total} = U_0$. Therefore the minimum energy required to trigger the buckling of this curved beam device is U_0 . This energy comes from the Gibbs energy change during solvent and polymer mixing or separation (solvent evaporation) [46]. Therefore it is a material property associated with particular polymer-solvent systems and thus it also provides a criterion for the material selection during the device design. Unfortunately, solvent transport in polymers is coupled with large deformations and is still a difficult and unsolved problem; further theoretical investigation is needed to understand and predict such phenomena at full scale.

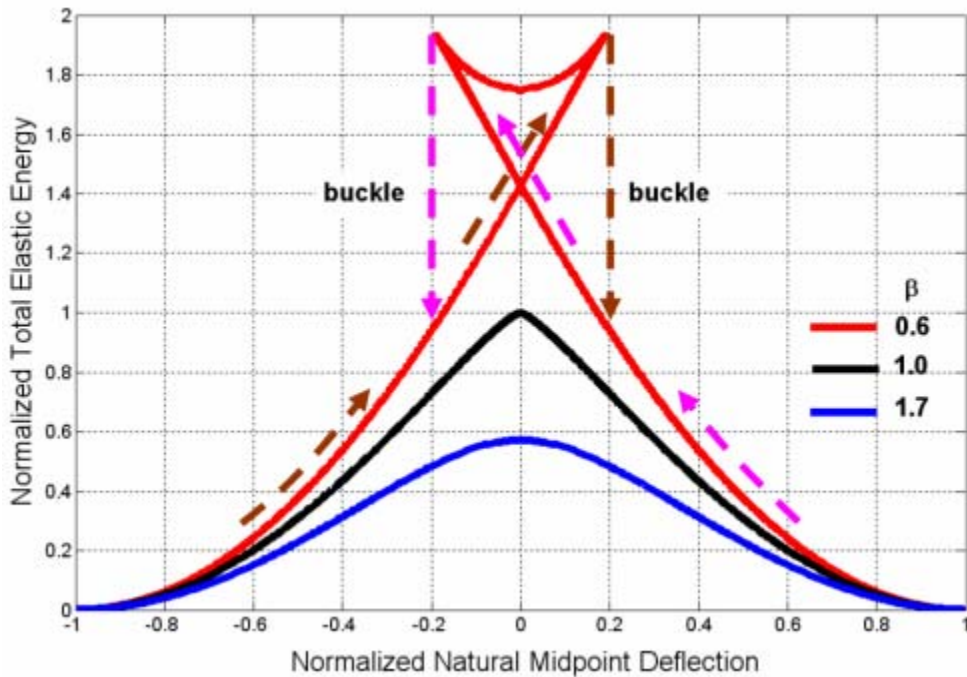


Figure 5.19 The dependence of the relationship between the total elastic energy and the natural midpoint deflection on the geometric parameter β .

5.3.3 Device performance

Using previous bending analysis, we designed and fabricated two samples with $\beta=0.4$ and $\beta=1.6$ using P μ SL. The dimension of the curved beam was the same in both samples, with an end-to-end span of 2 mm, a thickness of 175 μm , and channels that were 90- μm wide and 75- μm deep. We changed the value of β by changing the dimensions of the U-shaped frame, in which case we were able to reduce the β value by increasing the thickness of Beams 2, 3, and 5. Immediately following the P μ SL process, the samples were immersed in acetone and shielded (by covering) from ambient light for 24 hours to remove residual monomers, preventing further photo-polymerization. The samples were then dried at room temperature for 20 minutes before 0.5 μL acetone was delivered to them through the inlet of the faucet (Figure 5.20) by a syringe. An acetone droplet was first pushed out and it attached to the needle tip. Then the needle was moved to the faucet, making the droplet touch with the faucet. The droplet was immediately sucked into the faucet and almost at the same time the faucet detached from the needle tip due to disappearance of the droplet and the moving away of the faucet.

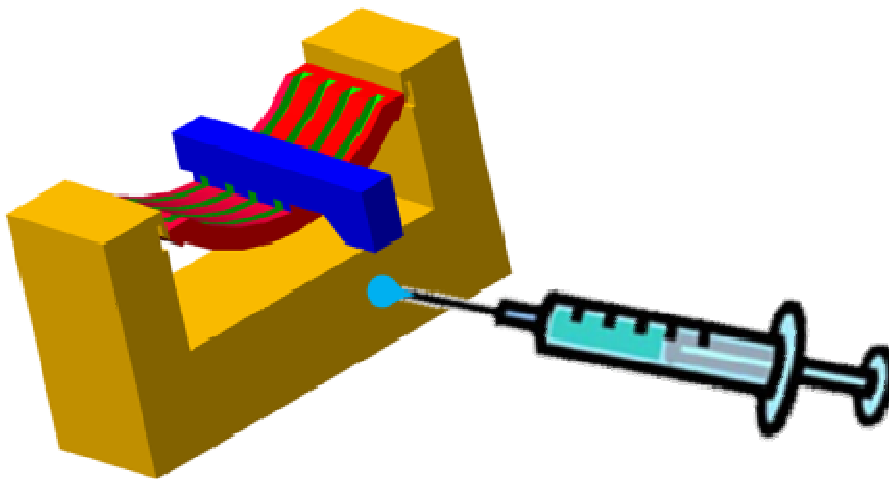


Figure 5.20. Actuating the bistable beam device using a syringe.

A video camera with frame rate of 60 fps recorded the motion of the beam (Figure 5.21). The videos were analyzed and the mid-point deflection of the beams in both samples was measured (Figure 5.22A). It is clearly shown that when $\beta < 1$, the beam buckles up and down during polymer swelling and shrinking, respectively. The actuation displacement is 45% of the end-to-end span of the beam. This value is much higher than that of silicon MEMS devices, which is typically less than 5% [21]. In contrast, the mid-point deflection transits smoothly in the case of $\beta > 1$. From Figure 5.22A, we can also see that at the beginning of solvent actuation, beams with $\beta > 1$ move faster than those with $\beta < 1$. This is because the beam with $\beta < 1$ takes time to accumulate elastic energy before it suddenly buckles. Figure 5.22B more clearly demonstrates that by introducing the instability mechanism, the maximum velocity at the mid-point increases by a factor of at least 20. The highest mid-point velocity we have observed is 3.1 cm/s with a beam length of 2 mm. The mid-point speed increases as β decreases which requires a stiffer U-shaped frame. However as we mentioned above, the elastic energy stored in the device comes from the mixing energy of the polymer and solvent. This amount of total energy is not changed when we increase the flexural rigidity of the U-shaped frame. Thus, in order for the beam to buckle, the mixing energy should be larger than the stored elastic energy associated with an instable configuration. However, if the mixing energy is too small to overcome the energy threshold associated with instable configurations, the beam will never buckle, even when $\beta < 1$. Therefore, increasing the flexural rigidity of the U-shaped frame can increase the mid-point speed during buckling. But the increase of the flexural rigidity is only up to a critical point, above which further increase will fail to cause the

beam to buckle. Prediction of the mixing energy during swelling in this device requires further theoretical and experimental investigation.

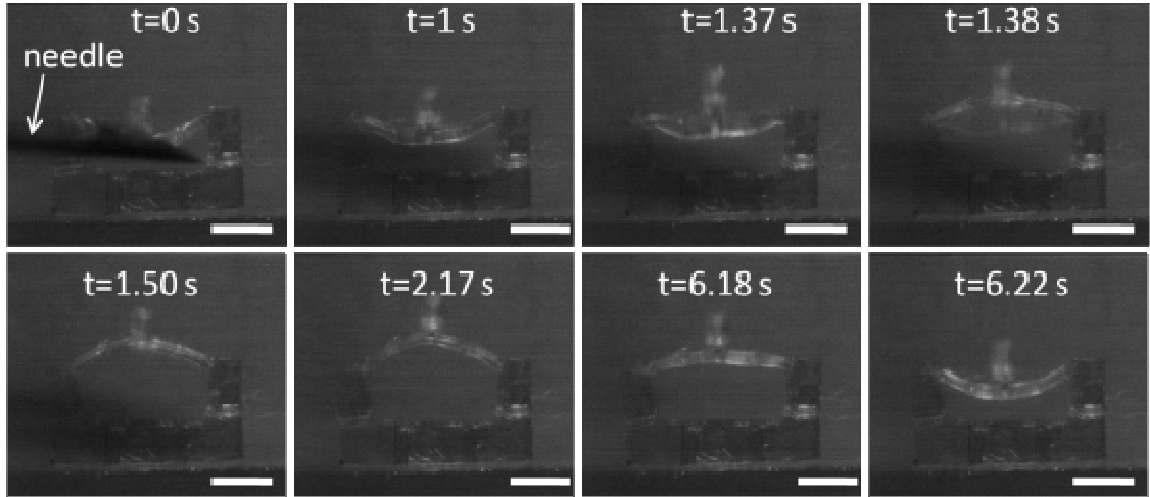


Figure 5.21 Time frames of the bistable beam device ($\beta=0.4$) actuated by a drop of acetone.

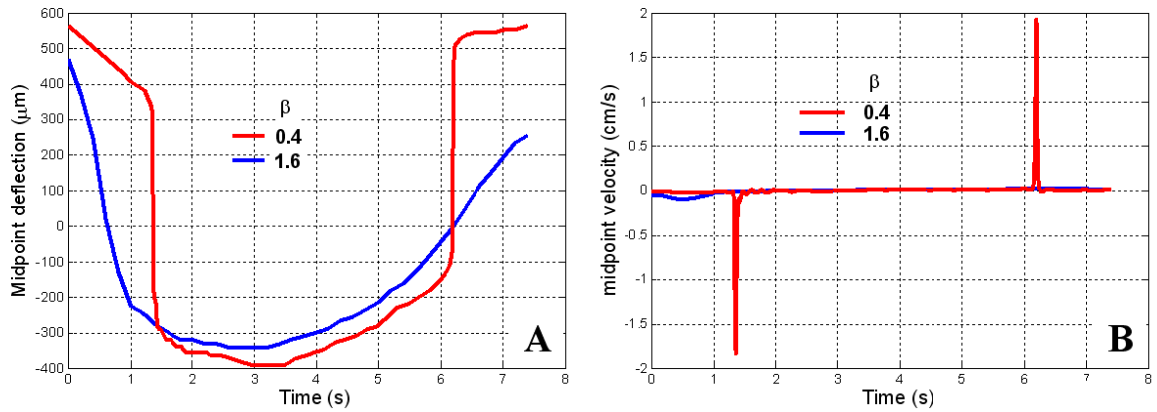


Figure 5.22 A. Measured midpoint deflection of curve beams during solvent actuation. B. Calculated midpoint velocity during solvent actuation.

5.4 CONCLUSIONS AND OUTLOOK

In an effort to increase the response speed of a polymeric hydrogel device during solvent actuation, in this chapter we reported on the design, analysis, fabrication and

testing of several novel polymeric devices. We introduced a capillary network into polymeric devices in such a way as to dramatically increase the rate of long-range solvent transport (compared with diffusion-based mechanisms), while also providing a means to locally control the swelling of polymeric hydrogel. We realized control of surface-oriented swelling in a curved polymeric beam, which also affected its bending direction. Compared with traditional silicon MEMS devices, using this method we achieved much higher actuation displacement with respect to the length of the beam without sacrificing the actuation speed. To further increase the transient response speed, we introduced an elastic instability into our beam design. Combined with a design criteria analysis based on beam bending theory, we proved in our experiment the existence of a critical value for the dimensionless parameter β that determines whether or not a curved beam will buckle. Further theoretical investigation on solvent transport in polymers coupled with large deformation is needed to fully understand this phenomenon. Due to its unique quick response time, this device has potential for a range of self-powered and autonomous systems, such as micro-fluidic transducers and valves, and artificial muscles.

As ongoing efforts, on the modeling side, we are collaborating with Dr. Jiang's group in Arizona State University to look for a theoretical explanation which couples the large deformation and viscoelastic-creep-driven transport to predict the behavior in our device; on the other side, we are continuing to design more complicated snapping device based on continuum elastic theory, for example, we have successfully designed a doubly-curved device to mimic the movement of versus fly traps, which is capable of switching the direction of concavity in less than 20 ms, under the actuation of an acetone droplet.

REFERENCES

- [1] Ling Xu, Xin Li, Maolin Zhai, Ling Huang, Jing Peng, Jiuqiang Li, and Genshuan Wei, Ion-Specific Swelling of Poly(styrene sulfonic acid) Hydrogel, *J. Phys. Chem. B* 2007, 111, 3391-3397.
- [2] Huidi Ji, Hashem Mourad, Eliot Fried and Hohn Dolbow, Kinetics of thermally induced swelling of hydrogels, *International Journal of Solids and Structures* 43(2006) 1878-1907.
- [3] Tetsu Tatsuma, Kazutake Takada and Taichi Miyazaki, UV-Light-Induced Swelling and Visible-light-Induced Shrinking of a TiO₂-Containing Redox Gel, *Advanced Materials*, 2007, 19, 1249-1251.
- [4] Toyochi Tanaka and David J. Fillmore, Kinetics of swelling of gels, *J. Chem. Phys.* 70(03), Feb. 1979, 1214-1218
- [5] Yong Li and Toyochi Tanaka, Kinetics of swelling and shrinking of gels, *J. Chem. Phys.* 92(2), Jan. 1990, 1365-1371
- [6] Sudipto K. De, N. R. Aluru, B. Johnson, W. C. Crone, David J. Beebe and J. Moore, Equilibrium Swelling and Kinetics of pH-Responsive Hydrogels: Models, Experiments and Simulations, *Journal of MEMS*, Vol. 11, No.5 (2002), 544-555.
- [7] Gerald Gerlach, Margarita Guenther, Joerg Sorber, Gunnar Suchanek, Karl-Friedrich Arndt, Andreas Richter, Chemical and pH sensors based on the swelling behavior for hydrogels, *Sensors and Actuators B* 111-112(2005)555-561.
- [8] Sebastiaan Herber, Wouter Olthuis and Piet Bergveld, A swelling hydrogel-based Pco₂ sensor, *Sensors and Actuators B* 91 (2003) 378-382.
- [9] Trong-Ming Don, Mei-Lien Huang, Ai-Chien Chiu, Kuo-Huai Kuo, Wen-Yen Chiu and Lien-Hua Chiu, Preparation of thermo-responsive acrylic hydrogels useful for the application in transdermal drug delivery systems, *Materials Chemistry and Physics* 107(2008)266-273.
- [10] Bumsang Kim, Kristen La Flamme and Nicholas A. Peppas, Dynamic Swelling Behavior of pH-sensitive Anionic Hydrogels Used for Protein Delivery, *Journal of Applied Polymer Science*, 89, 1606-1613(2003).
- [11] Dongshin Kim and David J. Beebe, Hydrogel-based reconfigurable components for microfluidic devices, *Lab on a Chip*, 2007, 7, 193-198
- [12] Jingjiao Guan, Hongyan He, Derek J. Hansford and L. James Lee, Self-Folding of Three-Dimensional Hydrogel Microstructures, *the journal of Physical Chemistry B*, 2005, 109, 23134-23137.
- [13] David J. Beebe, Jeffrey S. Moore, Joseph M. Bauer, Qing Yu, Robin H. Liu, Chelladurai Devadoss and Byung-Ho Jo, Functional hydrogel structures for autonomous flow control inside microfluidic channels, *Nature*, 404, 588-590, 2000
- [14] Chunguang Xia, Howon Lee and Nicholas Fang, 3D polymeric devices driven by surface micro fluidic capillaries, *Proceedings of ASME Integration and Commercialization of Micro and Nano systems International conference and Exhibition*, 2008.
- [15] Washburn, Edward W., The dynamics of capillary flow, *physical Review*, v18,n3, p273-283, 1921
- [16] S. P. Timoshenko and J. M. Gere, *Theory of Elastic Stability*. New York: MacGraw-Hill, 1961, p. 76, 77, 84

- [17] M. Vangbo, "An analytical analysis of a compressed bistable buckled beam," *Sens. Actuators*, v69, p 212–216, 1998
- [18] M. Taher A. Saif, On tunable bi-stable MEMS-theory and experiment, *Journal of MEMS*, V9,n2,157–170, 2000
- [19] Jin Qiu, Jeffrey H. Lang, and Alexander H.Slocum, A curved-beam bistable mechanism, *Journal of MEMS*, v13,n2, p137-146, 2004
- [20] M. Chiao and L. Lin, Self-buckling of micromachined beams under resistive heating, *Journal of MEMS*, v9, n1, p146–151, 2000.
- [21] Aron Michael, Chee Yee Kwok, Kevin Yu, and Mark R. Mackenzie, A novel Bistable two-way actuated out-of-plane electrothermal microbridge, *Journal of MEMS*, v17, n1, p58-69, 2008
- [22] D. De Kee, Q. Liu and J. Hinestroza, Viscoelastic (Non-Fickian) Diffusion, the *Canadian Journal of Chemical Engineering*, v83, pp913-929, 2005
- [23] Aminabhavi, T. M., U. S. Aithal and S. S. Shukla, "An Overview of the Theoretical Models Used to Predict Transport of Small Molecules Through Polymer Membranes," *J. Macromol. Sci., Rev. Macromol. Chem. Phys. C28*, pp.421–474 (1988).
- [24] Vrentas, J. S. and J. L. Duda, "Diffusion," *Encycl. Polym.Sci. Eng.* **5**, 36–68 (1986).
- [25] J.S. Vrentas, C.M. Jarzebski and J.L. Duda, *A.I.Ch.E.J.* 21 (1975) 894.
- [26] Alfrey, T., E. F. Gurnee and W. G. Lloyd, "Diffusion in Glassy Polymers," *J. Polymer Sci., Part C: Polym. Symp.* 12, 249–261 (1966).
- [27] Neogi, P., "Transport Phenomena in Polymer Membranes," *Plast. Eng.* 32, 173–209 (1996).
- [28] Chan Man Fong, C. F., C. Moresoli, S. Xiao, Y. Li, J. Bovenkamp and D. De Kee, "Modeling Diffusion through Geomembranes," *J. Appl. Polym. Sci.* 67, pp 1885–1889, (1998).
- [29] Frisch, H. L., "Irreversible Thermodynamics of Internally Relaxing Systems in the Vicinity of the Glass Transition, in *Non-Equilibrium Thermodynamics, Variational Techniques and stability*," Dennelly, R. J., R. Herman and I. Prigogine, University of Chicago Press, Chicago (1966).
- [30] Crank, J. and G. S. Park, "Diffusion in Polymers," Academic Press, London and NY (1968).
- [31] Frisch, H. L., "Isothermal Diffusion in Systems with Glasslike Transitions," *J. Chem. Phys.* 41, 3379–3683(1964).
- [32] Long, F. A. and D. Richman, "Concentration Gradients for Diffusion of Vapors in Glassy Polymers and their Relations to Time-Dependent Diffusion Phenomena," *J. Am. Chem. Soc.* 82, 513–519 (1960).
- [33] Richman, D. and F. A. Long, "Measurement of Concentration Gradients for Diffusion of Vapors in Polymers," *J. Am. Chem. Soc.* 82, 509–513 (1960).
- [34] Vrentas, J. S. and C. M. Vrentas, "Integral Sorption in Glassy Polymers," *Chem. Eng. Sci.* 53, 629–638 (1998).
- [35] Thomas, N. L. and A. H. Windle, "A Deformation Model for Case II Diffusion," *Polymer* 21, 613–619 (1980).
- [36] Thomas, N. L. and A. H. Windle, "Diffusion Mechanics of the System PMMA-methanol," *Polymer* 22, 627–639 (1981).

- [37] Thomas, N. L. and A. H. Windle, "A Theory of Case II Diffusion," *Polymer* 23, 529–542 (1982).
- [38] Cox, R. W. and D. S. Cohen, "A Mathematical Model for Stress-Driven Diffusion in Polymers," *J. Polym. Sci., Part B: Polym. Phys.* 27, 589–602 (1989).
- [39] Cohen, D. S., "Theoretical Models for Diffusion in Glassy Polymers. II," *J. Polym. Sci., Polym. Phys. Ed.* 22, 1001–1009 (1984).
- [40] Biot, M.A., General theory of three-dimensional consolidation. *J. Appl. Phys.* 12 (2), 155–164. (1941)
- [41] Coussy, O., 2004. *Poromechanics*. Wiley, New Jersey.
- [42] Tanaka, T., Fillmore, D.J., Kinetics of swelling of gels. *J. Chem. Phys.* 70 (3), 1214–1218. (1979)
- [43] Durning, C.J., Morman, K.N., Nonlinear swelling of polymer gels. *J. Chem. Phys.* 98 (5), 4275–4293. (1993)
- [44] Dolbow, J., Fried, E., Jia, H.D., 2004. Chemically induced swelling of hydrogels. *J. Mech. Phys. Solids* 52 (1), 51–84.
- [45] Li, H., Luo, R., Birgersson, E., Lam, K.Y., Modeling of multiphase smart hydrogels responding to pH and electric voltage coupled stimuli. *J. Appl. Phys.* 101 (11).(2007)
- [46] Wei Hong, Xuanhe Zhao, Jinxiong Zhou, and Zhigang Suo, A theory of coupled diffusion and large deformation in polymeric gels, *Journal of Mechanics and Physics of Solids*, 56 (2008) 1779–1793
- [47] Donald S. Cohen and Thomas Erneux, "Changing Time History in Moving Boundary Problems", *SIAM Journal on Applied Mathematics*, Vol. 50, No. 2, pp. 483-489, (1990).
- [48] Jingjiao Guan, Hongyan He, Derek J. Hansford and L, James Lee, Self-Folding of Three-Dimensional Hydrogel Microstructures, *the journal of Physical Chemistry B*, 2005, 109, 23134-23137.
- [49] Stephen R. Quake and Axel Scherer, From micro- to nanofabrication with soft materials, *Science*, v290, p1536-1540, 2000
- [50] A. Pfluger, *Stabilitatsprobleme der Elastostatik*, Springer-verlag, berlin, 1950
- [51] S. P. Timoshenko and J. M. Gere, *Theory of Elastic Stability*. New York: MacGraw-Hill, 1961,p49
- [52] S. P. Timoshenko, *Strength of Materials*, 3d ed.,D. Van Nostrand Company, Inc, Princeton, N.J., 1955, part I, p151
- [53] S. P. Timoshenko, *Strength of Materials*, 3d ed.,D. Van Nostrand Company, Inc, Princeton, N.J., 1955, part I, p306

AUTHOR'S BIOGRAPHY

Chunguang Xia was born on March 07, 1980, in Fujian, China. He graduated from the University of Science and Technology of China with a bachelor's degree in theoretical and applied mechanics. In 2002, he joined the department of theoretical and applied mechanics at the University of Illinois at Urbana-Champaign and obtained his master degree in 2004 before he transferred to the department of mechanical engineering for PhD. His research focused on developing technologies for three dimensional polymeric micro fabrication, three dimensional particle patterning, mass transport in thick tissue culture, and developing novel polymeric actuators. These researches have led to multiple publications, patents, and the present dissertation.

Journal publications (first author only) and patents

1. C. Xia, Howon Lee, and N. Fang, "Solvent Driven Polymeric Bistable Device", Journal of MEMS, under revision.
2. C. Xia and N. Fang, "Fully Three-Dimensional Micro Fabrication with Grayscale Polymeric Sacrificial Structure", Journal of Micromechanics and Microengineering, accepted, September 2009.
3. C. Xia and N. Fang, "3D Microfabricated bioreactor with capillaries", Journal of Biomedical Microdevices, accepted, August 2009.
4. C. Xia, A. Cox, and N. Fang, "3D microfabricated bioreactor with imbedded capillary network". International Patent, WO2009/042671.
5. C. Xia and N. Fang, "Membrane-pump stereolithography", US patent pending.